

Travail de fin d'études et stage[BR]- Travail de fin d'études : Concentrated solar power plants: multiscale parameter identification for a damage based corrosion model.[BR]- Stage d'insertion professionnelle

Auteur : Rodrigo Ruiz de Arriaga, Luis Miguel

Promoteur(s) : Duchene, Laurent

Faculté : Faculté des Sciences appliquées

Diplôme : Cours supplémentaires destinés aux étudiants d'échange (Erasmus, ...)

Année académique : 2021-2022

URI/URL : <http://hdl.handle.net/2268.2/14156>

Avertissement à l'attention des usagers :

Tous les documents placés en accès ouvert sur le site le site MatheO sont protégés par le droit d'auteur. Conformément aux principes énoncés par la "Budapest Open Access Initiative"(BOAI, 2002), l'utilisateur du site peut lire, télécharger, copier, transmettre, imprimer, chercher ou faire un lien vers le texte intégral de ces documents, les disséquer pour les indexer, s'en servir de données pour un logiciel, ou s'en servir à toute autre fin légale (ou prévue par la réglementation relative au droit d'auteur). Toute utilisation du document à des fins commerciales est strictement interdite.

Par ailleurs, l'utilisateur s'engage à respecter les droits moraux de l'auteur, principalement le droit à l'intégrité de l'oeuvre et le droit de paternité et ce dans toute utilisation que l'utilisateur entreprend. Ainsi, à titre d'exemple, lorsqu'il reproduira un document par extrait ou dans son intégralité, l'utilisateur citera de manière complète les sources telles que mentionnées ci-dessus. Toute utilisation non explicitement autorisée ci-avant (telle que par exemple, la modification du document ou son résumé) nécessite l'autorisation préalable et expresse des auteurs ou de leurs ayants droit.



Université de Liège – Faculté des Sciences Appliquées

MASTER'S THESIS CARRIED OUT TO OBTAIN THE DEGREE OF MASTER OF SCIENCE IN
MECHANICAL ENGINEERING

Concentrated solar power plants: Multiscale parameter identification for a damage based corrosion model

MIGUEL RODRIGO RUIZ DE ARRIAGA

Supervisor:	LAURENT DUCHENE	(ULiège)
Jury Members:	HELENE MORCH	(ULiège)
	PIERRE DUYSINX	(ULiège)
	RIDHA HARZALLAH	(John Cockerill)

Academic Year 2021-2022

ABSTRACT

This work aimed the coupling between two corrosion models with two different approaches by performing a comparative traction test. It was expected to achieve reliable results with a diffusional corrosion model to adjust the parameters of a damage corrosion model.

In the diffusional model, parameters extracted from the literature were used for a nickel-based alloy subjected to 700°C. To validate the comparison and ensure that the two models were mechanically compatible, not only the corrosion damage but also the stress-strain curves of both models were compared.

After finding the optimal parameters that were sought for the model. An evaluation of these parameters has been carried out and an optimization of the formula has been suggested in order to obtain values closer to the diffusional model.

ACKNOWLEDGMENTS

I would like to thank my master thesis supervisor, Prof. Laurent Duchene, as well as H  l  ne Morch for their great academic support throughout the thesis. Their willingness and constant suggestions at this stage have helped me a lot and have made me grow academically and professionally.

I would also like to thank Ridha Harzallah for his guidance during the internship at John Cockerill, as well as for his confidence in the accomplishment of this project.

Finally, I would like to give thanks to my family and my closest friends for their support during the months of the thesis, as well as to those who have offered me advice.

Table of Contents

1	INTRODUCTION	1
1.1	CONTEXT OF THE STUDY	1
1.2	OBJECTIVES.....	5
2	FUNDAMENTALS OF CORROSION	6
2.1	SALT DEGRADATION	6
2.2	MATERIAL CORROSION.....	9
2.3	CORROSION MODELLING	11
2.3.1	<i>Diffusion models.....</i>	<i>12</i>
2.3.2	<i>Damage variable models</i>	<i>16</i>
3	MODELS	19
3.1	LAGAMINE MODEL	19
3.1.1	<i>Lagamine software.....</i>	<i>20</i>
3.1.2	<i>Mechanical behaviour</i>	<i>20</i>
3.1.3	<i>Corrosion behaviour.....</i>	<i>22</i>
3.1.4	<i>Model review.....</i>	<i>24</i>
3.2	DIFFUSIONAL ELASTIC MODEL	24
3.2.1	<i>Software.....</i>	<i>24</i>
3.2.2	<i>Mechanical behaviour</i>	<i>25</i>
3.2.3	<i>Corrosion coupling.....</i>	<i>26</i>
3.3	COUPLING OF MODELS	29
4	COMPARISON OF MODELS	31
4.1	TEST CONDITIONS	31
4.1.1	<i>Fixed displacements.....</i>	<i>31</i>
4.1.2	<i>Material properties.....</i>	<i>32</i>
4.1.3	<i>Load.....</i>	<i>34</i>
4.1.4	<i>Meshes.....</i>	<i>35</i>
4.1.5	<i>Corrosion.....</i>	<i>37</i>
4.2	COMPARISON WITHOUT CORROSION	40
4.3	COMPARISON WITH CORROSION	42
4.3.1	<i>Determination of the time simulation.....</i>	<i>42</i>
4.3.2	<i>First corrosion comparison.....</i>	<i>44</i>
4.3.3	<i>Study of the negative oscillations.....</i>	<i>46</i>
4.3.4	<i>Mesh modification.....</i>	<i>53</i>
4.3.5	<i>Corrosion comparison by average damage variable</i>	<i>55</i>
4.3.6	<i>Mesh modification to overcome the convection limitation.....</i>	<i>59</i>
4.3.7	<i>Final comparison between models</i>	<i>60</i>
5	DISCUSSION.....	65
5.1	EQUATION FITTING FOR 7,05 YEARS	66
5.2	EQUATION FITTING FOR 25 YEARS	68
6	CONCLUSIONS AND PERSPECTIVES.....	70

BIBLIOGRAPHY.....73

LIST OF FIGURES

FIGURE 1.1 KEY BENEFITS OF CSP TECHNOLOGY	1
FIGURE 1.2: FOUR TYPES OF CONCENTRATING SOLAR POWER TECHNOLOGIES	2
FIGURE 1.3: SCHEMATIC OF A CENTRAL RECEIVER CSP PLANT.....	3
FIGURE 2.1: MASS EVOLUTION OF SOLAR SALT SAMPLES	7
FIGURE 2.2: VOLUME CHANGES OF NO (LEFT) AND NO ₂ (RIGHT) VS. TIME AND TEMPERATURE WITH QUARTZ.....	8
FIGURE 2.3: VOLUME CHANGE OF NO UNDER DIFFERENT WORKING ATMOSPHERES WITH SS316	8
FIGURE 2.4: CORROSION MECHANISM OF 304 AND 316L SS AT DIFFERENT TEMPERATURES	9
FIGURE 2.5: (A) CROSS SECTIONAL IMAGE OF 321H ALLOY; (B) ELEMENT CONCENTRATION PROFILES OF 321H ALLOY.....	10
FIGURE 2.6 CORROSION MECHANISMS DEPENDING ON THE WORKING ATMOSPHERE AND CL- IMPURITIES FOR 316 Ti.....	11
FIGURE 2.7: SIMULATED OXYGEN CONCENTRATION AT 800°C AFTER 33,475 CYCLES FOR (A) NATURAL DIFFUSION AND (B) A PRESSURE FACTOR OF 0.3 MPA-1	13
FIGURE 2.8: SKETCH OF THE ASSUMED CORROSION PROCESS AND THE BOUNDARY CONDITION	14
FIGURE 2.9: SCHEMATIC DIAGRAM OF MAGNESIUM ALLOYS CORROSION	15
FIGURE 2.10: MORPHOLOGY FEATURE OF THE MG ALLOY PIN OVER TIME: (A) SIMULATION, (B) EXPERIMENT	15
FIGURE 2.11: COMPARISON OF METAL LOSS BETWEEN EXPERIMENTAL DATA AND A PARABOLIC MODEL FOR 304 SS AND 316 L AT 565 °C	17
FIGURE 2.12: CORROSION OF A STENT IN THE HUMAN BODY WITH CONSIDERATION STRESS INDUCED CORROSION (SC), UNIFORM CORROSION (U), OR BOTH (SCU)	18
FIGURE 3.1: VON MISES STRESS [MPa] IN THE TUBE UNDER THERMAL LOADING	19
FIGURE 3.2: YOUNG’S MODULUS OF NICKEL-BASED ALLOY HAYNES 230 DEPENDING ON THE TEMPERATURE BASED ON (3.1)	21
FIGURE 3.3: REPRESENTATION OF EFFECTIVE STRESS	22
FIGURE 3.4: COMPARISON OF PARABOLIC LAW AND LINEAR LAW	23
FIGURE 3.5 ELEMENT OF 4 NODES (QUAD4)	25
FIGURE 3.6: TIME EVOLUTION OF NATURAL CORROSION DIFFUSION	26
FIGURE 3.7: STRESS-DRIVEN CORROSION TEST	27
FIGURE 3.8: TIME EVOLUTION OF CORROSION RATE FOR THE TEST	28
FIGURE 3.9: DEGRADATION OF YOUNG’S MODULUS AS A FUNCTION OF DAMAGE VARIABLE	28
FIGURE 3.10: DEFINITION OF DAMAGE VARIABLE Φ RESPECT TO C	29
FIGURE 4.1: DIAGRAM OF FIXED DISPLACEMENTS.....	32
FIGURE 4.2: PARAMETERS OF THE CHABOCHE’S LAW FOR HAYNES 230. EXTRACT OF THE INPUT FILE OF THE LAGAMINE MODEL	33
FIGURE 4.3: APPLICATION OF SURFACE PRESSURE AT THE END OF THE BEAM	34
FIGURE 4.4: TIME EVOLUTION OF THE LOAD APPLIED	35
FIGURE 4.5: MESH USED IN THE DIFFUSIONAL ELASTIC MODEL	35
FIGURE 4.6: MESH USED IN THE LAGAMINE MODEL	36
FIGURE 4.7: MESHERS COMPARISON; ELEMENTS BORDERS OF THE LAGAMINE MODEL (BLACK LINES); NODES OF THE DIFFUSIONAL MODEL (BLUE POINTS)	36
FIGURE 4.8: DIAGRAM OF THE BOUNDARY CONDITIONS OF THE TEST.....	37
FIGURE 4.9: LAGAMINE MESH, APPLYING TOP CORROSION	38
FIGURE 4.10: LITERATURE DATA OF THE CORROSION PARAMETERS OF THE DIFFUSIONAL MODEL	38
FIGURE 4.11: STRESS-STRAIN CURVE; NO CORROSION; DIFFUSIONAL MODEL	40
FIGURE 4.12: STRESS-STRAIN CURVE; NO CORROSION; LAGAMINE MODEL	41
FIGURE 4.13: MECHANICAL COMPARISON WITHOUT CORROSION	41
FIGURE 4.14: NODES STUDIED TO DETERMINE THE TIME SIMULATION	43
FIGURE 4.15: CONCENTRATION EVOLUTION OF THE NODES LOCATED AT $\frac{3}{4}$ OF THE HEIGHT OF THE BEAM.....	43

FIGURE 4.16: DIFFERENCE BETWEEN A 10-YEAR LOAD VS A 7-YEAR LOAD	44
FIGURE 4.17: ELEMENT STUDIED IN LAGAMINE MODEL (GREEN); NODE STUDIED IN DIFFUSIONAL ELASTIC MODEL (RED)	45
FIGURE 4.18: YOUNG MODULUS COMPARISON	45
FIGURE 4.19: DAMAGE VARIABLE COMPARISON	46
FIGURE 4.20: STUDY OF OSCILLATIONS BASED ON TIME STEP	47
FIGURE 4.21: STUDY OF OSCILLATIONS BASED ON TIME STEP (ZOOM IN)	47
FIGURE 4.22: STUDY OF OSCILLATIONS BASED ON COEFFICIENT OF DIFFUSIVITY	48
FIGURE 4.23: STUDY OF OSCILLATIONS BASED ON COEFFICIENT OF DIFFUSIVITY (ZOOM IN)	49
FIGURE 4.24: STUDY OF OSCILLATIONS WITH HIGHER DIFFUSIVITY BASED ON TIME STEP	50
FIGURE 4.25: STUDY OF OSCILLATION WITH HIGH DIFFUSIVITY BASED ON TIME STEP (ZOOM IN)	50
FIGURE 4.26: STUDY OF OSCILLATION BASED ON MESH (OUTSIDE THE CORROSION ZONE)	51
FIGURE 4.27: STUDY OF OSCILLATIONS BASED ON MESH (IN THE CORROSION ZONE).....	52
FIGURE 4.28: MESH MODIFICATION; ORIGINAL (TOP); MODIFIED (BOTTOM).....	53
FIGURE 4.29: CORROSION COMPARISON BETWEEN ORIGINAL MESH AND MODIFIED MESH	54
FIGURE 4.30: CORROSION COMPARISON BETWEEN LAGAMINE MODEL AND MODIFIED MESH	55
FIGURE 4.31: MESH USED FOR THE AVERAGE COMPARISON. LAGAMINE ELEMENT (GREEN); 5 NODES AVERAGE (BLUE); 7 NODES AVERAGE (RED)	56
FIGURE 4.32: CORROSION COMPARISON BETWEEN MODELS WITH THE 7 NODES AVERAGE.....	57
FIGURE 4.33: CORROSION COMPARISON BETWEEN MODEL WITH THE 7 NODES AVERAGE WITH AN INTERPOLATION	58
FIGURE 4.34: CORROSION COMPARISON BETWEEN MODEL WITH THE 5 NODES AVERAGE	59
FIGURE 4.35: SECOND MESH MODIFICATION	60
FIGURE 4.36: FINAL CORROSION COMPARISON BETWEEN MODELS	61
FIGURE 4.37: MECHANICAL COMPARISON; IN THE CORROSION ZONE (GREEN); OUTSIDE THE CORROSION ZONE (RED)	62
FIGURE 4.38: FINAL MECHANICAL COMPARISON BETWEEN MODELS (IN THE CORROSION ZONE)	63
FIGURE 4.39: FINAL MECHANICAL COMPARISON BETWEEN MODELS (OUTSIDE THE CORROSION ZONE)	64
FIGURE 5.1: COMPARISON WITH SOLVER FITTING; 7,05-YEAR SIMULATION	66
FIGURE 5.2: COMPARISON WITH SOLVER FITTING; 10-YEAR SIMULATION	67
FIGURE 5.3: COMPARISON WITH SOLVER FITTING; 25-YEAR SIMULATION	68
FIGURE 6.1: PRESSURE FACTOR FOR NICKEL-BASED ALLOYS AT DIFFERENT TEMPERATURES [15]	71

LIST OF TABLES

TABLE 2-1: STABILITY LIMITS OF SOLAR SALT SAMPLES	7
TABLE 2-2: THE OXYGEN DIFFUSIVITY AT FOUR TEMPERATURES.....	13
TABLE 2-3: THE PRESSURE FACTOR AT FOUR TEMPERATURES.....	13
TABLE 4-1: CONSTANT TO CALCULATE MATERIAL PARAMETERS AT 700°C	33
TABLE 4-2: CORROSION VARIABLES USED IN THE DIFFUSIONAL MODEL	42
TABLE 4-3: MESHES USED TO STUDY THE OSCILLATIONS.....	51
TABLE 4-4: COMPARISON CONDITIONS.....	61

1 Introduction

1.1 Context of the study

Global climate change is a significant issue in today's society. To face this problem, reduction of greenhouse emissions has been set as an objective and there is currently an energy transition from a fossil-based system to renewable energy sources such as solar, wind, geothermal, hydrogen, etc. In this framework, developing technologies to improve the efficiency and supply of these sustainable sources has an increasing interest in solving environmental problems as the energy demand.

Among renewable energies, solar power is proposed as a promising source to satisfy the large daily demand for energy consumption. Until now, there are two main technologies concerning to solar power: Photovoltaic (PV) technology which utilize solar radiation collected by solar panels to directly obtain electricity, and Concentrated Solar Power (CSP) technology that employs mirrors to direct and focus solar radiation on a heat transfer fluid (HTF), such as molten salt, which is heated to high temperatures to generate electricity via steam turbine generator. This study will develop in the context of this last type of solar energy, the CSP plants.

CSP is a technology with great potential because it is capable of producing utility-scale electricity, offering firm capacity and dispatchable power on demand by integrating thermal energy storage through the use of a HTF. In fact, CSP plants are predicted to produce a global electricity contribution of 7% by the year 2030 and 25% by the year 2050 [1]. Moreover, it is found that the electricity demand of all Europe can be met by harvesting from only 0,4% of the Sahara Desert.

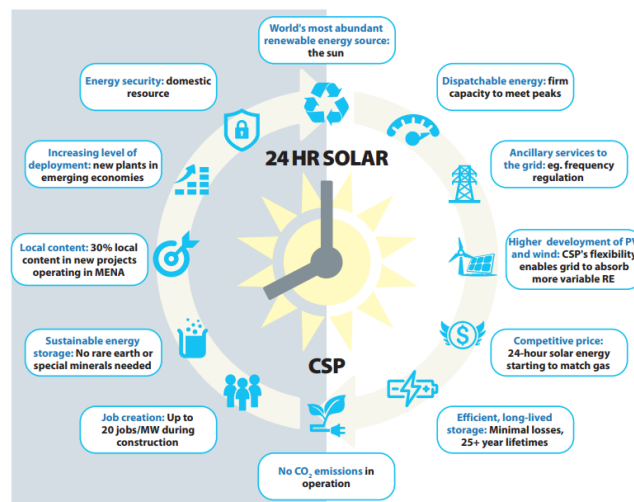


Figure 1.1 Key benefits of CSP technology

Image taken from [2]

The fact that CSP looks so promising for the future is due to its energy storage capacity and flexibility compared to other renewable sources. CSP with thermal energy storage can store energy in the form of heat, at utility scale, for days with minimal losses. Stored heat can then be converted into electricity and dispatched as required by demand, even at night or during cloudy periods of the day, providing green energy 24 hours a day. Also, its flexibility is a breakthrough in the field of renewable energies, meaning that it can quickly ramp up or down as required by the network and the energy demand. And when ramping down, output is not wasted; instead, it can be stored as heat in molten salt tanks and deployed hours or even days later. In addition, this technology has many more advantages as shown in Figure 1.1.

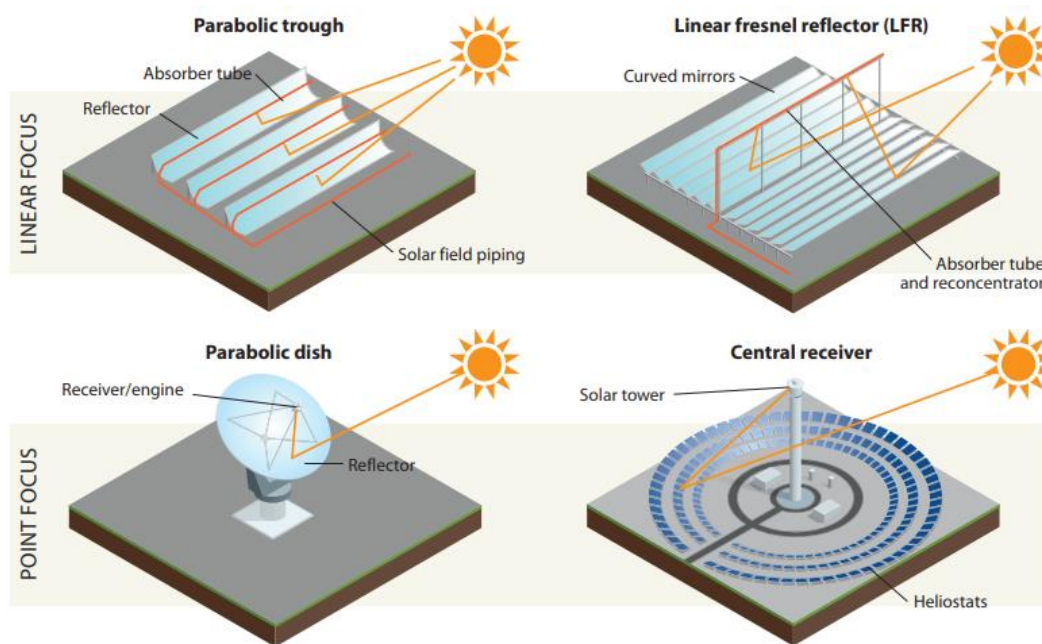


Image taken from [2]

Figure 1.2: Four types of concentrating solar power technologies

There are four CSP technologies: parabolic trough, solar tower, linear Fresnel, and parabolic dish, Figure 1.2. Currently, tower systems represent 18% of total installed CSP capacity, but this is expected to increase in the coming years. Plant unit sizes range from 10 to 150 MW and usually incorporate higher thermal energy storage capacity, making them suitable for dispatchable markets [2]. Also, the integration of towers into advanced thermodynamic cycles is feasible.

In a solar tower CSP plant, shown in Figure 1.3, the hot molten salt, which is heated in the receiver tower, is transferred to a heat exchanger to generate steam in order to convert thermal energy to mechanical work via a turbine, as in classic Rankine-based power cycle. The turbine drives a generator to have electricity as an outcome of the CSP plant. A great advantage that makes these kinds of electric plants attractive as a power generation pathway, is the facility of incorporating

high-efficiency thermal energy storage. Since CSP involves a solar-to-heat conversion step in the receiver, it is relatively straight-forward to have this capability of energy storage.

However, solar power-towers also have some challenges that need to be addressed in order to bring out their full potential. For instance, CSP is very sensitive to scale because its efficiency depends on the plant's size, making it necessary to have a massive plant to be feasible, which requires huge investments. Also, the global efficiency of CSP plants is a significant issue that limits their use.

A key constraint of the efficiency of a Rankine cycle is the temperature difference between the hot and cold stages, it increases as the temperature difference becomes bigger. Comparing to fossil sources, the temperatures produced by collecting the sun's radiations in current CSP designs do not reach the same levels as the temperatures achieved in coal or natural gas plants, so the efficiency of the Rankine thermodynamic cycle in a CSP plant is lower than the one of a non-renewable source plant.

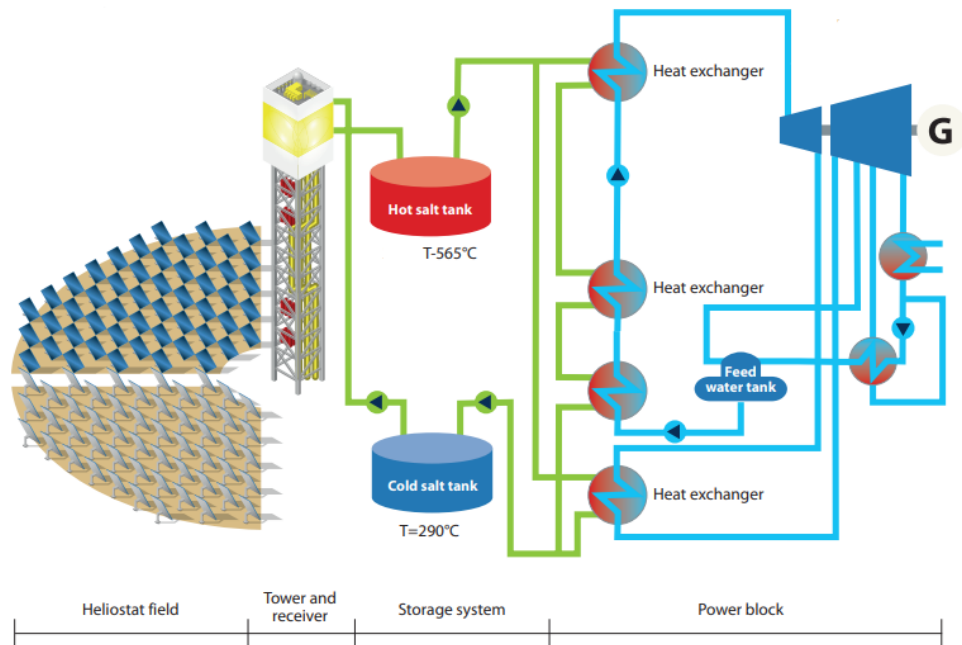


Image taken from [2]

Figure 1.3: Schematic of a central receiver CSP plant

Looking forward, the next generation of CSP plants are focused on elevating the working temperature of the hot molten salt to solve the efficiency problem compared to traditional sources. Higher temperatures bring new challenges such as testing new materials with high resistance at high temperature or finding solutions to deal with corrosion damage, as molten

salts are cost effective and have excellent thermal properties, but exhibit severe corrosion at high temperatures, even for stainless steels.

Therefore, research is focused on the search for strategies to improve the corrosion behavior of materials and on the testing of different materials to quantify their corrosion rates and corrosion damage under certain conditions, in order to be able to predict and increase the lifetime of the different components of a solar thermal power plant. Once materials resistant to high temperatures and with sufficiently good corrosion behavior are found, it will be a big step forward for the reliability of the CSP plant as a major source of renewable energy.

1.2 Objectives

Considering the challenges of CSP next generation, this study will focus on the lifetime prediction of CSP components. As a part of the project *Solar GNext* [3], in MSM (Materials and Solid Mechanics) and MMS (Metallic Materials Science) research teams of Uliege, different modelling techniques were developed:

- The master thesis of Julien Heremans [23] consisted of an elastic model with a coupling of mechanical and corrosion behaviour from a microscopic approach, using oxygen concentration as a degree of freedom of his model.
- The research work of Hélène Morch [24] which focused on the degradation of the tubes of the solar receivers due to corrosion with the molten salt. In this model, corrosion is considered from a macroscopic approach since it is a damage type thermo-mechanical model.

The model developed by Julien Heremans has corrosive concentration as a degree of freedom to better model the diffusion, while it was intentionally not the case in the model of Hélène, whose model focused on the thermo-mechanical modelling of Haynes 230.

Therefore, the main goal of the present master thesis is to use the model of Julien Heremans which will model better the diffusion of oxidizing species into the material due to his microscopic approach to find the optimal parameters in terms of corrosion damage to improve the model of Hélène Morch.

To have valid results with this multiscale comparison, it must be ensured that both models are operated under the same conditions and take advantage of the fact of behavioral coupling in Julien's model to calibrate the corrosion damage variable of the model developed by Hélène which will allow to have an even better lifetime prediction for the project *Solar GNext*.

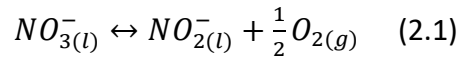
2 Fundamentals of corrosion

Before starting to discuss the two models and their results in terms of corrosion damage. Firstly, an introduction to molten salt corrosion should be given so that the reader can better understand the principles of this problem and the motivation of this work.

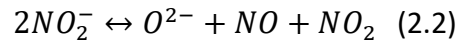
Currently, the molten salt mainly used in CSP plants as HTF is the binary nitrate molten salt (60% NaNO_3 and 40% KNO_3) [4-6] called Solar Salt, which has a working range of 290°C to 570 °C. Corrosion using a binary nitrate molten salt is observed on materials used in solar plant components: solar receiver tubes, collector, piping... Taking into account that these components are working under high temperatures, it is not only needed a stainless-steel type, but also resistance to high temperatures. Therefore, nickel-based alloys are being used and studied for the next generation of CSP plants as they meet these requirements, so in this study this type of alloy will be also selected as the container material subjected to corrosion.

2.1 Salt degradation

Corrosion is accelerated by temperature due to the oxidation of materials and salt degradation. The thermal decomposition of solar salt and its equilibrium reactions have been extensively investigated and a variety of decomposition mechanisms are reported [7]. It is widely accepted that in a first step nitrate ions (NO_3^-) decompose to form nitrite ions (NO_2^-) under the release of oxygen (2.1).



In the second step, the nitrite ion further decomposes to form oxide ions. A reaction, most referred to as a possible decomposition mechanism for nitrite, is the formation of metal oxide, accompanied by the evolution of NO and NO_2 (2.2).



It must be mentioned that the exact stoichiometry of Equation (2.2) has not been determined experimentally and may also depend on atmospheric composition. Corrosion using molten salt is a complex process and there are plenty of reaction paths behind corrosion that depend on various factors such as the temperature or the working atmosphere, so in this state of the art

only the basics of corrosion will be explained in order to not study in more detail than necessary this topic, to have an explanation easy to follow for a reader not specialized in this field.

It has been previously mentioned the working range of Solar salt (290 °C to 570 °C). P. Gimenez and al. [8] performed an analysis on the thermal degradation of Solar Salt, evaluating the influence of different impurities. To determine the stability limit of the samples, a loss of 3% of its initial weight was set as a limit. Results are shown in Figure 2.1 and in Table 2-1 and explains why the working range of Solar Salt is up to 570 °C since it is close to its stability limit (630 °C).

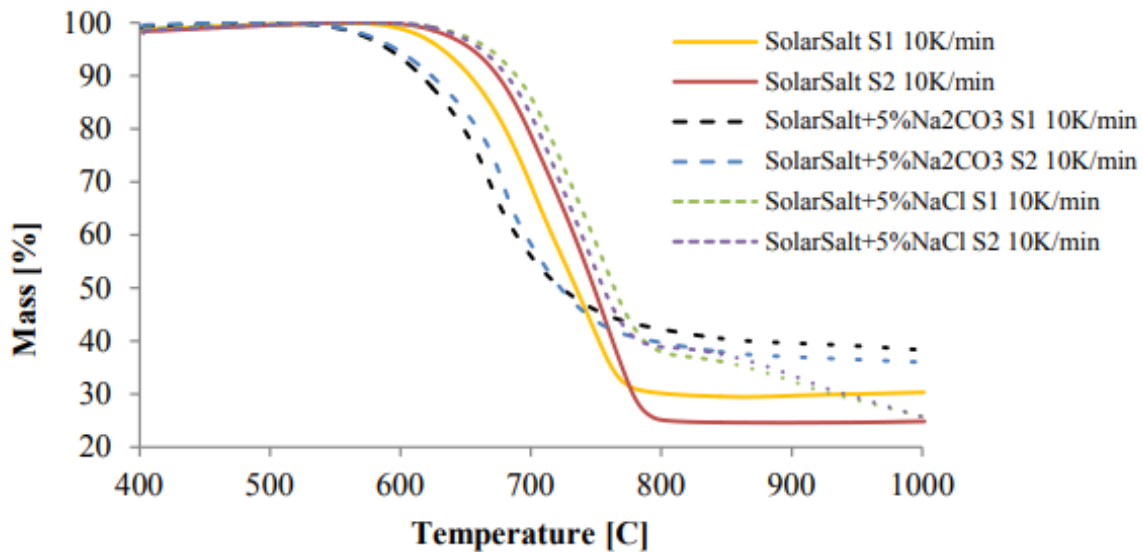


Figure 2.1: Mass evolution of Solar Salt samples

Composition	Stability limit (°C)
Solar salt	630
Solar salt + 5% Na_2CO_3	579
Solar salt + 5% $NaCl$	651

Table 2-1: Stability limits of Solar Salt samples

However, the stability limit does not influence only the working range. Within the working range, the closer the temperature is to the stability limit the more oxide species are released into the salt mixture and, therefore, this affects the salt degradation. This phenomenon has been studied in various investigations [9], where salt degradation of Solar Salt in contact with container materials has been measured at different temperatures.

As a conclusion of this study, it was stated that the volume rate of formation of nitrogen oxides increases with an increasing temperature, especially when the temperature is the closest to the stability limit since the release of this oxide species grows exponentially as shown in Figure 2.2.

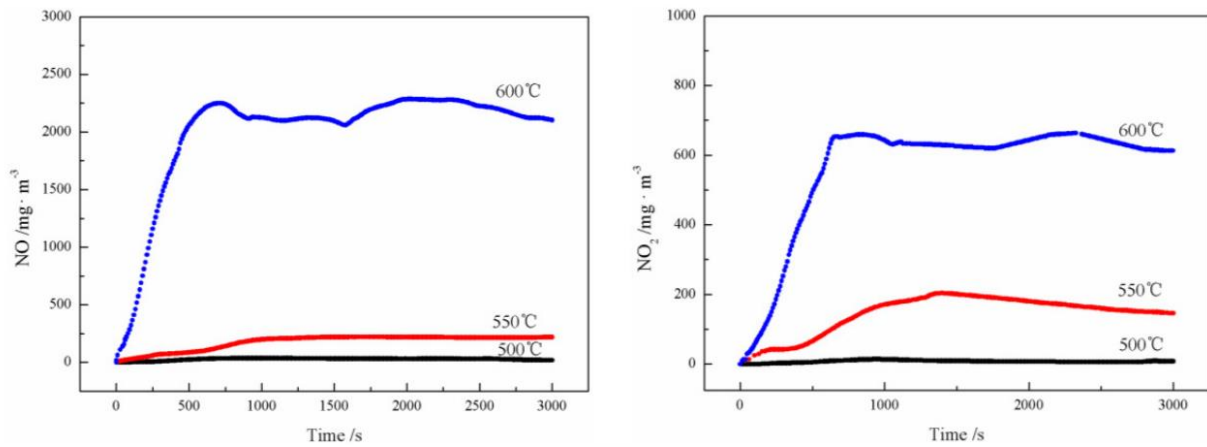


Image taken from [9]

Figure 2.2: Volume changes of NO (left) and NO₂ (right) vs. time and temperature with quartz

The volume change of these oxide nitrogen species is measured in order to quantify the salt degradation since their presence has a major impact in the corrosion of storage materials due to an acceleration of the oxide reactions and, therefore, the corrosion mechanisms in these steels. The release of oxide species doesn't depend exclusively on the temperature, due to this, different investigations have measured the volume change and the salt degradation depending on other factors such as the working atmosphere (Figure 2.3) or the container material itself.

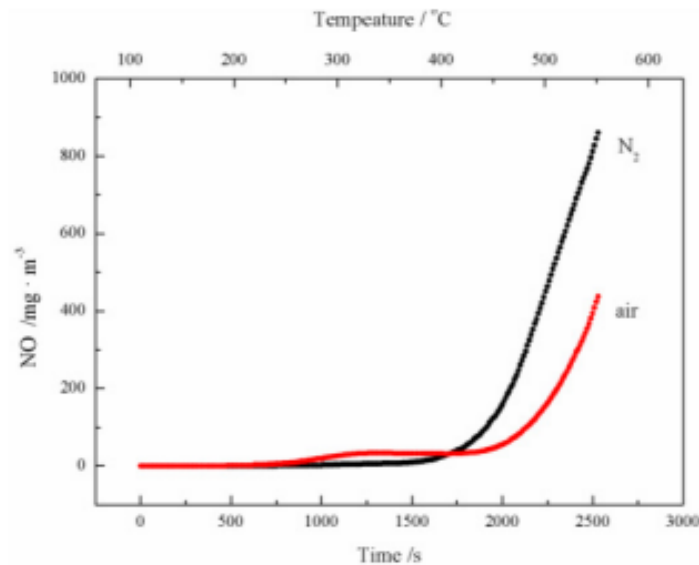


Image taken from [8]

Figure 2.3: Volume change of NO under different working atmospheres with SS316

2.2 Material corrosion

Once it has been reviewed the molten salt decomposition, mentioning its oxidation reactions and the different factors that have an influence in this process, it is time to discuss the other factor that participates in the corrosion with molten salt, the storage materials, and their corrosion mechanisms.

The corrosion of stainless steels is usually quantified by measuring the specific mass change [Δm (gr/mm^2)] or by the corrosion rate of the oxide scale ($\mu m/year$). In spite of using the corrosion rate to measure, the oxide scale originated is not homogeneous, in fact, it is based on a morphology of multiple oxide layers formed by protective and non-protective layers. The corrosion mechanisms that act in the formation of this oxide scale vary depending on the material used and by modifying the conditions such as temperature, salt purity, working atmosphere, etc.

For instance, Heng Li. Et al. [10], tested 304 and 316 austenitic stainless steels at different temperatures in order to understand how the temperature influences corrosion rates and corrosion mechanisms in long term exposure. As a conclusion, it was stated that temperature's increment not only affects the corrosion rate but also the corrosion mechanism. Figure 2.4 shows the corrosion mechanisms and reactions that happen in these two steels and how the protective scale of Cr_2O_3 decreases with an increasing temperature. Also, as the oxide scale becomes thicker, the probability of defects like voids and microcracks is higher, because of that, there are defects in both steels at 600 °C.

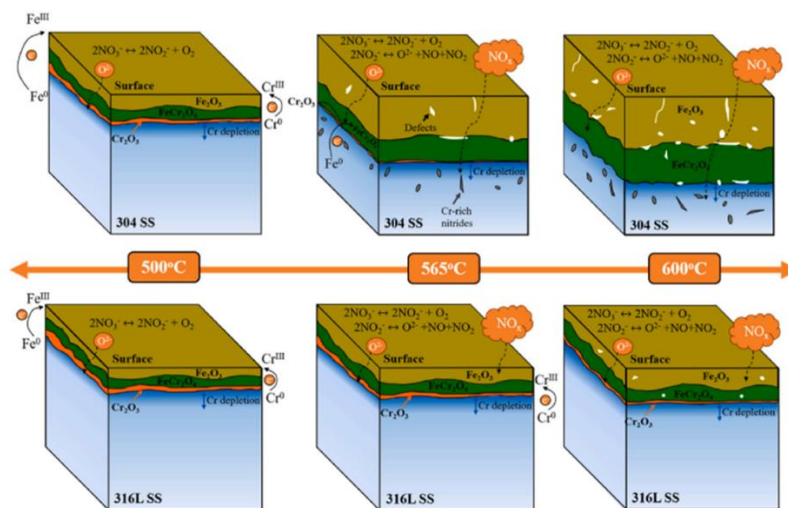


Figure 2.4: Corrosion mechanism of 304 and 316L SS at different temperatures

In addition, Figure 2.4 also shows how the two steels have a different corrosion behaviour. For instance, nitridation only occurs on 304 SS at high temperatures (565 °C and 600 °C). Talking

Image taken from [10]

about the decrease of the protective scale of Cr_2O_3 , this phenomenon is more significant in 304 SS, even disappearing this layer at 600 °C. Moreover, for 316L SS, the corrosion is controlled by the ion's transportation through the oxide layer, however, the corrosion process for 304 SS is controlled by the diffusion of oxidant in molten salts at 565 °C and 600 °C. All this evidence makes it clear that the corrosion behaviour depends on the temperature of molten salts and the chemical compositions of the substrate, as the 316L SS has a better corrosion behaviour.

Considering that the chemical composition has a major influence in the corrosion behaviour, austenitic, ferritic, and nickel-based alloys were tested under dynamic conditions, performing under short thermal cycles seeking to reproduce as closely as possible the actual condition of a CSP plant [11]. Apart from other conclusions, the test showed that nickel-based alloys have superior corrosion behaviour under realistic conditions compared to the other steels.

Once the test was finished, each type of stainless steel showed a different oxide scale morphology with layers formed by different components that should be explained in more detail due to the complexity of corrosion in the actual dynamic conditions of a CSP plant, since it involves the superimposition of several different phenomena. However, the three groups exhibit some common corrosion mechanisms under dynamic exposure in molten nitrates:

- Cr dissolution into the salt melt.
- Nitridation of the alloy surface.
- Scale damage due to thermo-cyclic conditions and re-healing of the scale.
- Surface recession due to dynamic conditions.

These phenomena all result in the depletion of Cr in the alloy and finally lead to breakaway corrosion involving the formation of fast-growing, non-protective oxide scales. Chromium plays a big role in the protective corrosion behaviour of the stainless steels so when its level has been reduced below a critical concentration for healing, this leads to breakaway corrosion, which involves a rapid growth of oxide scales and cracking or (partial) spalling of the surface oxide layer occurs [12].

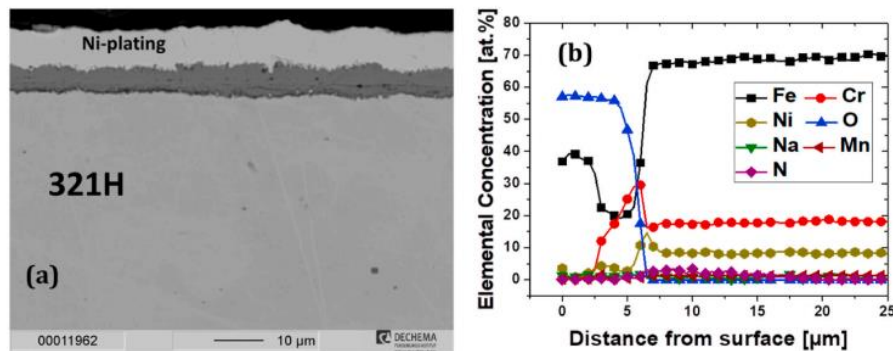


Figure 2.5: (a) Cross sectional image of 321H alloy; (b) Element concentration profiles of 321h alloy

Image taken from [11]

All alloy groups exhibited *Cr*-depletion to a certain extent, Figure 2.5(b), especially at higher exposure temperatures near 600 °C. This depletion of *Cr* at the alloy surface was associated with the formation of chromates upon either reaction of metallic *Cr* with nitrate anions or the basic fluxing of chromia scales and their dissolution into the salt melt. Both mechanisms result in the formation of highly soluble, toxic chromate species that enrich in the nitrate salt melt over time.

Regarding other factors such as chloride impurities in the molten salt, many studies demonstrated how its presence leads to much higher corrosion rates and more severe corrosion mechanisms [13-14]. Again, it has been seen that there are plenty of factors that affect not only the corrosion behaviour of stainless steels, but also the salt decomposition, Figure 2.6.

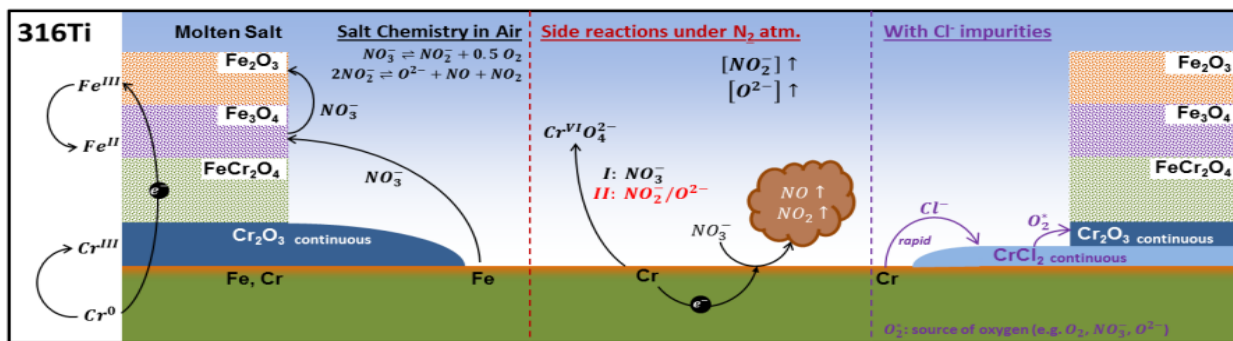


Figure 2.6 Corrosion mechanisms depending on the working atmosphere and Cl^- impurities for 316 Ti

Therefore, there are still great research efforts in this field in order to better understand the phenomena behind corrosion and to obtain updated corrosion data, especially under dynamic conditions since it is a situation closer to the actual one in a CSP plant. Another conclusion of the corrosion literature review is that nickel-based alloys have the best corrosion behaviour and that's the reason why this alloy type is selected as the storage material to be studied in both models in this master thesis.

2.3 Corrosion modelling

Corrosion plays a significant role in the lifetime of the components of a CSP plant due to the oxide layer generated and the damage that occurs, as it has been seen above. Therefore, it is important for the designing stage to have reliable models which predict how the different compounds will behave when exposed to cyclic loading at high temperatures as occurs in these types of solar plants, taking into account the oxidizing aspect of these environments. In addition, since CSP plants require huge investments, not only are the different parts required to be able to work with

cyclic loads under these conditions in the short term, but also to guarantee a long service life so that the plants can operate profitably.

Therefore, these models, apart from calculating the mechanical behavior, must also be able to quantify the damage that the material suffers during its use (either damage due to fatigue, creep or corrosion), in order to have a prediction of the damage evolution and to have a reliable guarantee of its useful life before its installation. To meet this need, various corrosion models with different approaches have been developed in recent years.

Since corrosion modelling is directly related to the objective of this master's thesis, a review of the currently available literature on this topic has been carried out. Therefore, two types of models found in literature will be explained in the following sections.

2.3.1 Diffusion models

Diffusion models aim to simulate the progress of the penetration of oxidizing species into the analyzed material. These models can be split in 2 categories:

- Microscopic models: These models follow the changes in the material at the microscopic level. They model how the corrosive elements penetrate the material and how it affects the material's behaviour.
- Macroscopic models: These models use diffusional laws to set the velocity of a mobile boundary between the material and the corrosive environment, simulating the material loss due to uniform corrosion.

As a reference of the first group, a microscopic model was developed [15], which simulates the transport of oxygen into the material and the associated internal oxidation under fatigue-oxidation conditions. The model considers grain boundaries as the primary path for oxygen diffusion and a coupled mechanical-diffusion analysis is adopted to account the influence of loading into the diffusion, as described by the following constitutive law:

$$\frac{\partial C}{\partial t} = \nabla(D\nabla C - DCM\nabla P) \quad (2.3)$$

C is the concentration of oxygen, t the time, D the oxygen diffusivity, P the hydrostatic stress and M the pressure factor. As it is shown in equation (2.3), there is influence of mechanical stress on the mass transport and if the pressure factor $M = 0$, the equation is reduced to natural diffusion.

$T (^{\circ}\text{C})$	$D (\text{mm}^2/\text{s})$
650	$1.085\text{e} - 13$
700	$1.397\text{e} - 12$
750	$5.859\text{e} - 12$
800	$1.423\text{e} - 11$

Table 2-2: The oxygen diffusivity at four temperatures

The diffusion parameters considered in this model (D & M) were calibrated based on measurements of oxide scale to estimate the internal oxygen penetration. These measurements were taken at different temperatures, and it can be noticed the great dependency of both parameters on temperature, Table 2-2 & Table 2-3. It should be mentioned that both the diffusion coefficient and the pressure factor are material-dependent values and that the experiments and the model are performed considering a nickel superalloy as material.

$T (^{\circ}\text{C})$	$M (\text{MPa}^{-1})$
650	0.001585
700	0.0098
750	0.068
800	0.188

Table 2-3: The pressure factor at four temperatures

From Table 2-3, it can be stated that the mechanical influence on the oxygen diffusion increases significantly since the pressure factor M rises with an increasing temperature. Results of the model in terms of oxygen concentration are shown in Figure 2.7, using the grain boundaries as a diffusion path, and comparing the deeper oxygen penetration with a high-pressure factor than with a natural diffusion situation.

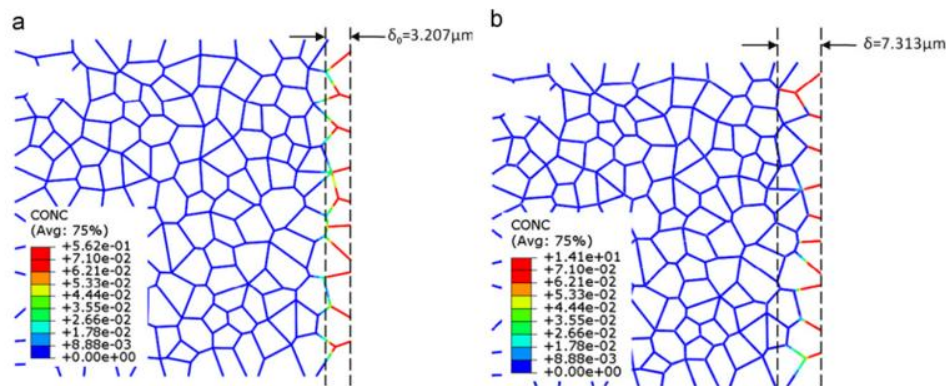


Figure 2.7: Simulated oxygen concentration at 800°C after 33,475 cycles for (a) natural diffusion and (b) a pressure factor of 0.3 MPa^{-1}

Moreover, this model also allows us to predict the rate of crack propagation when there is some oxygen concentration around a fatigue crack tip and to quantify the embrittlement near the crack tip due to oxidation.

Regarding the macroscopic models, there are some models in the biomedical field that take this approach using magnesium alloy as a material. The aim to use corrosion models in this field is to simulate if prosthesis, to replace body parts which have been lost due to disease or injury, made of magnesium alloy could tolerate the corrosion that entails the environment inside an organism. An example of this biomedical approach is the model developed in [16], which is based on the finite element method using an adaptive mesh whose boundary is mobile.

Boundary movement simulates the rate of retreat of the corrosion surface which is modelled by specifying a uniform corrosion rate. This corrosion rate is governed by the diffusion of metallic ions from the corrosion surface according to the Fick's law (2.4), being similar to the heat equation in a convection situation.

$$\frac{\partial c}{\partial t} = \nabla(D\nabla C) \quad (2.4)$$

Therefore, this model has the concentration of magnesium as a degree of freedom and its diffusion sets the velocity at which the mesh boundary moves, Figure 2.8. To implement this mobile boundary is used the Arbitrary Lagrangian-Eulerian (ALE) adaptive meshing functionality which allows moving boundary problems to be solved and is compatible with some commercial finite element software.

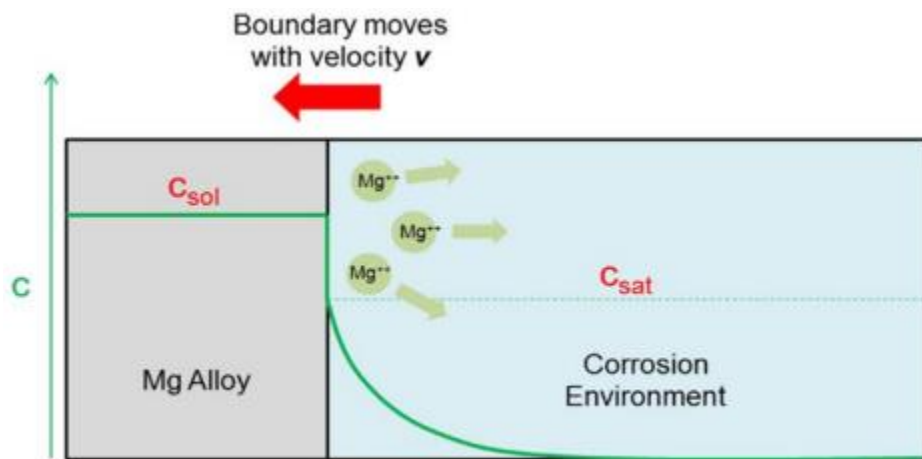


Image taken from [16]

Figure 2.8: Sketch of the assumed corrosion process and the boundary condition

Another model in the biomedical field with the same approach is the one developed in [17]. As the previous model, it uses a finite element method with a mobile boundary (Figure 2.9) based on the magnesium diffusion, according to the Fick's law (2.4).

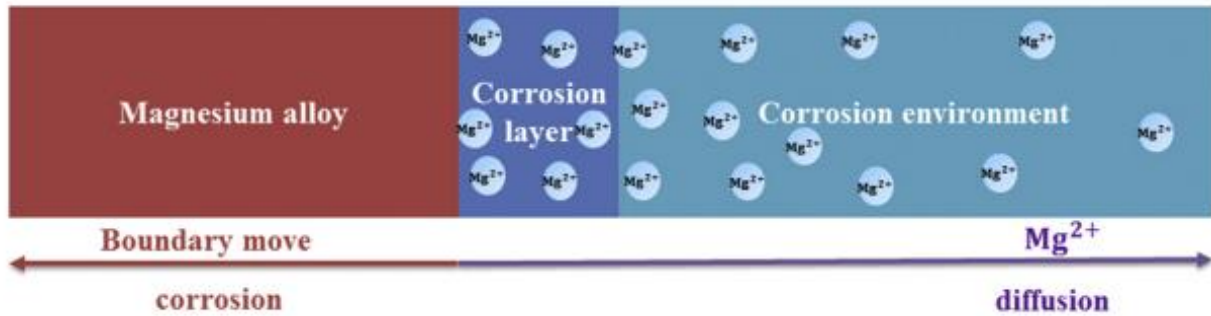


Image taken from [17]

Figure 2.9: Schematic diagram of magnesium alloys corrosion

The goal of the model is to characterize the degradation behaviour of the magnesium alloys in a quantitative manner to improve the estimation of the lifetime of this promising biocompatible material, based on experimental data, Figure 2.10. ALE functionality is used again to implement the boundary mobility condition in the finite element method.

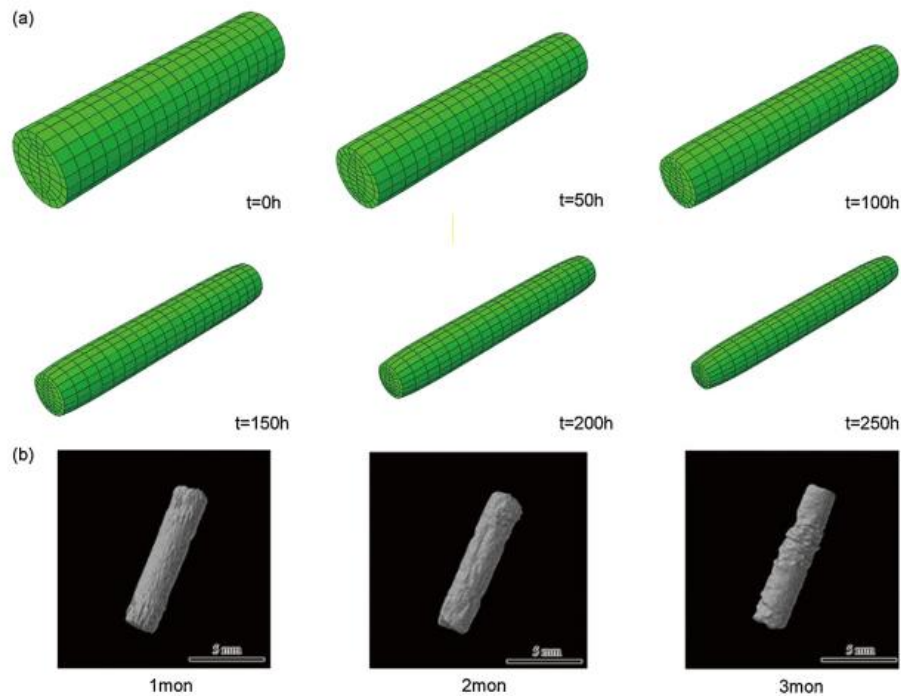


Image taken from [17]

Figure 2.10: Morphology feature of the Mg alloy pin over time: (a) simulation, (b) experiment

2.3.2 Damage variable models

The advantage of this type of model is that it does not focus on the propagation of oxidizing species within the material but on the concept of corrosion damage. Therefore, it is compatible with already developed mechanical models since it only requires the implementation of the corrosion damage variable.

The first steps in this direction were taken by the model of Neu and Sehitoglu [18]. Their model consists of a life prediction for crack nucleation and early crack growth considering three possible damage mechanisms: Fatigue, environmental attack (oxidation) and creep. The different damage variables are computed independently and to obtain the total damage per cycle, these three mechanisms are summed as in equation (2.5):

$$D^{tot} = D^{fat} + D^{ox} + D^{creep} \quad (2.5)$$

Assuming linear damage and damage is equal to 1 at failure, equation (2.5) could be rewritten in terms of the failure life, N_f , since damage is equal to $1/N_f$.

$$\frac{1}{N_f} = \frac{1}{N_f^{fat}} + \frac{1}{N_f^{ox}} + \frac{1}{N_f^{creep}} \quad (2.6)$$

As each variable is calculated independently, depending on the conditions, one mechanism or another will control the life. For instance, if the temperature is too low, the fatigue will be the main mechanism.

Each mechanism has different material constants and parameters:

- The fatigue damage is based on the strain-life equation with constants determined at room temperature.

- The creep damage is based on stress, temperature, strain-temperature phasing, and time.

- The oxidation damage is a function of mechanical strain range, strain rate, strain-temperature phasing and oxidation kinetics, which follows a parabolic law due to the decreasing oxidation rate according to literature, Figure 2.11.

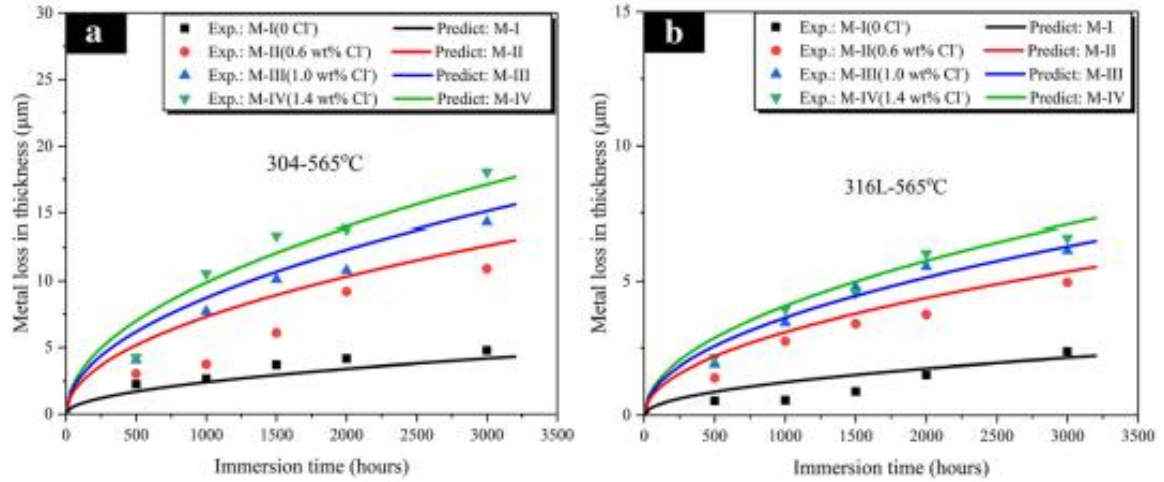


Figure 2.11: Comparison of metal loss between experimental data and a parabolic model for 304 SS and 316 L at 565 °C

More recently, it was incorporated the concept of corrosion damage induced by stress (D^{SCC}) [19] (S and R are material/environmental parameters) and set a critical damage value. When this value is reached, the damage changes instantaneously to 1, modelling a fast unstable fracture.

$$D^{SCC} = \left(\frac{\delta\sigma}{1-D}\right)^R \quad (2.7)$$

Later on, it was used the same model with the addition of uniform corrosion damage (2.8) and introduced the deactivation of elements when critical damage is reached in an element [20], known as “death element technique”.

$$\dot{D}_u = \frac{\delta_u}{L_E} K_u \quad (2.8)$$

Where δ_u is a characteristic dimension of the corrosion (e.g., the critical thickness of the corrosion layer); L_E the characteristic length of the element and K_u a parameter linked to the kinetics of corrosion.

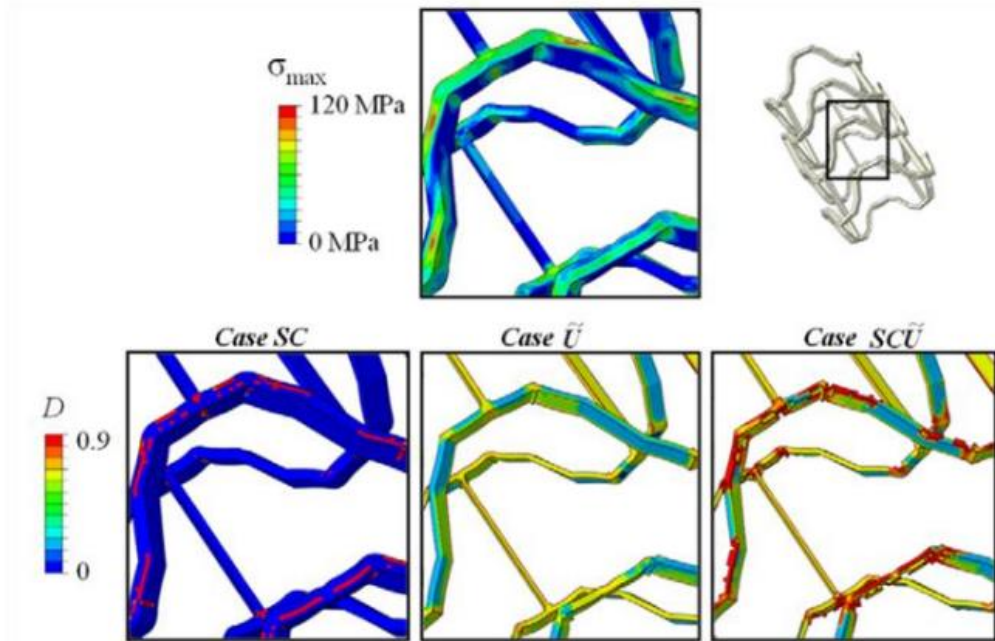


Image taken from [20]

Figure 2.12: Corrosion of a stent in the human body with consideration stress induced corrosion (SC), uniform corrosion (U), or both (SCU)

Although some of the models reviewed are oriented to the biomedical field, they can be easily adaptable and serve as a good reference for corrosion modelling in the context of molten salt corrosion in CSP plants as they are based on the same fundamentals.

3 Models

In this chapter, before starting to show results, we will describe the two models that this thesis aims to compare in order to understand both the similarities and differences between them. In addition, during the description we will see the limitations of the model and the reason why it is useful to perform this coupling.

3.1 Lagamine model

The research work of H  l  ne Morch is based on a thermo-mechanical model which was implemented in the finite elements code *Lagamine* of the University of Li  ge to model the tubes of the solar receivers of a CSP plant [21]. *Lagamine* is a 3D finite element calculation software which makes it possible to impose different laws on a material, and to observe the stresses, displacements, deformations in each element of the mesh.

Therefore, the behaviour model is used to compute the stresses and strains in a tube when thermal loading is applied, in order to simulate the conditions of the solar receivers. For instance, Figure 3.1 shows the stress distribution of the von Mises stress in a section of the tube (only half of the section is modelled because of the symmetry). The radiation from the sun coming from the right in the picture leads to an increase in temperature on this part of the tube, whereas the other side of the tube remains at lower temperatures.

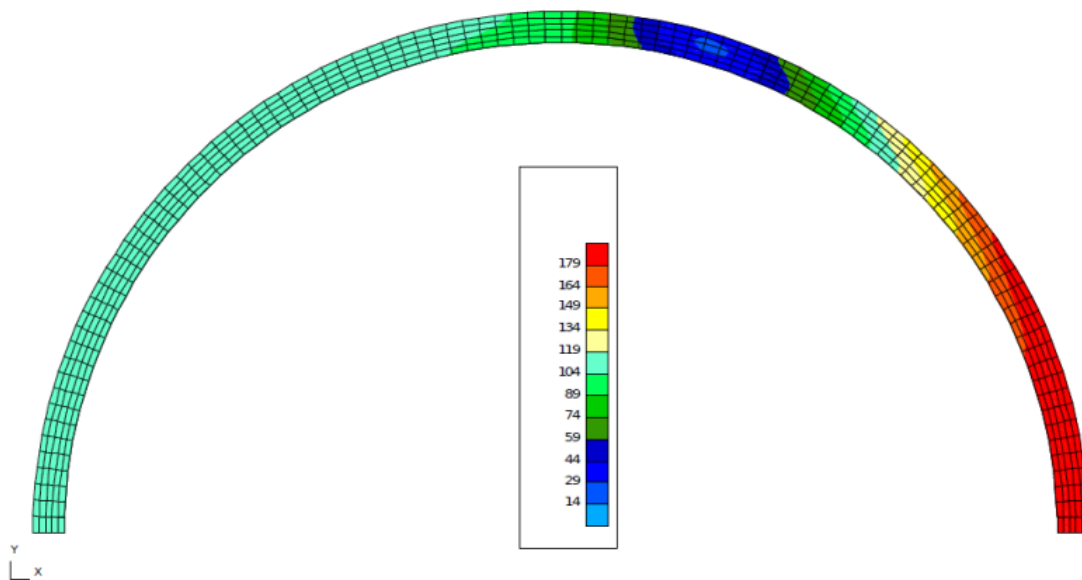


Figure 3.1: Von Mises stress [MPa] in the tube under thermal loading

The difference of temperature leads to a difference in thermal expansion between front and back. Since the tube is fixed and must remain straight, the thermal deformation is compensated by a mechanical deformation, which generates stresses in the tube as can be seen above.

3.1.1 Lagamine software

Lagamine doesn't have a graphical interface, so input data is introduced with different text files that can be modified manually by the user. For this program, there are several types of text files which each have their own function:

- The file_ex.dat, containing information about the execution of the simulation, such as the simulation time, the size of a time step, the calculation method, the parameters of convergence, the time steps at which the results are saved, etc. (Simulation parameters).
- The .lag file, which contains data concerning geometry (the position of nodes and mesh elements), material laws, initial conditions, boundary conditions, etc.
- The .dep file, used to define the imposed displacements according to time.
- The .lic file to define the forces imposed according to time.
- The .pri file which indicates the variable to be displayed. The results shown are pure numerical.

These are the main files that have been used during the comparison, but the software has more types with specific functions which allows the user to perform simulations with all kinds of boundary conditions or loads (constant, cyclic, progressive, etc.) thanks to this variety and flexibility of the software.

3.1.2 Mechanical behaviour

To model the mechanical behavior of the solar receiver tubes in their working cycles at high temperatures, this model takes into account several laws, such as the Chaboche's elasto-visco-plastic behaviour law which is used for solid elements, evolving at constant or variable temperatures, considering cyclic work hardening, visco-plasticity, material damage, etc.

According to this law, many material parameters such as the Young's modulus, the yield stress or the dilatation coefficient depend on the temperature of the material, following an exponential equation type (3.1). So, if a variable temperature is fixed, the properties of the material will change during the simulation.

$$P(T [^{\circ}\text{C}]) = A_P \left(1 - B_P \cdot \exp\left(\frac{T [^{\circ}\text{C}]}{C_P}\right) \right) \quad (3.1)$$

Where A_P , B_P and C_P are material coefficients that can be fixed and modified in *Lagamine*. The influence of the temperature in these parameters is significant, as the goal of the solar receiver of the next generation of CSP plants is to operate at temperatures up to 850°C. Figure 3.2 shows the relation between the Young's modulus and temperature for a nickel-based alloy, Haynes 230.

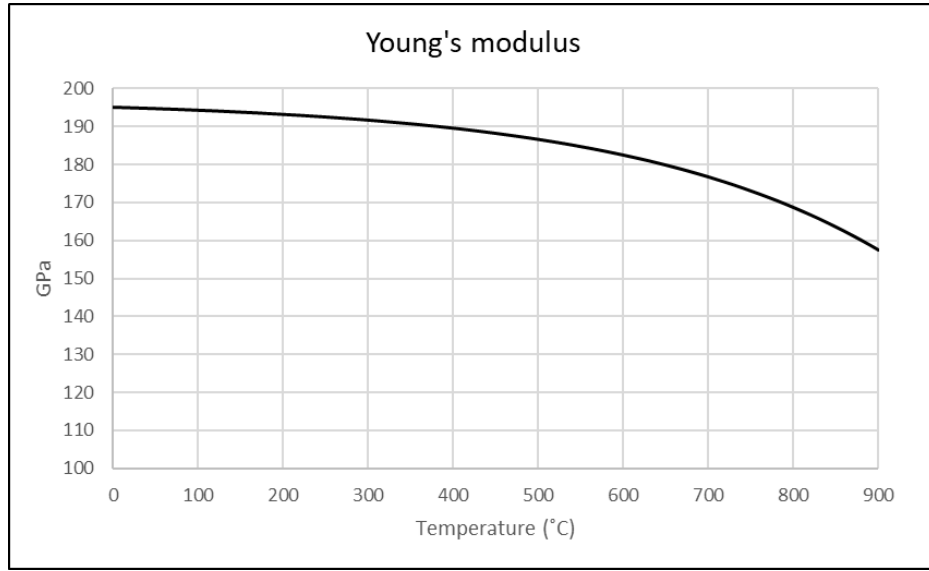


Figure 3.2: Young's modulus of nickel-based alloy Haynes 230 depending on the temperature based on (3.1)

Also, the model considers a thermal conduction constitutive law which simulates the heat transfer by conduction and heat accumulation in solids and, since this model is a damage type thermo-mechanical model with the goal of obtain a lifetime prediction of the tubes, it is considered the damage generated by the stresses and strains at these high temperatures. Two types of mechanical damage can be identified:

- Fatigue damage (D_f) linked to the cyclic nature of the loading in a CSP plant (the thermal loading is repeated every day due to sunlight and nighttime periods).
- Creep damage (D_c) related to the duration of the loading at high temperatures (every day, the stresses in the tube are maintained for several hours).

The damage generated deteriorates the mechanical behaviour of the material and the total damage is the result of the sum of the different damages (3.2). The damage variable is equal to 0 when the material is intact and 1 when the rupture occurs.

$$D_{tot} = D_f + D_c \quad (3.2)$$

In the model, a critical damage is set (usually, $D_{critical} = 0,3$) and when this value is reached, the simulation is stopped because it is considered that the material is very close to an unstable rupture, so the damage increases exponentially to 1. This approach using critical damage had already been mentioned in the previous chapter when performing the modelling review.

To model the influence of damage on the material behaviour, the effective stress $\tilde{\sigma} = \frac{\sigma}{1-D}$ can be used. This effective stress corresponds to the stress that should be applied to the non-damaged material to obtain the deformation ε [22], Figure 3.3.

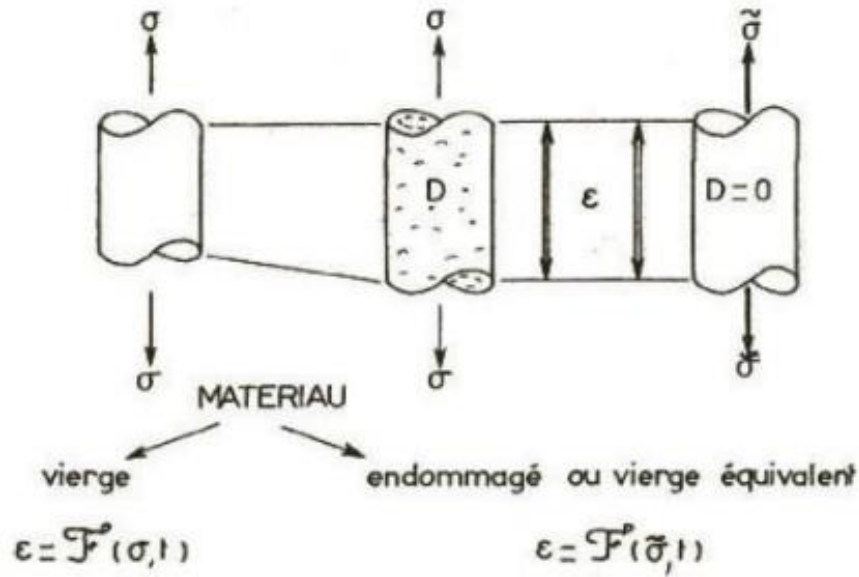


Figure 3.3: Representation of effective stress

3.1.3 Corrosion behaviour

In terms of corrosion modelling, this model chooses to use the damage variable model approach, previously explained in chapter 2. Therefore, to include the corrosion behavior in the model, the corrosion damage variable (D_u) is simply added to the total damage equation, in order to characterize the additional damage due to uniform corrosion. Then, the new equation of total damage will be:

$$D_{tot} = D_f + D_c + D_u \quad (3.3)$$

The evolution of D_u is computed through a linear law:

$$D_u = \frac{k_u \cdot t}{L_E} \quad (3.4)$$

Or using a parabolic law:

$$D_u = \frac{1}{L_E} \cdot \sqrt{2k_p t} \quad (3.5)$$

Where k_u , k_p are corrosion rates [m/s or m^2/s] (these parameters depend on the material and on the corrosive environment [air, solar salt, chloride impurities, ...], as seen in literature review); t is the time [s]; L_E is the characteristic length of the element; by default: $L_E = \sqrt[3]{V_E}$, being V_E the volume of the element.

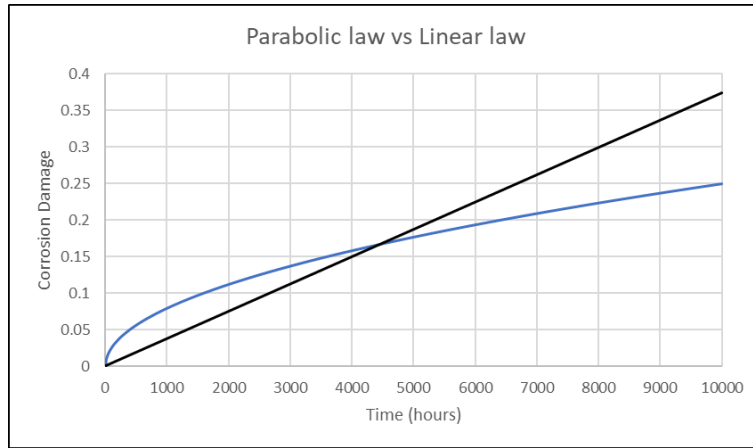


Figure 3.4: Comparison of Parabolic law and Linear law

Figure 3.4 shows how both corrosion laws evolve. In this work, the parabolic law will be used since, as it has been verified in the literature review, it is the one that best fits the experimental results, in which the evolution of the oxide layer is measured over time. This law is best suited because the rapid growth of the oxide at the beginning is slowed down by the creation of a protective oxide layer, which leads to a decrease in the corrosion rate and therefore in the damage.

This corrosion damage weakens the material in the same way as other types of damage. For instance, in the elastic domain the undamaged material will behave according to Hooke's law:

$$\sigma = E \varepsilon^{el} \quad (3.6)$$

So, if the damage is not equal to zero, Hooke's law can still be used but replacing the stress by the effective stress, as was done for the total damage before. Therefore, following the definition of effective stress, Hooke's law becomes:

$$\tilde{\sigma} = \frac{\sigma}{1-D_u} = E\varepsilon^{el} \Leftrightarrow \sigma = (1 - D_u)E\varepsilon \quad (3.7)$$

Thus, it is equivalent to reducing the value of Young's modulus by a factor $(1 - D_u)$, as will be seen in the next chapters in the simulation results.

3.1.4 Model review

The work developed by Hélène Morch is a very complete model at the mechanical level and allows testing of materials using and modifying both boundary conditions and load types. In addition, it takes into account the effect of accumulated damage on the material's mechanical behavior, thus serving as a very useful life predictor.

From the corrosion point of view, this model adopts a simpler approach, using a parabolic damage law based on the corrosion rate. However, this model does not simulate how corrosion diffuses into the material, taking into account only the influence of corrosion damage on the material of the elements previously selected at the start of the simulation. Therefore, in a situation where reliable experimental results are not available or it is not known precisely how and where corrosion develops, this model may not give optimal results in terms of corrosion damage.

3.2 Diffusional elastic model

This model was created by Julien Heremans as a result of his master's thesis [23] at the University of Liège with the aim of modelling the coupling between corrosion diffusion and the mechanical behaviour of metal alloys. A non-fickian diffusion process was considered to interact with a two-dimensional linear elastic mechanical model, assuming a plane stress state.

3.2.1 Software

The diffusional elastic model is a finite elements code written in the Fortran language created in the code editor *Microsoft Visual Studio*. As the Lagamine model, this one does not have a graphical interface either, so it is again necessary to handle text files to use this model and modify its parameters.

- The .par file, which contains the value of the load that is applied to the material and all the material parameters required by the model. Being a linear elastic model, from the mechanical point of view these parameters are reduced to the Poisson ratio, the Young's modulus for undamaged material and the Young's modulus for the damaged material. And from the corrosion point of view, the only material parameters are the corrosion diffusivity and the pressure factor. (Load, ν , E_o , E_d , D and M).
- The .msh file, which contains data concerning the mesh and geometry (the position of nodes and elements). In this file also the boundary conditions are defined, stating which nodes are fixed in a certain direction or at which points the previously defined load value is applied.
- All program code and subroutines are in the *Microsoft visual studio* file. The rest of the model values have to be changed directly from the code. In this case, there are the simulation parameters (simulation time and time step), the value of the boundary conditions and the way in which the load is applied (progressively or constantly).

Once the simulation has been performed, the numerical results are obtained in another text file. As outputs of the program, the following values are obtained for the whole mesh and for each time step: Corrosive concentration c [%], displacements (u and v), stresses (σ_x , σ_y and τ_{xy}) and strains (ε_x , ε_y and ε_{xy}).

3.2.2 Mechanical behaviour

The mechanical model consists of a 2D isotropic linear elastic behaviour, considering a state of plane constraints. Therefore, dynamic effects and material plasticity are not taken into account. It should be mentioned that this model shows the stresses as a function of the nodes and not of the elements, since the stresses are extrapolated from gauss points to the node. This solution was adopted by Julien due to practical considerations inherent to the post-processing software.



Figure 3.5 Element of 4 nodes (Quad4)

So, the Fortran code solves the equilibrium equations of the material considered at each time step, using elements of 4 nodes, in order to determine the stresses, deformations and

displacements at each node of the mesh. It also incorporates a damage law, which will be explained in the next section, that modifies the mechanical behaviour of the model according to corrosion. In conclusion, it is a simple elastic mechanical model with certain limitations that have to be taken into account when comparing it with the Lagamine model.

3.2.3 Corrosion coupling

As already mentioned, this model uses the diffusional approach to model corrosion, thus using a non-fickian diffusion process as the model stated in [13], incorporating a stress-driven diffusion factor, whose amplitude is conditioned by the material pressure factor, seeking to model the influence of mechanical loading on the corrosion process.

$$\frac{\partial c}{\partial t} = \nabla \cdot (D \nabla c - D M c \nabla p) \quad (3.8)$$

Where c (%) represents a relative concentration in oxygen, p the isotropic pressure (MPa), D the diffusivity of the corrosion (mm^2/s) and M the pressure factor (MPa^{-1}). If the pressure factor is equal to zero, the corrosion will behave as a natural corrosion diffusion process. This natural process was validated by Julien based on experimental results of metallic alloys submitted to hot corrosion, without mechanical loading. Therefore, if it supposed a top corrosion in a rectangle mesh, the diffusion would have the following aspect, Figure 3.6:



Figure 3.6: Time evolution of natural corrosion diffusion

On the other hand, if the pressure factor is not cancelled out, the corrosion does not have this homogeneous evolution. Julien Heremans carried out several tests during his master's thesis in which the effect of stress-driven corrosion can be seen.

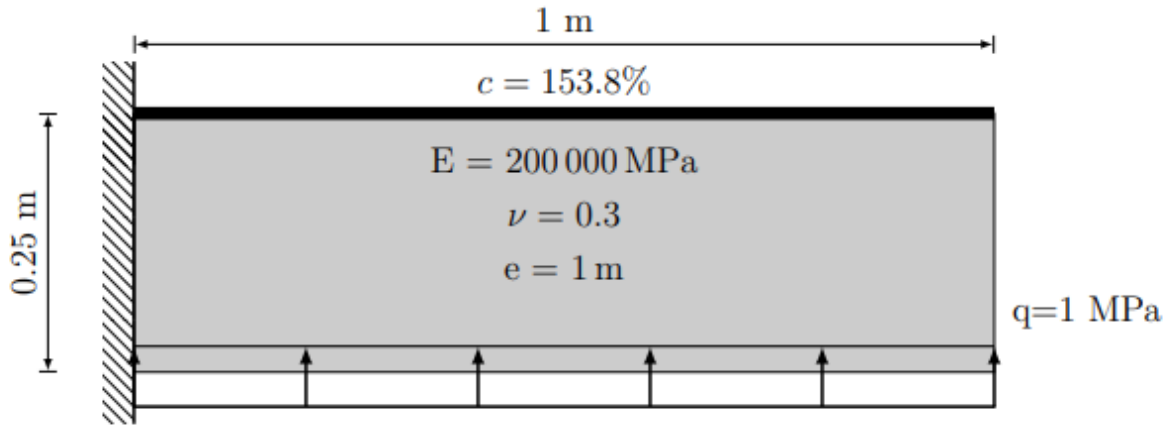


Image taken from [23]

Figure 3.7: Stress-driven corrosion test

Figure 3.7 shows an example of one of Julien's tests, in which the material is subjected to surface pressure of 1 MPa on the lower face and corrosion on the upper face. The initial oxygen concentration is set at 153.8%, it may surprise the reader that this is higher than 100%, but it should be remembered that this is a relative oxygen concentration with respect to a critical oxygen concentration, at which it is assumed that the material is already fully corroded (3.9).

$$c = [O_2]/[O_2]_{cr} \quad (3.9)$$

By observing the time evolution of the corrosion in this test, shown in Figure 3.8, it is possible to appreciate the different way in which the corrosion process takes place, especially in the lower part of the material at 1.5 seconds. This shows the influence that the pressure factor has on the diffusion equation and the sense of making this coupling of mechanical and corrosion behaviour.

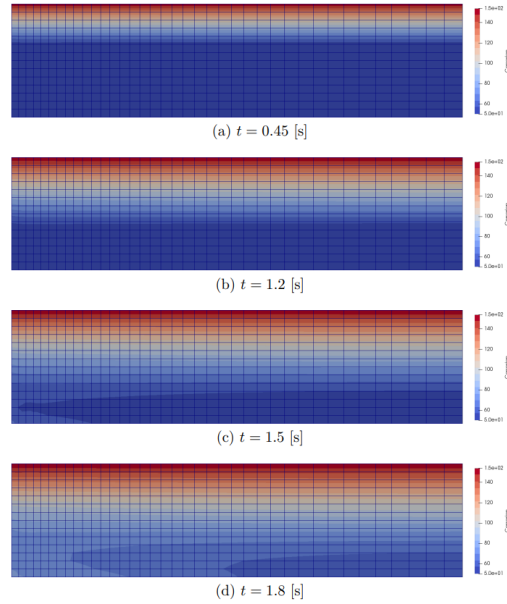


Figure 3.8: Time evolution of corrosion rate for the test

So far, the influence of the stress state on the corrosion behaviour has been explained, but the reverse has not been mentioned. This model also takes into account the deterioration of the mechanical behaviour due to the material corrosion, for which a damage law is used, modelling a linear degradation of Young's modulus with a damage variable.

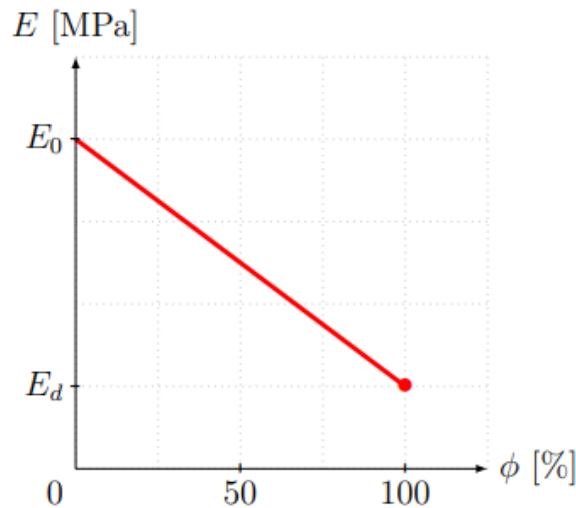


Figure 3.9: Degradation of Young's modulus as a function of damage variable

Figure 3.9 shows how the Young's modulus of the material decreases linearly until it reaches the residual Young's modulus (E_d) when the material is completely damaged. The relationship between this damage variable and concentration is shown in the graph below:

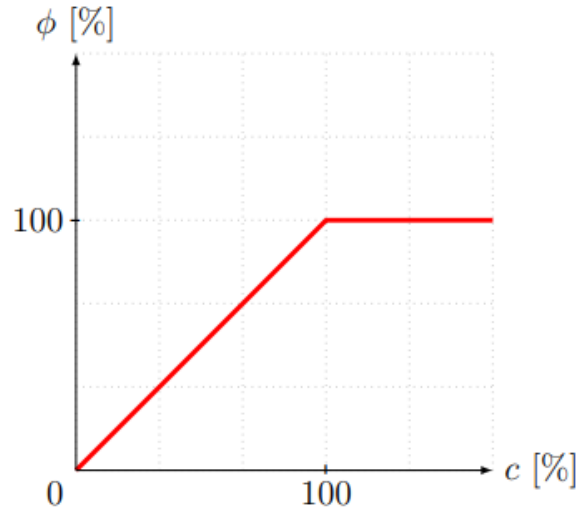


Image taken from [23]

Figure 3.10: Definition of damage variable ϕ respect to c

Considering that c can have values greater than 100% as previously observed, it makes sense to use an intermediate variable ϕ instead of c , to avoid lower values than the residual Young's modulus. Then, damage variable ϕ is equal to c in the bounded interval $[0,1]$. Summarising all these relationships, we obtain the following equations:

$$\begin{cases} \phi = c; & \text{if } c \in [0\%, 100\%] \\ \phi = 100\%; & \text{if } c > 100\% \end{cases} \quad (3.10)$$

So, the Young's modulus will follow this equation:

$$E^{eff} = \left[1 + \phi \cdot \left(\frac{E_d}{E_0} \right) \right] \cdot E_0 \quad (3.11)$$

Where E^{eff} is the Young's modulus given a ϕ [%], E_0 the Young's modulus for an undamaged material and E_d the Young's modulus for a completely corroded material.

3.3 Coupling of models

As explained above, on the one hand, the Lagamine model has a complex mechanical modelling that allows the application of many types of boundary conditions and loads due to its flexibility, however, from the corrosion point of view, it only uses a parabolic damage law to model the degradation of the material behaviour due to corrosion.

On the other hand, the diffusional elastic model has a much more detailed corrosion modelling that takes into account the influence of the stress on the corrosion behaviour, but a simple linear elastic mechanical model with several different models with some limitations at setting boundary conditions and types of loads.

Thus, by performing tests for both models under the same conditions, it is possible to find the optimal parameters for the damage law of the Lagamine model, obtaining more reliable results. However, it is necessary to take into account the limitations of each model in the corrosion and mechanical aspects in order to obtain accurate and reliable results.

4 Comparison of models

In this chapter, the process that has been carried out to perform both the mechanical and corrosion comparison is explained. Firstly, common boundary conditions and the type of test to be carried out will be established. Next, a first mechanical comparison without corrosion will be carried out to validate that the two models are mechanically compatible from the beginning. At the final stage, corrosion will be applied in both cases to compare both the corrosion damage and the mechanical behaviour.

4.1 Test conditions

When setting the test conditions, the limitations of each model must be taken into account, in order to be able to apply the same boundary conditions to both models. The Lagamine model enjoys a great flexibility as far as the mechanical model is concerned, however, the diffusional elastic model has many more limitations in this field as will be discussed, for instance, it is not possible to fix the displacement in one direction and, at the same time, impose a displacement in the same direction in another part of the mesh, since only one value per boundary condition is allowed in the input file.

Several of these limitations of the diffusional elastic model could have been avoided by making modifications to the model code. However, this required a minimum of knowledge in Fortran programming and further analysis of how the program code was made and structured. Since this was not the main purpose of the thesis and the time of the master thesis was limited, changes to the model were avoided as much as possible, adapting to the limitations of the model.

Therefore, in order to avoid major problems and to be easily reproducible for both models, a simple tensile test has been selected. The following sections will explain in more detail the characteristics of this test, which is carried out on a beam of 0.25 m high, 1 m long and 0.1 m deep (as the Lagamine model works in 3D).

4.1.1 Fixed displacements

For this tensile test, the displacements in the x-direction at the beginning of the beam and the displacements in the y-direction at the bottom face of the beam are fixed. These fixed displacements are shown in the 2D diagram in Figure 4.1. As the Julien diffusional elastic model is a 2D model, the displacements in the Z-direction of the rear face are additionally fixed in Lagamine.



To avoid any confusion with the symbology, these boundary conditions are shown explicitly in the following equations (4.1):

$$\begin{cases} u = 0; \text{ for } x = 0 \\ v = 0; \text{ for } y = 0 \\ w = 0 \text{ (In the case of Lagamine)}; \text{ for } z = 0 \end{cases} \quad (4.1)$$

4.1.2 Material properties

In the literature review it has been found that the group of nickel-based alloys have a superior corrosion behaviour compared to the rest of stainless steels, therefore for this test a material from this group is used, specifically Haynes 230.

It should be reminded that the aim of the next generation of CSP plants is to raise the working temperature of molten salt to above 700°C. At this temperature, the properties of the metal undergo some variation from their properties at room temperature. These considerations were taken into account by H  l  ne Morch and so her model incorporates all the parameters needed in Chaboche's law to model the change in properties due to temperature for Haynes 230 alloy. However, as Julien's model does not consider the effect of temperature, it is necessary to look at the constants introduced in the Lagamine model to calculate the material properties at a set temperature, to be introduced in the other model.

The test has been chosen to be performed at 700°C, since it is in the target working range of the next generation and literature data of the corrosion variables for the diffusional model are available for this temperature. Then, the values of the material properties to be introduced into the diffusional elastic model (the Young's modulus and the Poisson ratio) are calculated at 700°C. In addition, the yield stress will be calculated, in order to know in which load range it is possible to work, since, being an elastic model, we must remain exclusively in this zone.

First, the formula used in Chaboche's law of Lagamine model, which models the changes in material properties due to temperature, will be shown again:

$$P(T [^{\circ}\text{C}]) = A_p \left(1 - B_p \cdot \exp\left(\frac{T [^{\circ}\text{C}]}{C_p}\right) \right) \quad (4.2)$$

Then, Figure 4.2 shows a part of the lag.file used in the Lagamine model where the Chaboche's law is introduced, with the respective parameters for Haynes 230 alloy.

COLAW							
Chaboche Model			Haynes230 with corrosion				
1	271			1	23	2	
1	1	50	3	0	0		
0.5	0.00001						
800.0	2000.0	0.20					
0.8	0.5	50.0					
197000.0	0.01	300.0		1.0	1.0	1.0	1.0
1.24e-5	-0.01	250.0		0.3	0.0	100.0	
0.01	0.0	100.0		50.0	-4.0	-300.0	
15.0	55.0			2.0	0.0	100.0	
3.57e-2	1765.72	1.28e-3		158.93	-4.0	19.0	
790902.0	10867.0	3.0E-22		2.1			
370309.0	8381.0	1.4E-22		2.1			
47339.0	500.0	1.0E-22		2.1			
10.0	0.0	100.0		2.0	2.0	0.1	400.0
0.91713	-7.147	-471.58		2.2186			
190000.0	-75.0	3.5		4.0			
1.50e-12	0.0	10.0					

Figure 4.2: Parameters of the Chaboche's law for Haynes 230. Extract of the input file of the Lagamine model

The encircled values are those used to calculate the properties used in the diffusional model. In red are encircled the constants relating to the Young's modulus, in green to the Poisson's ratio and in blue to the elastic limit. These values are shown in summary form below:

Constants	A_p	B_p	C_p
E	197.000	0,01	300
ν	0,3	0	100
σ_y	50	-4	-300

Table 4-1: Constant to calculate material parameters at 700°C

Then, using these constants, the properties of Haynes 230 at 700°C are obtained:

$$\begin{cases} E(700^\circ\text{C}) = 176.684,85 \text{ MPa} \\ \nu(700^\circ\text{C}) = 0,3 \\ \sigma_y(700^\circ\text{C}) = 69,39 \text{ MPa} \end{cases} \quad (4.3)$$

4.1.3 Load

Considering that in a CSP plant, the working loading is cyclic due to the periods of sunlight and non-sunlight, ideally it would be best to perform this test with a cyclic load, or by varying the temperature cyclically. However, due to the limitations of the diffusional elastic model, this is currently not possible as the temperature affects the material properties, which are uniquely introduced in Julien's model, and the load can only be set to a constant value throughout the simulation or to a progressive load.

As mentioned before, during this work it has been necessary to adapt to the limitations of the model since introducing the possibility of a cyclic load would have implied not only a modification of the code but also of the model itself, by introducing time-dependent stiffness matrices.

For this reason, in this case, a test is carried out by progressively applying the load over time. This option is chosen as it is one of the only two viable options in the diffusional elastic model and by applying it progressively, the stress-strain curve can be easily obtained with which to mechanically compare both models.



Figure 4.3: Application of surface pressure at the end of the beam

Taking also into account that the calculated yield stress for Haynes 230 alloy at 700°C is around 69 MPa, a load lower than this has to be applied to ensure that the material is always working in the elastic zone. Therefore, the load will be a surface pressure at the end of the beam, Figure 4.3, applied progressively until it reaches 60 MPa at the end of the test, as shown in Figure 4.4.

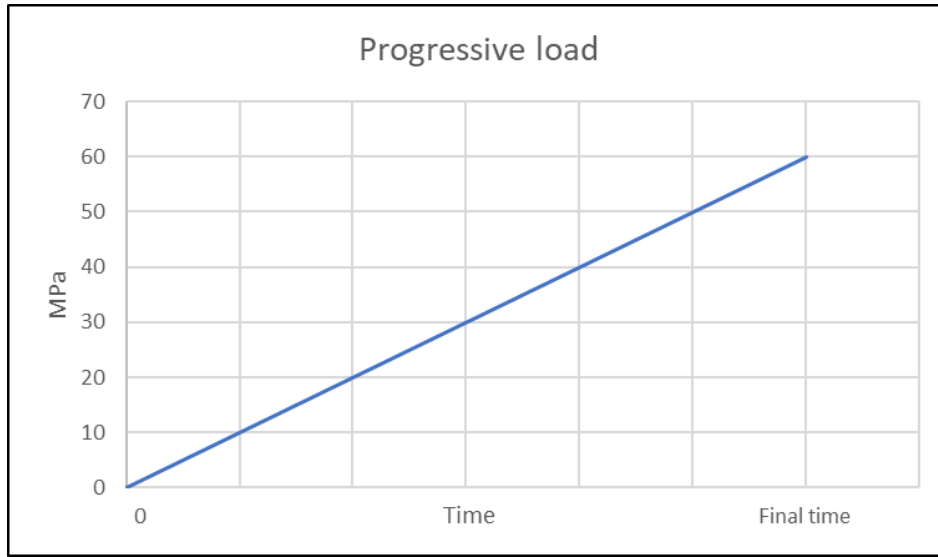


Figure 4.4: Time evolution of the load applied

4.1.4 Meshes

Both models use the finite element method, so a mesh with the dimensions of the beam to be studied has to be used to obtain the stresses, deformations and displacements along the beam.

For the diffusional elastic model, the mesh shown in Figure 4.5 is used, which is composed of 256 elements (16x16).

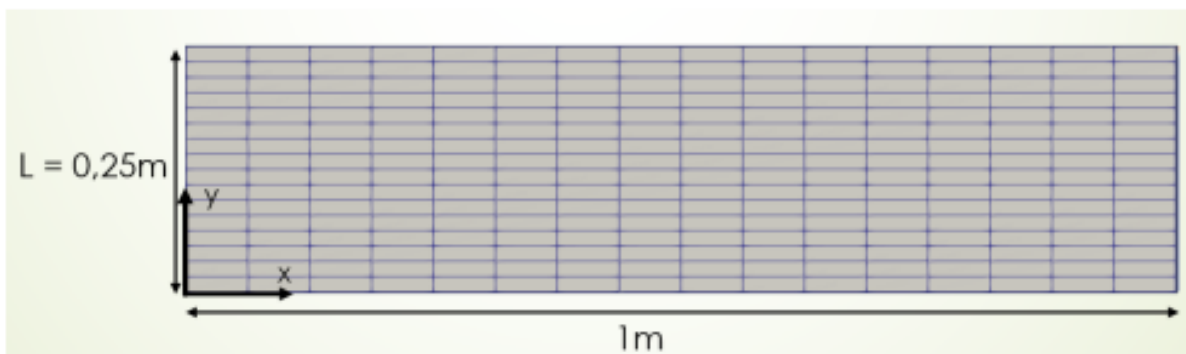


Figure 4.5: Mesh used in the diffusional elastic model

In the case of the Lagamine model, a regular mesh composed of 40 elements is used, that is, 4 rows of 10 elements each, (4x10), Figure 4.6.

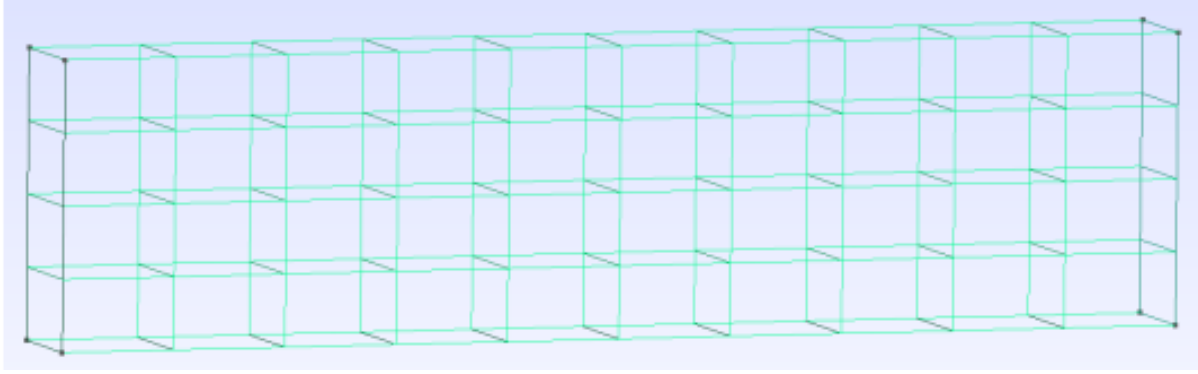


Figure 4.6: Mesh used in the Lagamine model

At first look, the difference between one mesh and the other can be seen, since the diffusional model has a finer mesh, with many more elements being the same dimensions of the beam. Figure 4.7 shows a comparison of both meshes, showing the mesh elements of the Lagamine model and the nodes of the mesh of the diffusional model. In the case of this second model, the nodes are represented in the figure, as it should be noted that the results are shown as a function of them, even for the stresses.

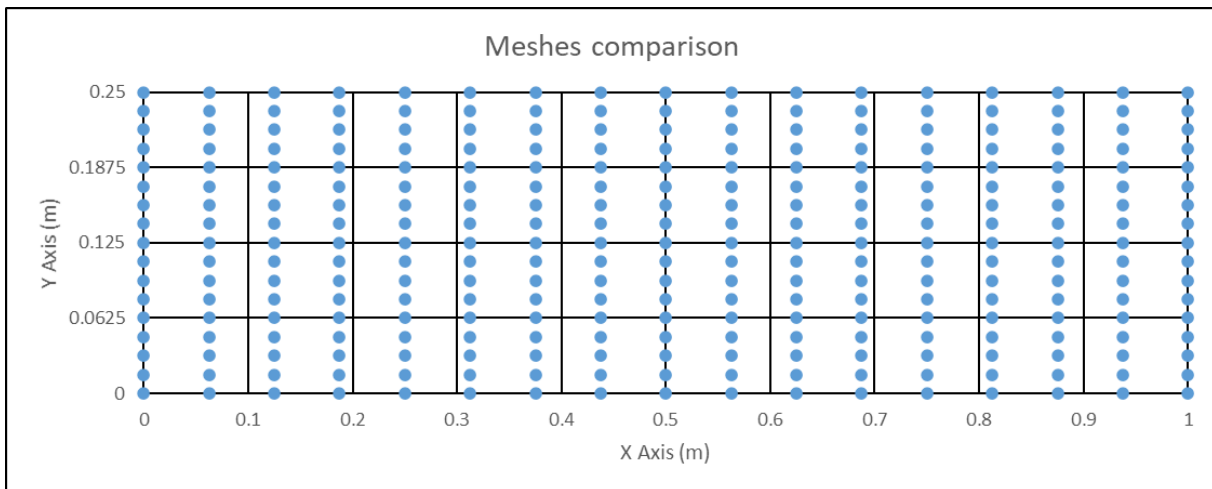


Figure 4.7: Meshes comparison; Elements borders of the Lagamine model (Black lines); Nodes of the diffusional model (Blue points)

This clear difference between the two meshes is explained by the greater need for precision in one model than in the other. Since it is a mechanically uniform loading in a tensile test, it is easy to calculate the stresses and strains in the beam, so that mechanically not much precision is needed.

Therefore, the Lagamine model has fewer elements due to the simplicity of the mechanical calculation and the fact that the corrosion component is taken into account with a damage law that affects all the elements, designated as affected by the corrosion, equally.

On the other hand, since the diffusional elastic model deals with the corrosion from a diffusional approach, the corrosive concentration is treated as a degree of freedom of the model, so a higher accuracy, and therefore, a higher number of elements in the mesh is needed to model this diffusion in an optimal way.

4.1.5 Corrosion

To complete the description of the boundary conditions of this test, the aim is to model the described tensile test by adding corrosion on the top face of the material. This seeks to simulate the corrosion to which the inner face of the material is exposed in the pipes of a CSP plant due to the contact with hot molten salt.

By applying this corrosion on the upper part of the beam, it is intended to study the evolution of the material degradation as well as the variation of the mechanical behaviour of the beam while the progressive load is applied at the end of the beam.

The diagram showing the boundary conditions of this tensile test will then have the form shown in figure 5.

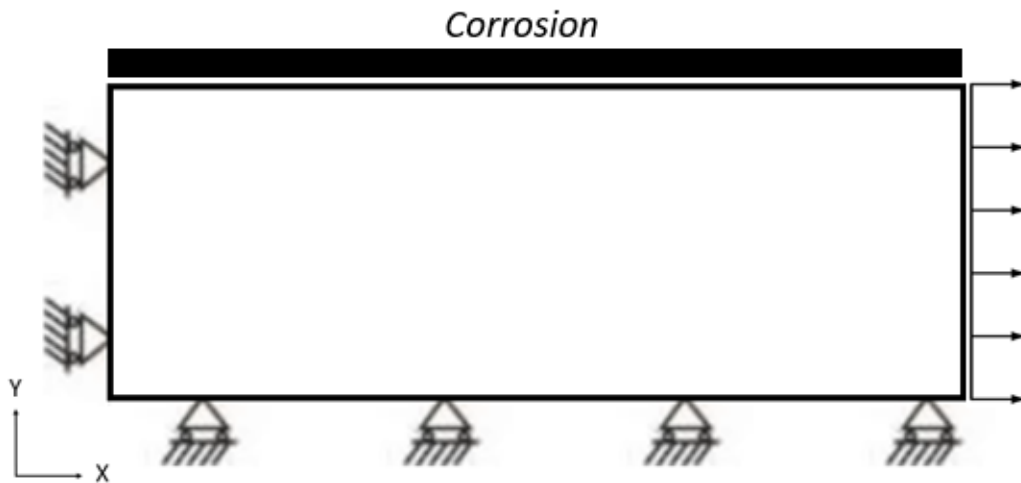


Figure 4.8: Diagram of the boundary conditions of the test

In the Lagamine model, corrosion does not propagate from one element to another due to its corrosion damage approach. Therefore, to reproduce the test desired and model a beam under top corrosion, the material law with corrosion is applied to the elements bordering the top surface. In Figure 4.9, the top row of elements of the Lagamine mesh are represented in light purple (elements for which corrosion damage is taken into account) and then, the surface exposed to corrosion is in orange.

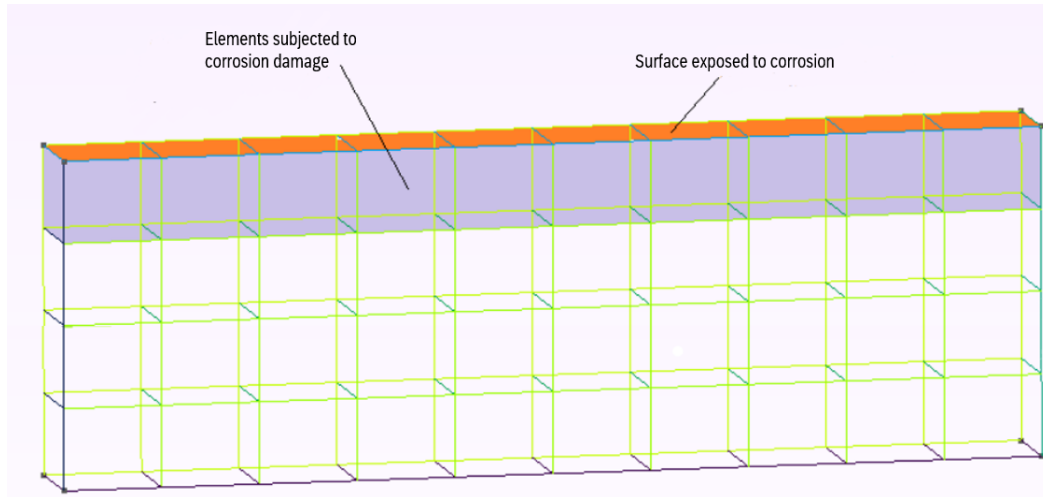


Figure 4.9: Lagamine mesh, applying top corrosion

Taking this into account, in the diffusional model an initial corrosion concentration of 100% will be applied at the nodes on the top surface of the beam, in order to model the diffusion of the corrosion. To have the same conditions in both models, the simulation time will be at which the diffusional model has $\frac{1}{4}$ of his mesh affected by corrosion, since as explained, in the Lagamine model it is used a mesh with $\frac{1}{4}$ of it subjected to corrosion. The limit that has been chosen to determine when the material is being affected by corrosion or not, is the 1% decrease of the Young's modulus.

To know the exact time of the test simulation, the diffusional model will be used to determine it and when the nodes at $\frac{3}{4}$ height of the mesh have a degradation of 1%, this time will be used to make the comparison.

Regarding the values of the corrosion parameters, since the diffusional model is the one that best models the corrosion phenomenon, literature data has been used for this model and the aim is to obtain similar results by adjusting the corrosion variables of the Lagamine model.

Looking back to the literature review chapter, it can be found experimental tables with the corrosion variables (D & M) used by the diffusional model for nickel-based alloys at the target temperature of this study (700°C), Figure 4.10.

$T (^{\circ}\text{C})$	$D (\text{mm}^2/\text{s})$	$T (^{\circ}\text{C})$	$M (\text{MPa}^{-1})$
650	$1.085\text{e} - 13$	650	0.001585
700	$1.397\text{e} - 12$	700	0.0098
750	$5.859\text{e} - 12$	750	0.068
800	$1.423\text{e} - 11$	800	0.188

Figure 4.10: Literature data of the corrosion parameters of the diffusional model

Before concluding this section, a comparison of the damage laws used by each model is made. First, the damage law equation of the Lagamine model:

$$E = (1 - D_u)E_0 \quad (4.4)$$

On the other hand, the damage law of the diffusional model is governed by the following equation:

$$E = \left(1 + \phi[\%] \left(\frac{E_d}{E_0} - 1\right)\right) E_0 \quad (4.5)$$

If this expression is operated:

$$E = E_0 + \phi \cdot E_d - \phi \cdot E_0 \quad (4.6)$$

And then, simplified:

$$E = (1 - \phi)E_0 + \phi \cdot E_d \quad (4.7)$$

However, if E_d is cancelled, it is obtained an expression equivalent to the damage law of the Lagamine model (4.4):

$$E = (1 - \phi)E_0 \quad (4.8)$$

This means that in order to have the same damage law, so that both damage variables modify the Young's modulus in the same way, the value of E_d must be introduced in the diffusional model as zero. This means that when the material is 100% corroded, its Young's modulus is equal to 0.

Thanks to this modification in the damage law of the diffusional model, apart from having the same damage law, it is observed that the damage variables are equivalent (ϕ and D_u), so they can be used directly to make the corrosion comparison between the models. In addition, by

setting the initial concentration in the diffusional model as 100% in the top surface and being within the range of [0%,100%], the corrosive concentration is equal to the damage variable ϕ , so the comparison of models can be made using c (degree of freedom of diffusional model) and D_u (damage variable of Lagamine model).

4.2 Comparison without corrosion

Before carrying out the test by applying the corrosive boundary conditions to each model, it is first necessary to check that both models are mechanically compatible. For this purpose, the same tensile test described above will be carried out but without applying the corrosion.

As this is a simple tensile test, in which the beam is subjected to a homogeneous mechanical load and there is no deterioration of the material due to corrosion, the whole beam is subjected to the same stresses and deformations. Because of this it is easy to make a comparison between models, since all the elements of the Lagamine model have the same results and all the nodes of the diffusional elastic model have the same results.

First, the simulation is carried out in the diffusional elastic model. In order to make the comparison with the other model, the stress-strain curve of any node of the mesh is obtained in order to compare it with the stress-strain curve that will later be obtained from the Lagamine model. The result of this test is shown in Figure 4.11:

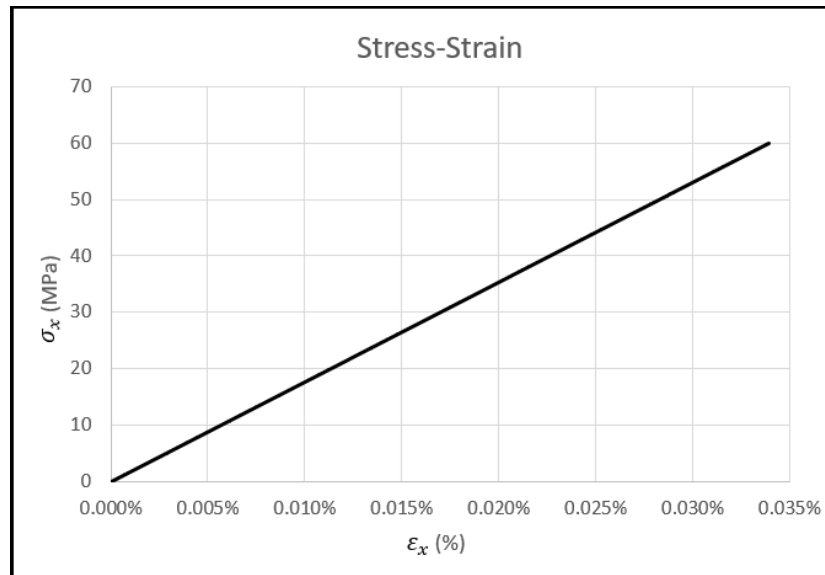


Figure 4.11: Stress-strain curve; No corrosion; Diffusional model

As expected, the stress-strain curve of the diffusional model has the usual shape of the elastic zone. In this case, the simulation time is irrelevant, as the result will be the same regardless of the loading rate. In this model, the time only influences the corrosion, since the longer the time, the higher the degree of deterioration of the beam due to corrosion damage.

Then, the same process is performed but with the Lagamine model, obtaining the following stress-strain curve, Figure 4.12:

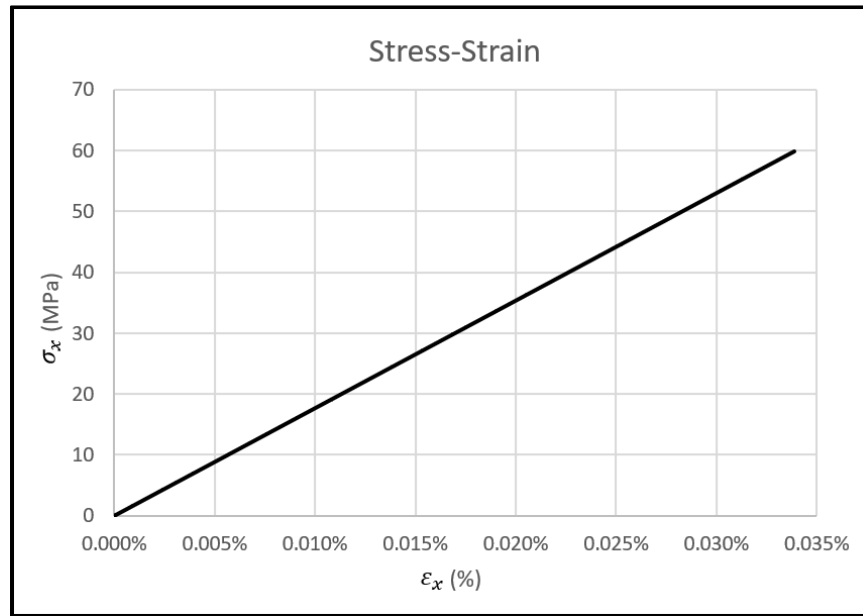


Figure 4.12: Stress-strain curve; No corrosion; Lagamine model

In this case, it can also be seen that work is carried out in the elastic zone. This model is also not influenced by the simulation time or the loading speed for this test without corrosion, since on the one hand, there is no corrosion damage that could increase with time and on the other hand, when working in the elastic zone, there is no effect of visco-plasticity due to the speed of the load.

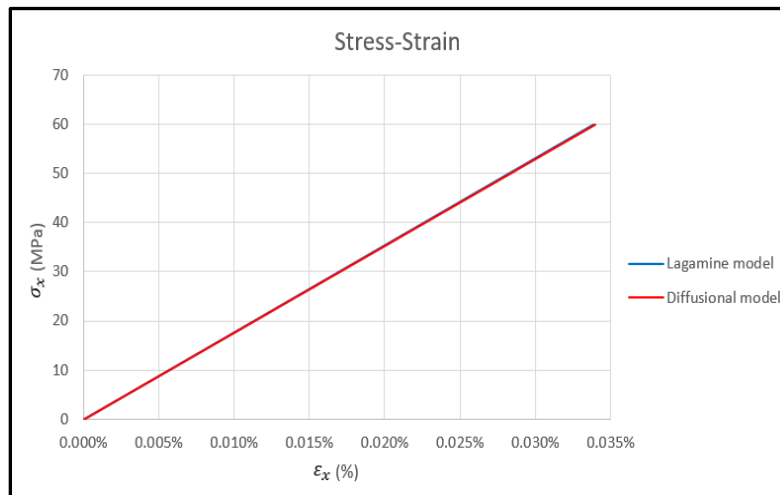


Figure 4.13: Mechanical comparison without corrosion

Both models seem to obtain very similar results, however, in order to better appreciate this similarity, the stress-strain curves of both models are joined in Figure 4.13. In this figure it can be seen how both models give practically identical results, so it can be concluded that they are perfectly compatible from the mechanical point of view, given the conditions described for this tensile test, and as long as work is carried out in the elastic zone.

Once this mechanical compatibility is assured, in the following section, the comparison is carried out by applying corrosion to both models. In this case, although there is still a uniform mechanical load, the comparison will not be so simple, since the application of corrosion from the upper surface of the beam leads to a deterioration of the material in this area, which causes alterations in the stresses and deformations experienced by the beam.

4.3 Comparison with corrosion

In this section, the comparison of models applying corrosion with the boundary conditions described in the previous sections will be carried out. For this purpose, the diffusional model is used with the values of its corrosion variables (M and D) obtained from experimental results in the literature (Table 4-2).

$M(MPa^{-1})$	$D(mm^2/s)$
0,0098	1,397e-12

Table 4-2: Corrosion variables used in the diffusional model

Since the Lagamine model uses the corrosion damage law for $\frac{1}{4}$ of the beam, the first step in the comparison is to determine the time required for corrosion to evolve in the diffusional model until $\frac{1}{4}$ of the beam is affected.

4.3.1 Determination of the time simulation

In order to determine the simulation time required for $\frac{1}{4}$ of the beam to be affected by corrosion, the nodes of the mesh that are located at $\frac{3}{4}$ of the total height of the beam, figure 5, must be studied. These nodes will be considered as affected by corrosion when their Young's modulus is decreased by 1%.

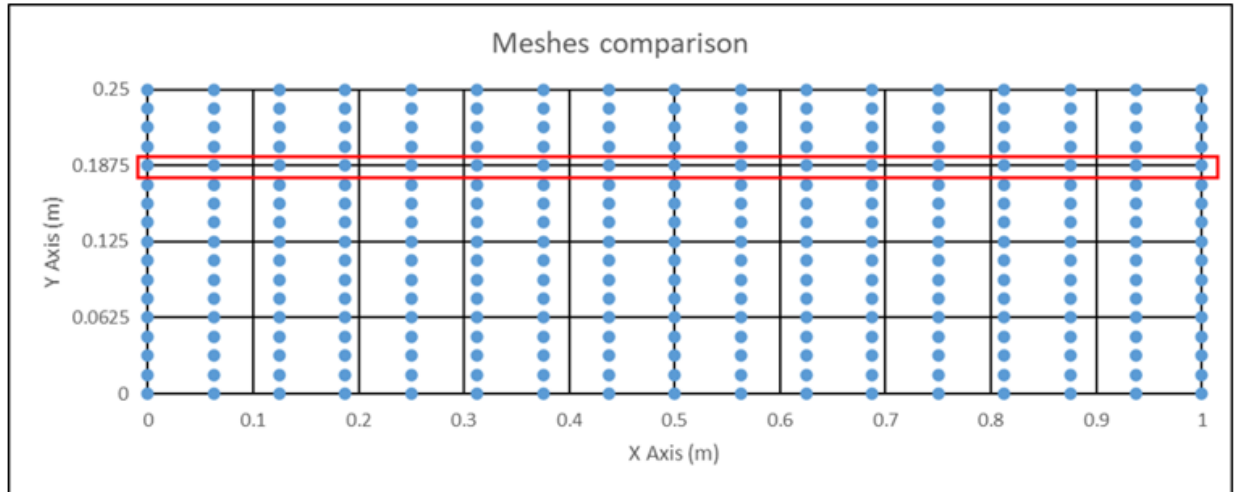


Figure 4.14: Nodes studied to determine the time simulation

Instead of studying the Young's modulus of the nodes marked in red, one can look directly at their damage variable, i.e. the corrosive concentration in these nodes. Based on the damage law of this model (4.8), it is known that a decrease in the Young's modulus of 1% is equivalent to the damage variable also being equal to 1%.

Then, a 10-year simulation (Figure 4.15) is carried out to observe the evolution of the corrosion concentration at these selected nodes and to obtain a first approximation of when the desired time is reached.

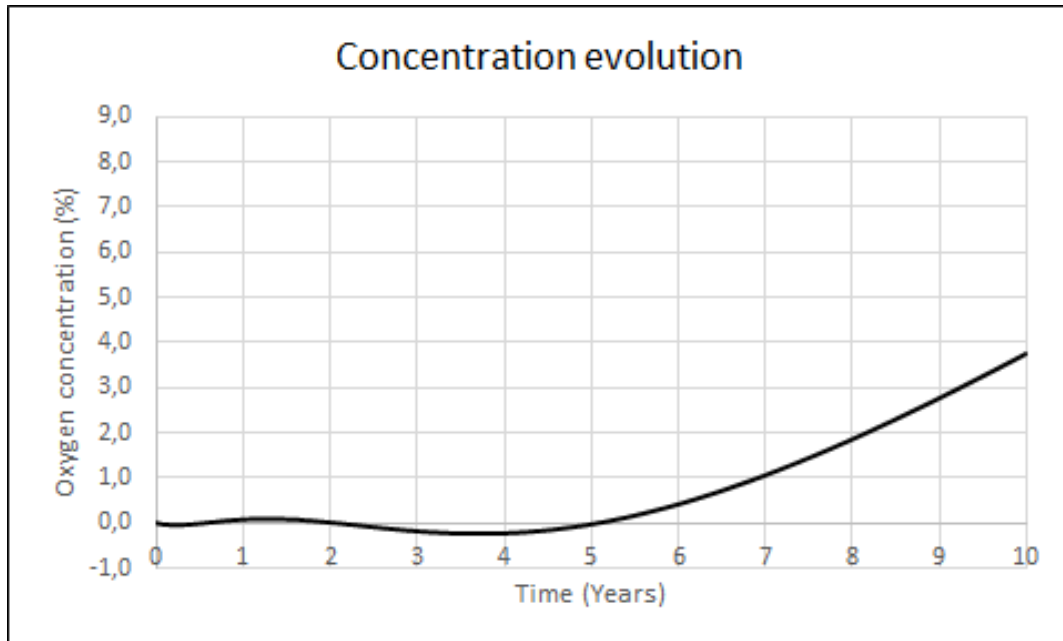


Figure 4.15: Concentration evolution of the nodes located at $\frac{3}{4}$ of the height of the beam

This simulation serves to know around what time the $\frac{1}{4}$ corrosion of the beam is going to be reached and observing the graph, it can be concluded that this moment is reached around year 7. However, this first approximation needs to be refined with more simulations of a duration around this time to get the exact value for a simple reason.

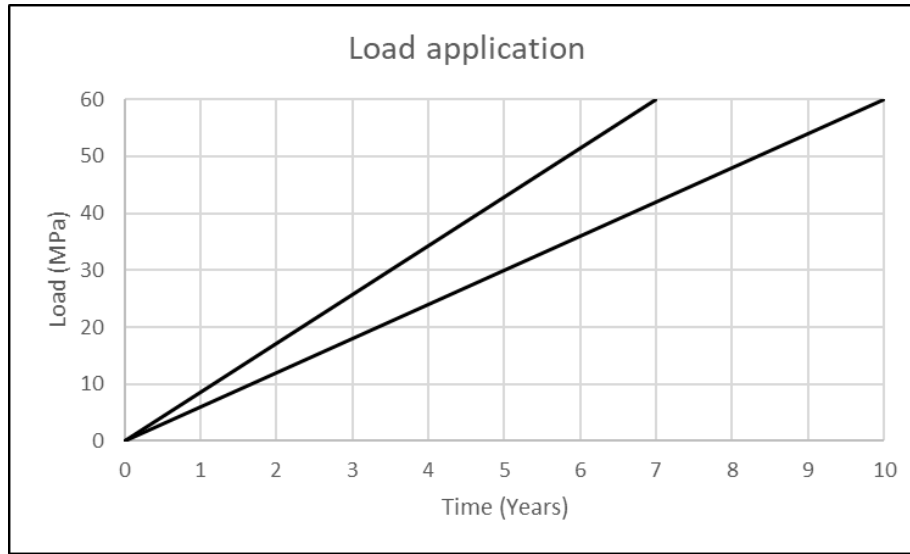


Figure 4.16: Difference between a 10-year load vs a 7-year load

Firstly, it is known that the load has an effect on the diffusion through the pressure factor (M) in equation (3.8), therefore, as this test uses a progressive load that reaches its maximum value at the end of the simulation, by varying the time of the simulation there may be certain changes in the evolution of the concentration, since the value of the load applied is different in the first years, as shown in Figure 4.16.

Then, taking into account this influence of the load, by performing several simulations over a period of about 7 years, it is finally concluded that the time necessary for the $\frac{1}{4}$ of the beam to be affected by corrosion is 6,8 years. Additionally, it should be mentioned the appearance of oscillations in the corrosive concentration in the first years of simulation in Figure 4.15. This phenomenon will be explained and studied in the following sections.

4.3.2 First corrosion comparison

To achieve the coupling of results between models, the literature values for the diffusional model are used and the corrosion variable of the Lagamine model is varied until the maximum possible similarity is achieved. For this purpose, the results of an element of the Lagamine model and the equivalent node in the diffusional model, located exactly in the centre of the Lagamine element, will be compared, as shown in Figure 4.17.

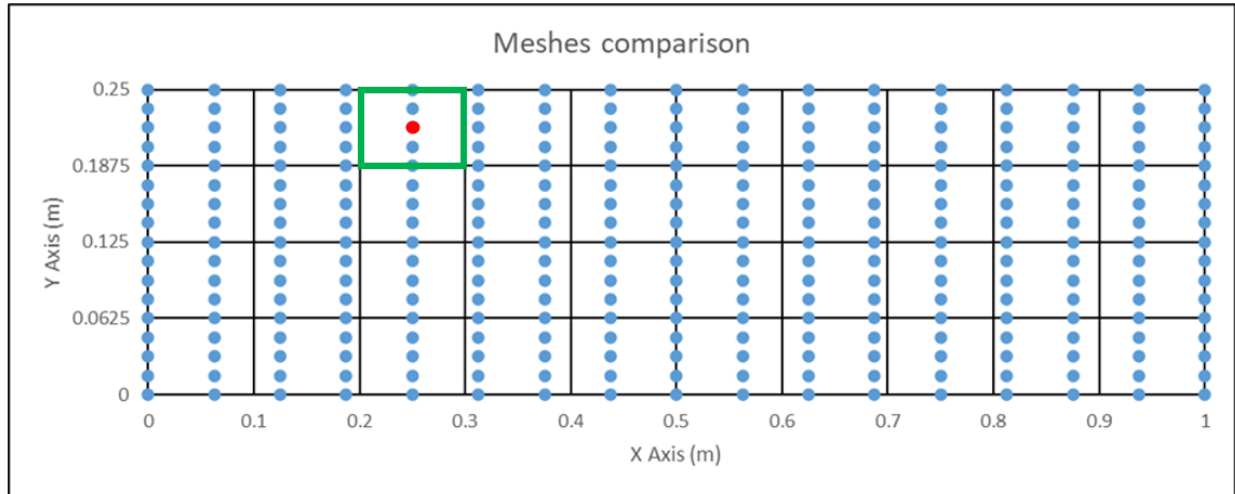


Figure 4.17: Element studied in Lagamine model (Green); Node studied in diffusional elastic model (Red)

Performing the 6,8-year simulation, it is found that the most similar results between models are achieved by introducing the following corrosion ratio in the Lagamine model ($k_u = 9 \cdot 10^{-13} \text{ m/s}$). Using the results of the stresses and strains of both models, the Young's moduli are calculated in both cases and their time evolution is compared, Figure 4.18. In this graph, despite using the best possible value in the Lagamine model, the results are quite far from each other since they have different curve shapes.

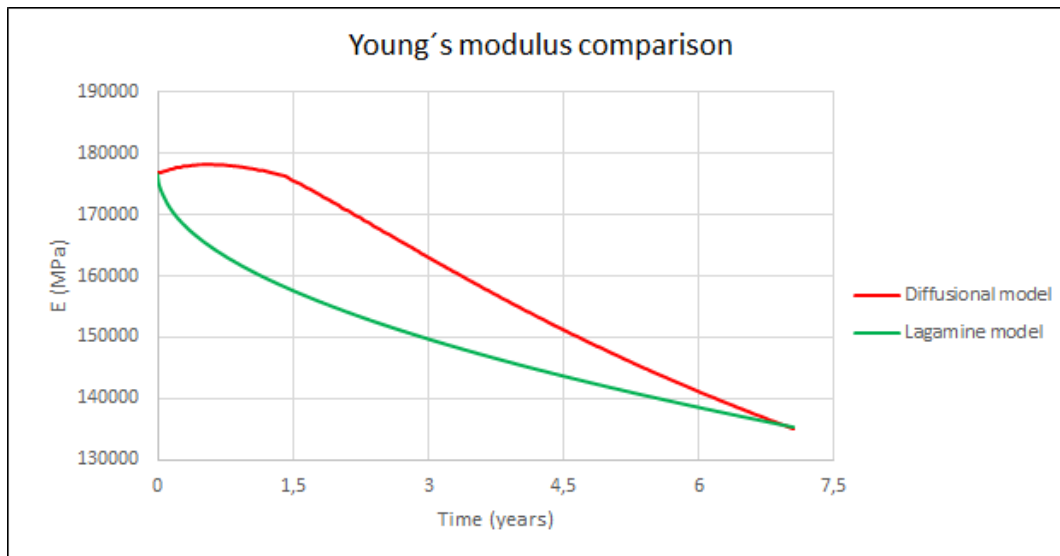


Figure 4.18: Young modulus comparison

This clear difference between models is due to an increase of the Young's modulus in the diffusional model during the first years of the simulation. From a physical point of view, it does

not make sense that a material with some damage due to corrosion has a higher Young's modulus than the undamaged material. So, in order to find a reason for this hardening, a comparison of the damage variables of both models is carried out for the same situation.

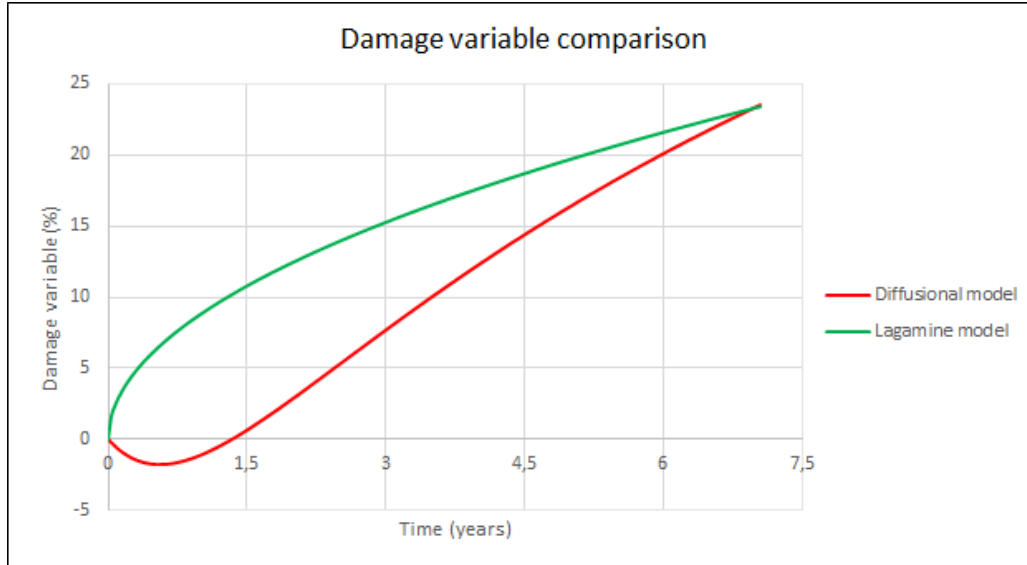


Figure 4.19: Damage variable comparison

In the comparison of the corrosion variables in Figure 4.19, it is shown how the diffusional model has negative and oscillating values at the beginning of the simulation. This negative damage is impossible to occur in reality and is a malfunction that leads to a fictitious hardening of the material. Therefore, in order to be able to continue with the model comparison, this phenomenon must be studied to understand why it occurs and to be able to correct it. These oscillations already appeared in Figure 4.15, although to a smaller scale.

4.3.3 Study of the negative oscillations

The occurrence of negative oscillations in the damage variable of the diffusional model is studied by modifying several factors that can affect the quality of the simulation. Firstly, the effect of the simulation time step on this phenomenon is studied. As the simulation time is several years, a too large time step could cause bad approximations or inconsistencies in the simulation.

For this purpose, the damage variable of the diffusional model is studied at the same node of the mesh as in the previous case. This time, a simulation of 10 years duration is performed, and the number of time steps is varied in order to observe how the phenomenon of oscillations and the quality of the simulation behaves. It should be mentioned that currently the simulation has been carried out by using 200 time steps.

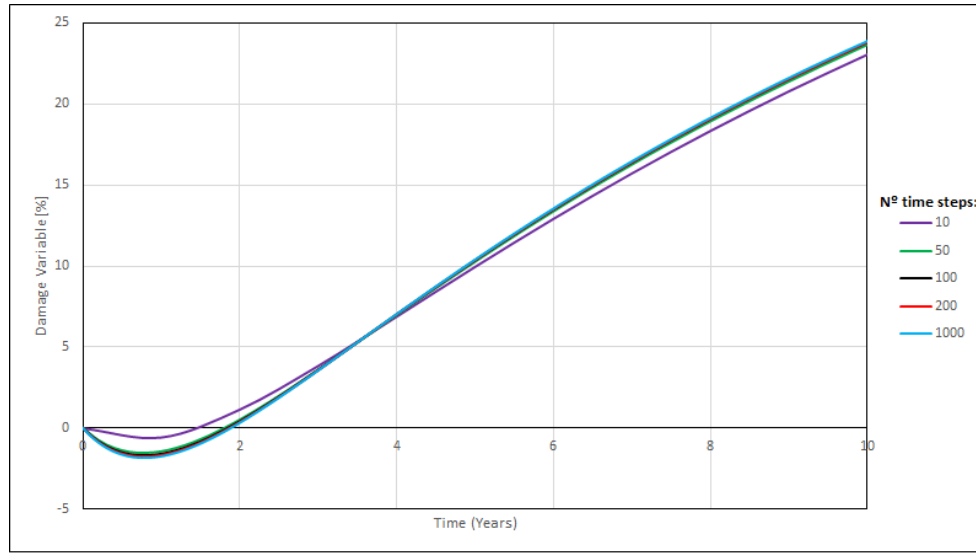


Figure 4.20: Study of oscillations based on time step

Looking at figure 4.20, it can be seen that all cases give very similar results with the exception of the 10 time steps simulation since, evidently, this time step is too imprecise for a total duration of 10 years, and it is normal that the results differ with respect to the rest. Roughly speaking, the number of time steps does not have a significant influence as the other cases give a practically identical curve shape.

However, in order to study the influence of the time step on the oscillations, the same results are shown but zooming in on the area of interest, at the beginning of the simulation, where the negative values occur, Figure 4.21.

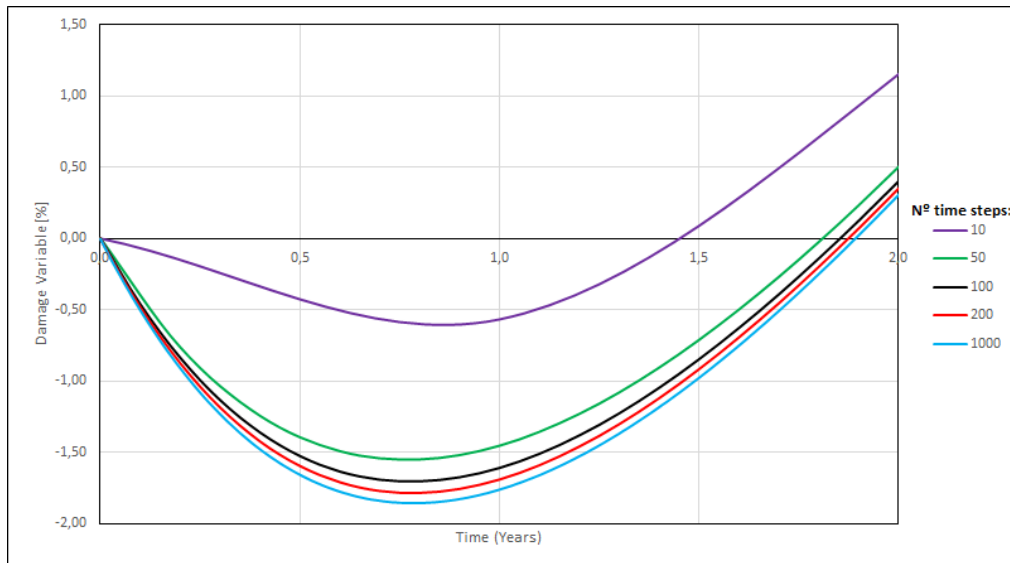


Figure 4.21: Study of oscillations based on time step (Zoom in)

When zooming in on the results, it can be seen that as the number of time steps increases, far from solving the problem, the damage variable reaches even more negative values, showing a trend towards -2% as the number of time steps increases. Therefore, it is concluded that a higher precision in the time step is not the solution for this problem, as increasing it makes the problem even worse.

The next factor to be studied is the coefficient of diffusivity (D). This is one of the two corrosion variables used in the diffusional model and is the dominant factor controlling the rate at which corrosion diffuses through the beam.

In the development of the diffusional model during the master thesis of Julien Heremans, no negative corrosive concentrations were detected at any time. However, Julien during his work did not use literature values whose magnitude is around ($\sim 10^{-12}$; 10^{-13}) but he used significantly higher coefficients of diffusivity ($\sim 10^{-1}$; 10^{-2}) for his tests, as his simulations were not as long as in this work. It would therefore be interesting to study the influence of this factor on the problem of negative oscillations.

Simulations are then carried out by studying the same node as previously, using 200 time steps and varying the coefficient of diffusivity, Figure 4.22.

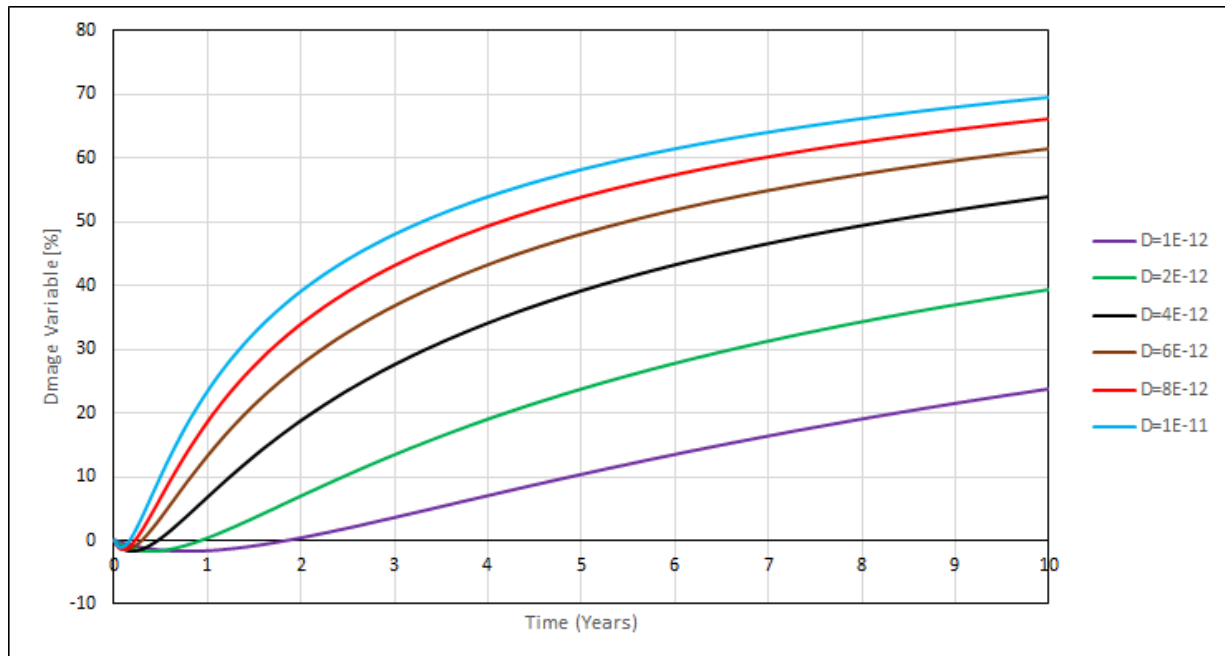


Figure 4.22: Study of oscillations based on coefficient of diffusivity

It can be seen that the higher the coefficient of diffusivity, the higher the corrosion damage throughout the simulation, as expected. In relation to the oscillations, it can also be observed that the higher the coefficient of diffusivity, the shorter the time it takes for the damage variable

to enter positive values, since the case with the lowest diffusion ends the oscillation around year two and the case with the highest diffusion in the first part of the first year.

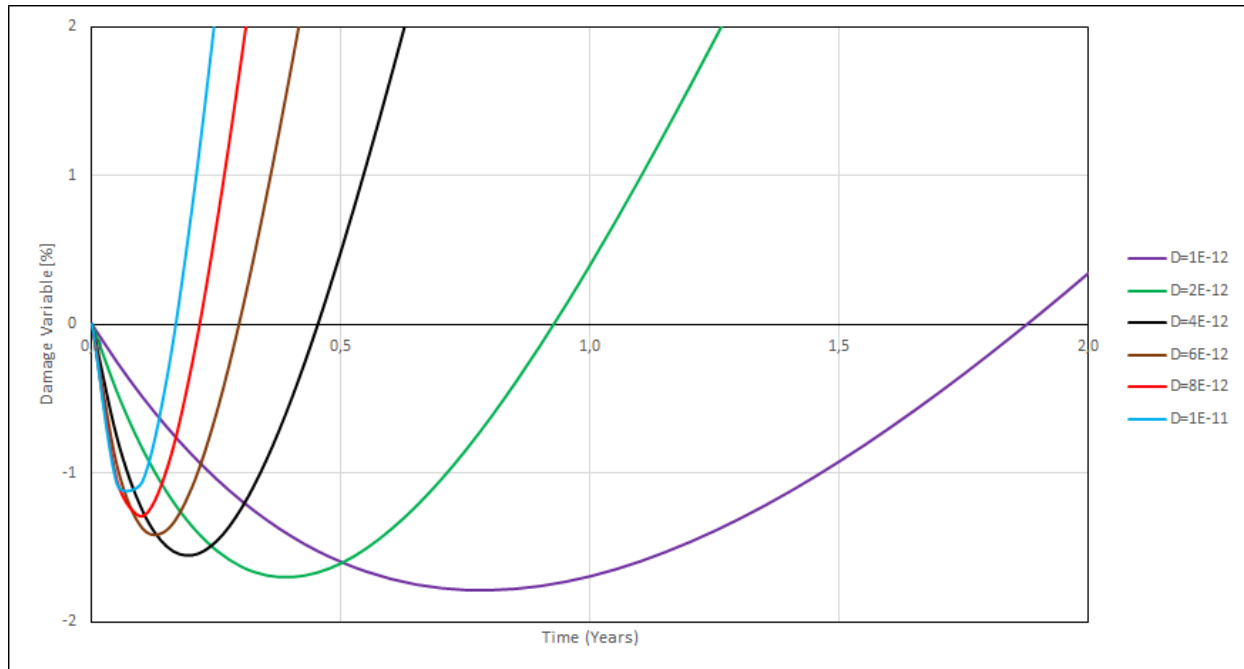


Figure 4.23: Study of oscillations based on coefficient of diffusivity (Zoom in)

Figure 4.23 shows a zoom in on the oscillation area to better appreciate not only the duration of the oscillation but also its amplitude. It can be concluded a priori that the higher the diffusion coefficient, the shorter the oscillation and the smaller the amplitude.

However, previously, by studying the influence of time step on the oscillations, it has been shown that greater time precision leads to greater amplitude. It would therefore be interesting to combine both effects (time step and diffusion coefficient) in order to observe the changes that occur.

In order to study the combination of these two factors, it was decided to study the case with the highest diffusion coefficient, carrying out two different simulations, one with 200 time steps and the other with 1000 time steps. Viewing the comparison of the two simulations, Figure 4.24, it can again be seen that the variation of time steps does not affect the overall quality of the simulation as both cases show almost identical results. However, there is a slight difference in the area of the oscillation.

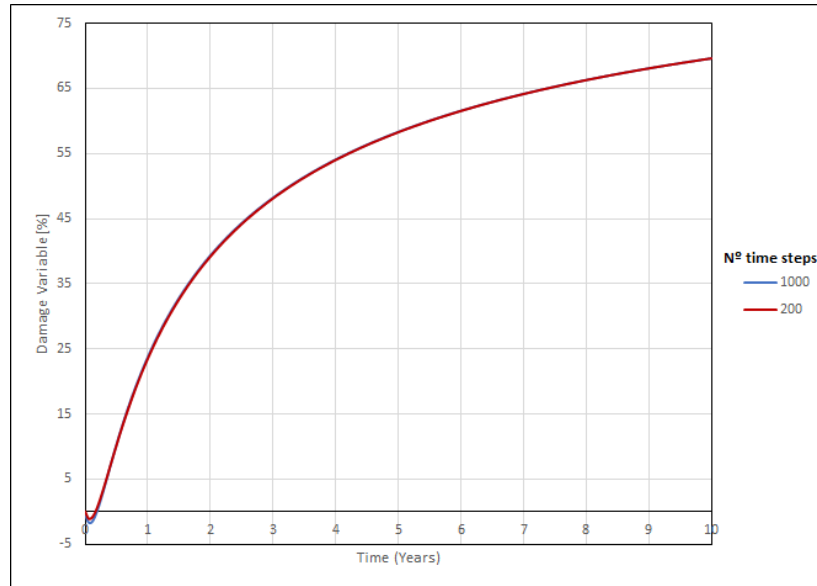


Figure 4.24: Study of oscillations with higher diffusivity based on time step

By zooming in again in the oscillatory zone, Figure 4.25, it is shown that by increasing the diffusion coefficient the problem does not disappear, simply, as the process takes place faster, precision is lost and the oscillation seems smaller, therefore, if precision is gained by decreasing the size of the time step, it can be seen that the oscillation returns to similar values of previous cases, so it is concluded that increasing the diffusion coefficient will not solve this problem.

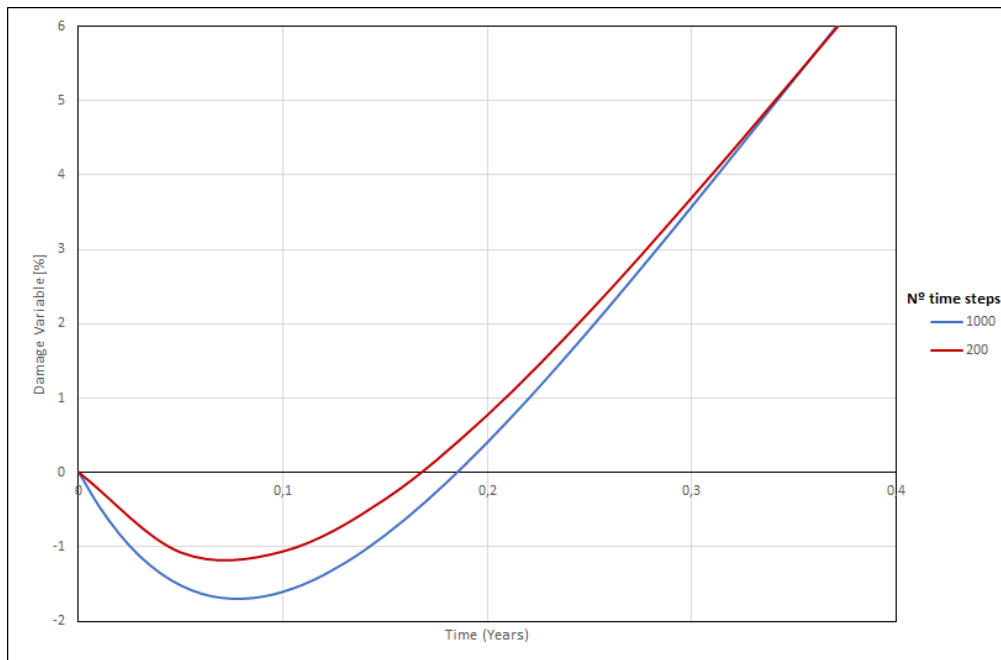


Figure 4.25: Study of oscillation with high diffusivity based on time step (Zoom in)

Taking into account that neither of the two previous factors have served as a solution to the problem of negative oscillations, it is now decided to study the mesh of the model. So, to achieve greater precision by modifying the mesh, the number of mesh elements must be increased to make the mesh finer. In order to study the influence of the mesh on the oscillations, three different meshes are used, as described in Table 4-3.

Mesh	N° of total elements	N° of elements in Y axis	N° of elements in X axis
1	256	16	16
2	532	14	38
3	1404	18	78

Table 4-3: Meshes used to study the oscillations

The first mesh is the one that has been used throughout the work, the second mesh has more elements in total but less on the Y-axis and the last mesh has by far the most elements. With these meshes, the aim is not only to study the influence of the total number of elements but also of the number of elements on each axis.

To carry out this study, a 10-year simulation is performed with the original corrosion parameters and 200 time steps, however, this time it is studied in a node of the mesh that is further away from the corrosion zone, so that there is practically no diffusion and only the phenomenon of negative oscillations can be observed.

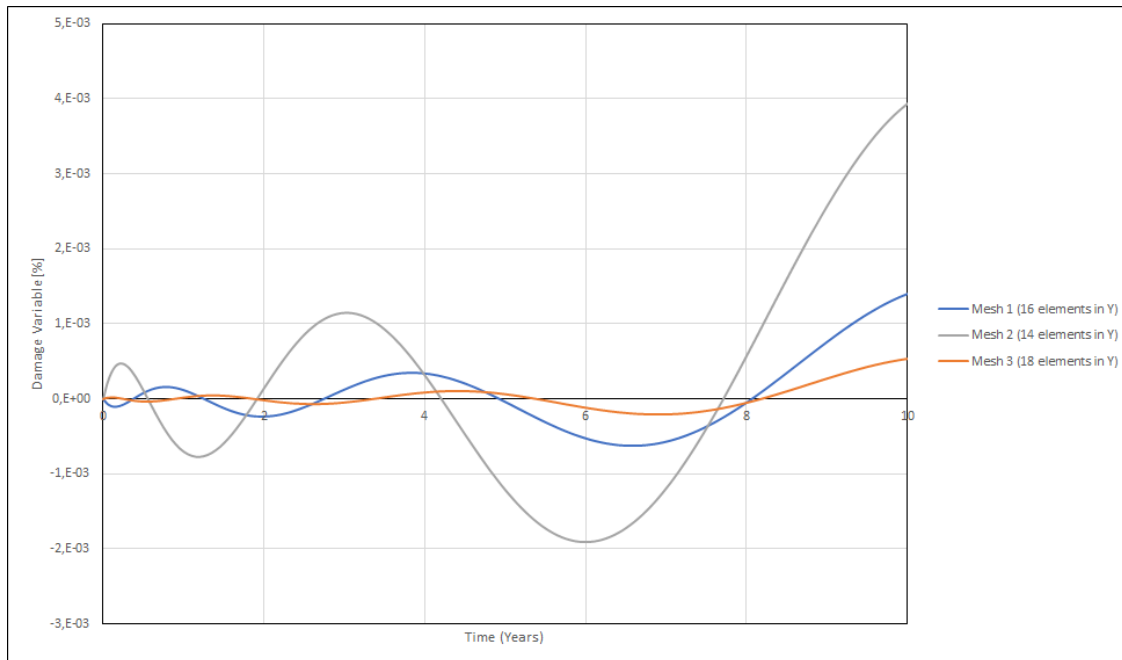


Figure 4.26: Study of oscillation based on mesh (Outside the corrosion zone)

Figure 4.26 shows the results for the 3 meshes, it can be seen at first view that being outside the corrosion zone, the damage values are much lower but still have the oscillatory character. Comparing the 3 meshes, it can be seen that Mesh 3 has the lowest oscillation, however, Mesh 2, despite having a higher total number of elements than Mesh 1, has a higher oscillation. On the other hand, if we compare the results of Mesh 1 and Mesh 3, the results of Mesh 3 only slightly improve despite having much more elements compared to Mesh 1.

In conclusion, a higher precision in the mesh does serve to solve or at least lessen the problem of negative oscillations. However, this improvement is not obtained simply by adding more elements to the mesh. As this is a case where the corrosion is applied over the entire upper surface, the diffusion is produced on the Y-axis, therefore, in order to obtain greater precision, it is not so important the total number of elements but the number of elements in the direction of the Y-axis. Because of this Mesh 1 gives better results than Mesh 2 and only slightly worse results than Mesh 3 despite having significantly fewer elements, as the difference in the Y-axis is not so great.

To validate this idea, a final comparison is made between Meshes 2 and 3, since they differ the most in the number of elements in the Y-axis, but this time studying a node in the corrosion zone. The aim is to observe if the reduction of oscillations also occurs in the corrosive diffusion zone when increasing the number of elements in the Y-axis.

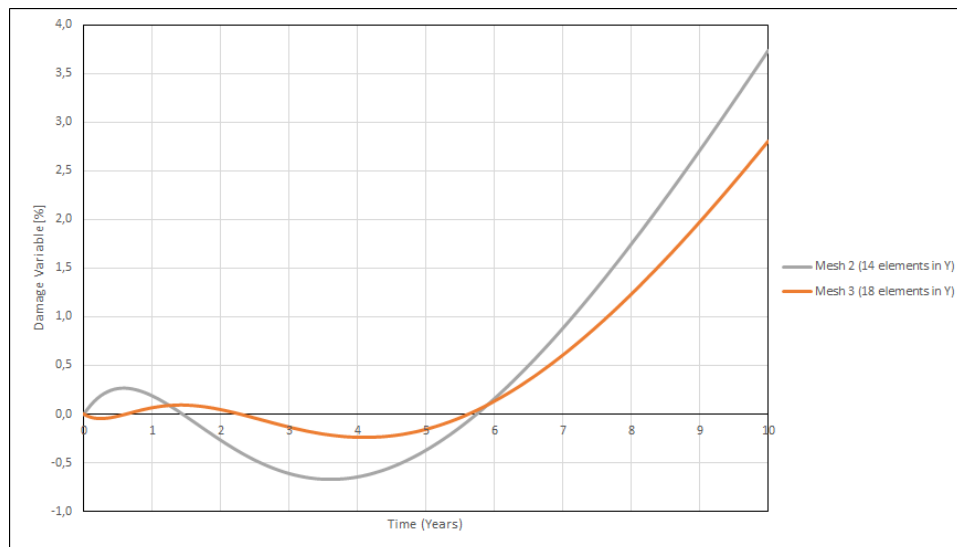


Figure 4.27: Study of oscillations based on mesh (In the corrosion zone)

Reviewing the results shown in Figure 4.27, it can be finally concluded that increasing the number of elements in the same axis where corrosion occurs can solve or at least reduce the problem of negative oscillations. Because of this, in order to continue with the comparison between the two corrosion models, the mesh of the diffusional elastic model has to be modified to improve its accuracy as far as the Y-axis is concerned.

4.3.4 Mesh modification

To improve the quality of the mesh there are two viable options. The first option consists of creating a new mesh with a higher number of elements on the Y axis and the same number on the X axis, while the second option consists of modifying the current mesh, concentrating the Y axis elements in the upper area of the beam, thereby increasing the density of elements in that area and increasing the accuracy where the corrosion matters.

In this work, the second option has been chosen for several reasons: the creation of a new mesh entails the use of mesh generating software and with it a learning period, and on the other hand, by adding more elements, the computational cost of the simulations increases. In addition, as this is a simple test at the mechanical level, not much precision is needed for the part of the mesh that is not affected by corrosion, so by concentrating the elements in the upper part, the quality of the simulation is not compromised.

Then, to continue with the comparison between the Lagamine model and the diffusional model, the mesh of the diffusional model is modified, concentrating most of the elements in the upper half of the beam, Figure 4.28. In order to compare the results of both meshes, it will be used the results of the node that was originally studied in the model comparison, the node that is located at the height of the middle of the last row of elements of the Lagamine model.

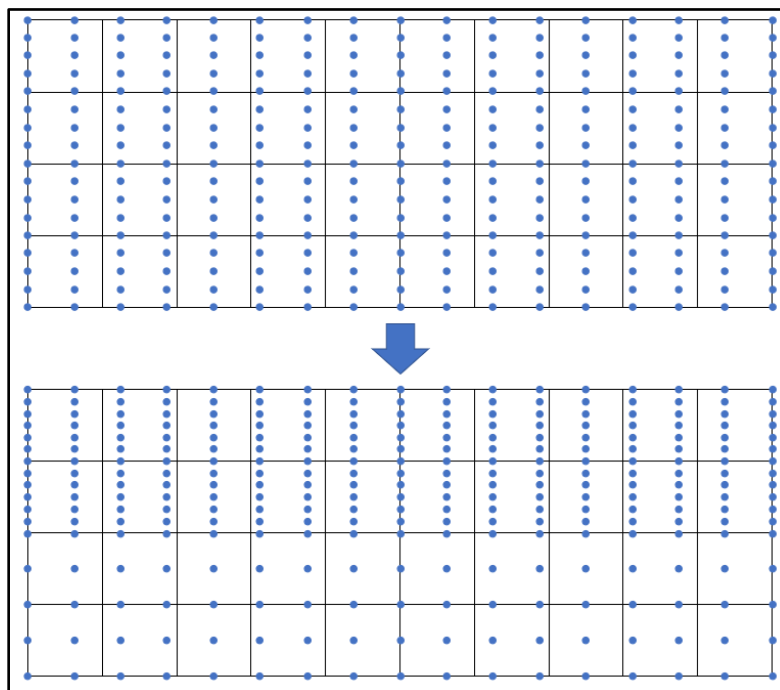


Figure 4.28: Mesh modification; Original (Top); Modified (Bottom)

Figure 4.29 shows the results of the original mesh and those of the modified mesh and it can be observed how the oscillations have been reduced. In addition, it should be taken into account

that the concentration values obtained by this new mesh are slightly lower than those of the original mesh. For this reason, the time necessary for $\frac{1}{4}$ of the mesh to be affected by corrosion must be re-determined, as the concentration is slightly lower, so the time to reach this point will be slightly longer. After repeating the process of determining the simulation time in the same way as previously, it is concluded that the simulation time required increases from 6.8 years to 7.05 years. In addition, it is worth mentioning that both models are still mechanically compatible without applying corrosion.



Figure 4.29: Corrosion comparison between original mesh and modified mesh

Once the improvement of the mesh has been validated and the simulation time has been corrected, the comparison with the Lagamine model is carried out as initially planned. In this 7.05 year simulation, the corrosion variable in Lagamine was readjusted, since the diffusion is slower with the new mesh, the corrosion ratio in Lagamine was lowered to $k_u = 8 \cdot 10^{-13} \text{ m/s}$.

However, the results of the models are still far apart, Figure 4.30, even though the amplitude of the negative oscillations are not very significant at this stage. The remaining difference is based on the fact that in the Lagamine model the corrosion variable increases from the moment the simulation starts, following a parabolic damage law. On the other hand, in the diffusional model, the damage variable starts to increase between year 1 & year 2, because the node is close to the surface, but in terms of corrosion, it takes quite a long time to diffuse to that point. Therefore, it is not possible to make the comparison in this way, since in the diffusional model the case of instantaneous damage will never occur with the experimental diffusion values.

If the definition of the corrosion damage variable D_u in the Lagamine model is reminded, the value of this variable consists of the average damage in the Lagamine element due to corrosion. This means that the result does not show the damage in the centre of the element, but an average of the whole element, therefore, the same logic can be applied with the diffusional model. By averaging the damage variables of all nodes of the diffusional model that are located within the element from which the damage variable of the Lagamine model is obtained, the average damage of the whole element is compared in both cases, avoiding the null damage in the first years of simulation in the diffusional model.

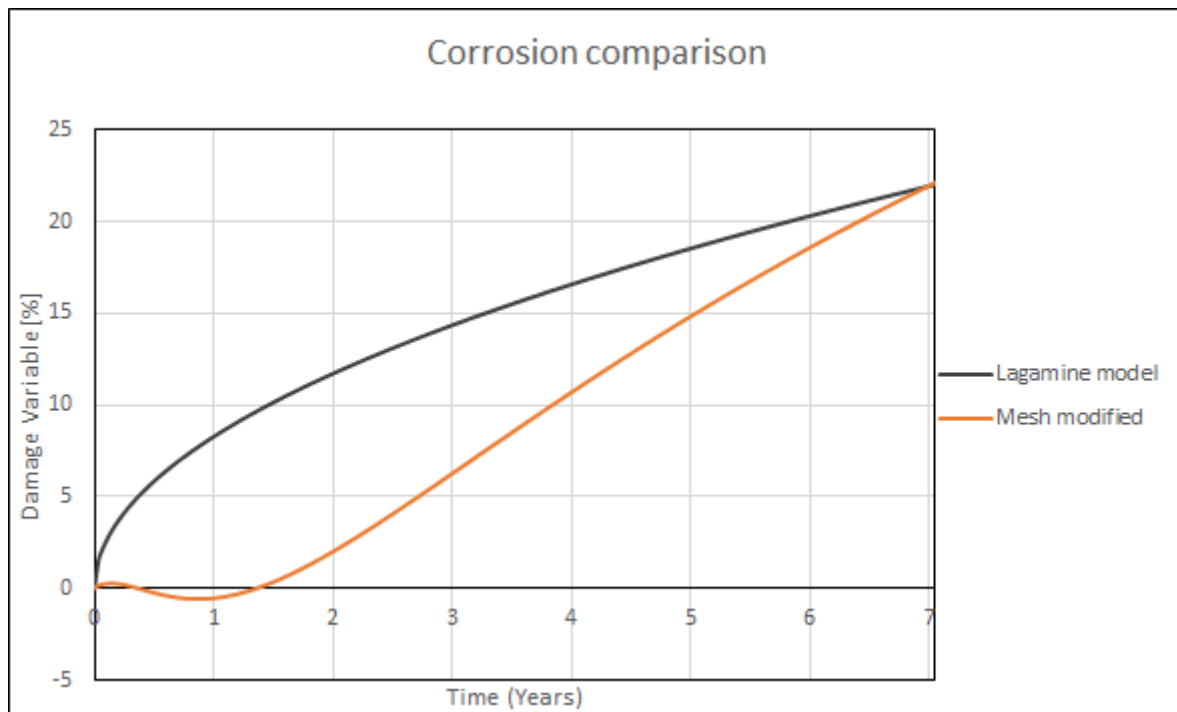


Figure 4.30: Corrosion comparison between Lagamine model and modified mesh

4.3.5 Corrosion comparison by average damage variable

It has been shown that to achieve an equivalent comparison of models, the damage variable in the diffusional model must be averaged. When studying an element affected by corrosion in the Lagamine model, the results of all the nodes of the diffusional model that are in the equivalent place to that element must be taken into account. Following this logic, two ways of averaging will be studied, the first considering the nodes that are entirely within the Lagamine model element, and the second, also taking into account the nodes at the upper and lower boundary of the element.

Figure 4.31 shows the Lagamine mesh with the diffusional model nodes superimposed and shows the two options for averaging the damage variable of the Lagamine model element (Green). From this point on, the way of averaging including the nodes of the element boundaries is referred to in this paper as 7 nodes average and the other way, counting only the inner nodes, as 5 nodes average.

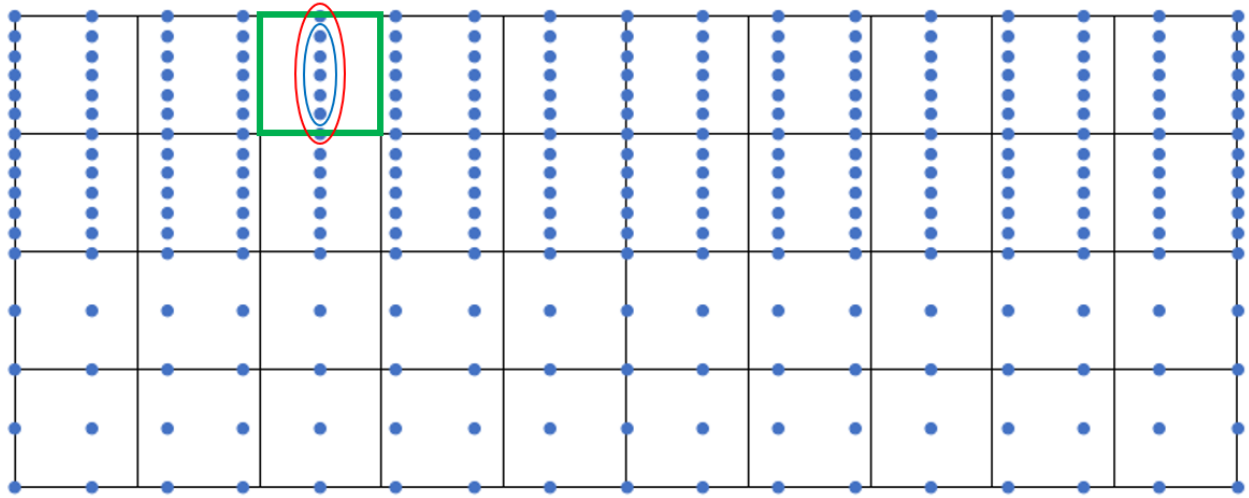


Figure 4.31: Mesh used for the average comparison. Lagamine element (Green); 5 nodes average (Blue); 7 nodes average (Red)

In order to determine which is the optimal way to perform this averaging, we will show the results of both ways in order to argue which is the best, observing their similarity to the physical phenomenon of corrosion and to the Lagamine model.

Firstly, the 7 nodes average is carried out, performing a 10-year simulation and using the literature corrosion values in the diffusional model. For the Lagamine model, the best fit to this average is achieved by using $k_u = 1,85 \cdot 10^{-12} \text{ m/s}$ as the corrosion variable.

The results of this comparison are shown in Figure 4.31. It can be seen that in the long term, both models tend to have the same shape of the curve of the damage variable, however, the biggest discordance is found at the beginning of the simulation, since the results of the 7 nodes average start at 15% corrosion damage.

This damage at the beginning of the simulation has no justification at the physical level considering the corrosion phenomenon, because it makes no sense for an undamaged material to have corrosion damage at the initial instant. The reason for this initial difference is that the method of averaging takes into account the upper boundary node of the element, which, being on the surface of the beam, is subject to the boundary condition of 100% initial corrosive concentration. Therefore, by averaging the results of the node with the boundary condition, the

average damage at the start of the simulation is greater than zero, consequently, does not match either the Lagamine model or the actual corrosion phenomena.

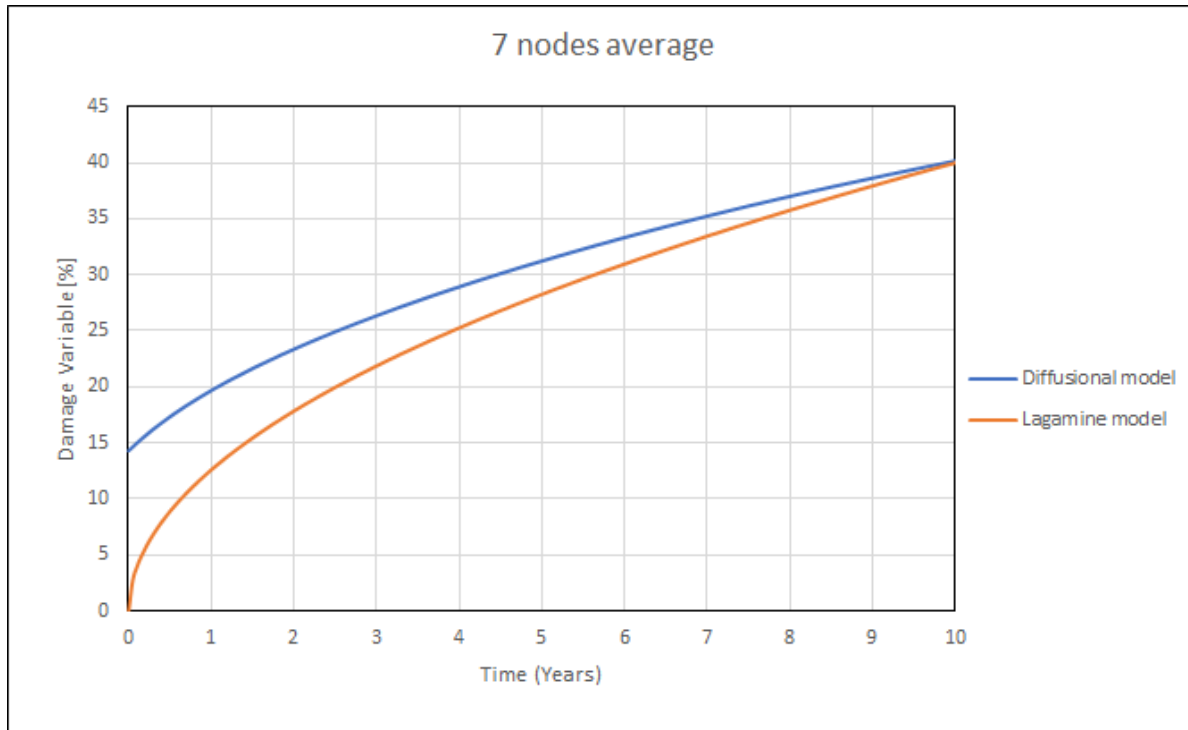


Figure 4.32: Corrosion comparison between models with the 7 nodes average

As discussed, the initial surface concentration of 100% is an unrealistic situation that is not equivalent to what actually happens, however, this is part of the limitations of the model, which uses this boundary condition in order to model corrosive diffusion within the material.

To alleviate this deficiency, certain strategies can be tried, such as substituting the corrosive values of the surface node by performing a linear interpolation with the concentrations of the interior nodes, obtaining a more realistic approximation of the corrosive concentration of the surface and thus being able to make the 7 nodes average.

The results of this strategy can be viewed in Figure 4.33. In this comparison, a greater similarity with the results obtained by Lagamine can be appreciated and they are in agreement with the real phenomenon of corrosion, since when performing the interpolation, the average damage variable starts at 0. However, when performing this interpolation on the corrosion aspect, it would also have to be done on the mechanical aspect of the study, which is hardly justifiable from the point of view of the mechanical model.

Therefore, despite obtaining a better approximation of the damage variable with this strategy, it has not been used in this study, as assumptions have to be made on all kinds of mechanical

aspects that are doubtfully justifiable and that would lead to a more complete and consensual analysis of the mechanical model.

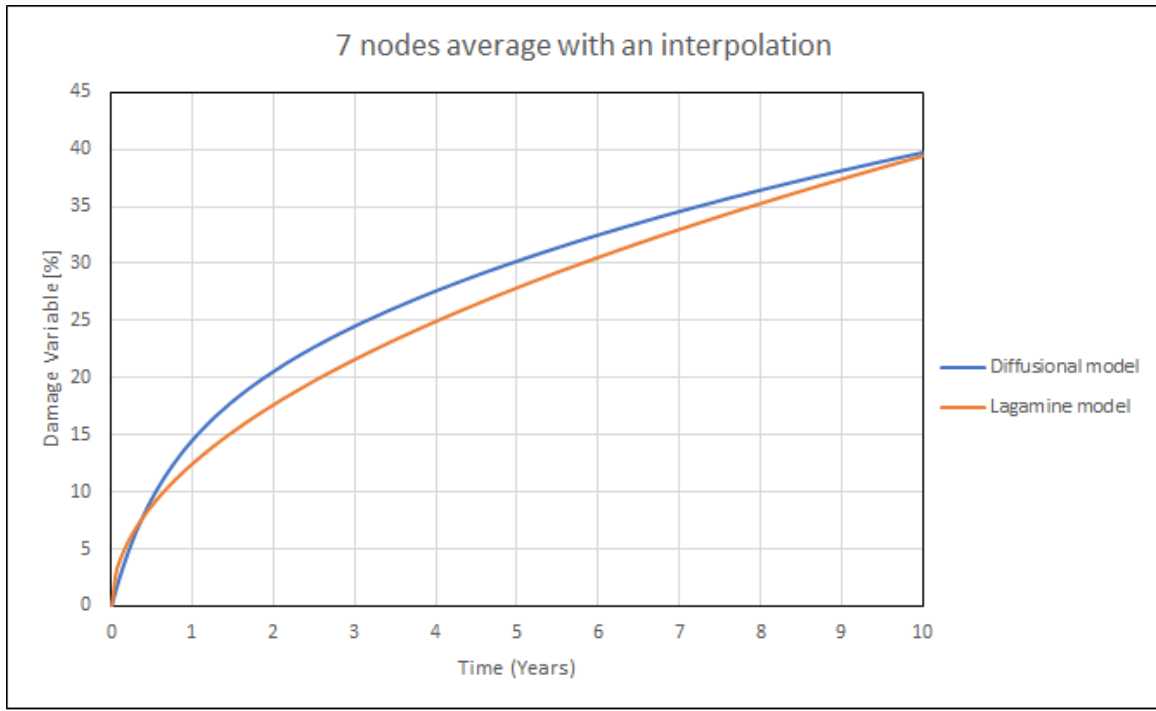


Figure 4.33: Corrosion comparison between model with the 7 nodes average with an interpolation

Considering that the first approach to averaging cannot be used, the option of 5 nodes average, Figure 4.34, which does not take into account the unrealistic boundary condition applied to the surface, is chosen.

In this comparison with the 5 nodes average, the corrosion variable used for the Lagamine model is $k_u = 1,5 \cdot 10^{-12} \text{ m/s}$. Regarding the results, both models are reasonably similar from year 5 onwards and their long-term trend is identical, however, at the beginning of the simulation, differences between the models are still observed and both curves have different shapes.

By being forced to choose this averaging option, fewer nodes are taken into account and some accuracy may have been lost by only taking into account the 5-node results of the diffusional model. Therefore, it is not yet possible to ensure that the comparison is sufficiently accurate, as using only 5 nodes in the average corrosion damage variable might not exploit the full potential of this model to simulate diffusion corrosion within the beam.

Therefore, in order to be able to obtain reliable conclusions from this model comparison, a new strategy has to be proposed to overcome this limitation of the diffusional model.

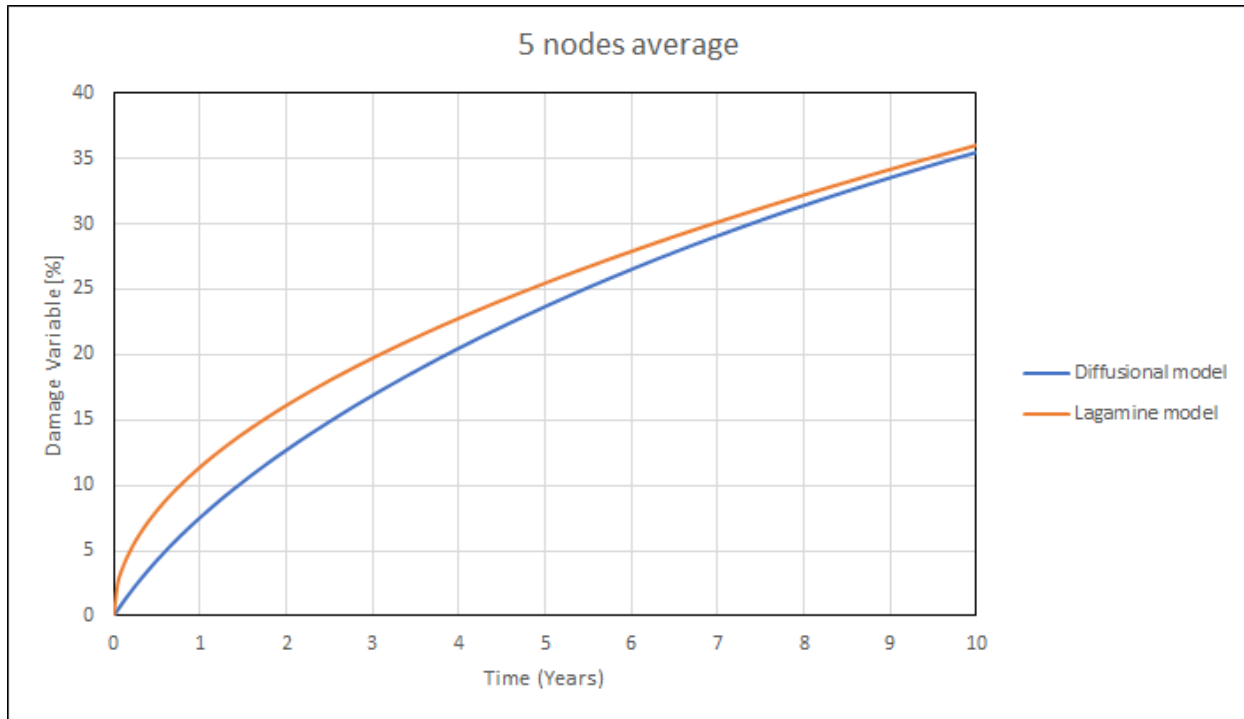


Figure 4.34: Corrosion comparison between model with the 5 nodes average

Actually, the best way to solve the problem of the unreal boundary condition of 100% concentration on the surface of the beam would be to replace this fixed condition by an evolution of the surface concentration following the principles of a convective transition between the surface of a liquid and a solid. Thus, if the surface concentration were modelled as if it were the temperature in a convective case, it would be much closer to an actual corrosion diffusion.

However, this convective transition cannot be easily integrated into the diffusional elastic model since the convective law would have to be incorporated and the model code would have to be modified. Therefore, to overcome this limitation of the model, it was decided to modify again the mesh of the diffusional model, in order to concentrate more nodes near the surface so that the results of more nodes are taken into account, and therefore, be more accurate.

4.3.6 Mesh modification to overcome the convection limitation

In this new modification of the mesh of the diffusional model, the concentration of nodes is made only in the last row of Lagamine elements, since they are the only ones that are affected by corrosion and therefore they are the ones that need more precision for the modelling of the diffusion.

Figure 4.35 shows the modification made to the mesh, in this way, instead of having only 5 nodes in the inner part of the Lagamine element, there are 9 nodes, so it is expected to get a more

accurate average corrosion damage in the elastic diffusion model. And therefore, a better model comparison to obtain the optimal parameters at the end of the study.

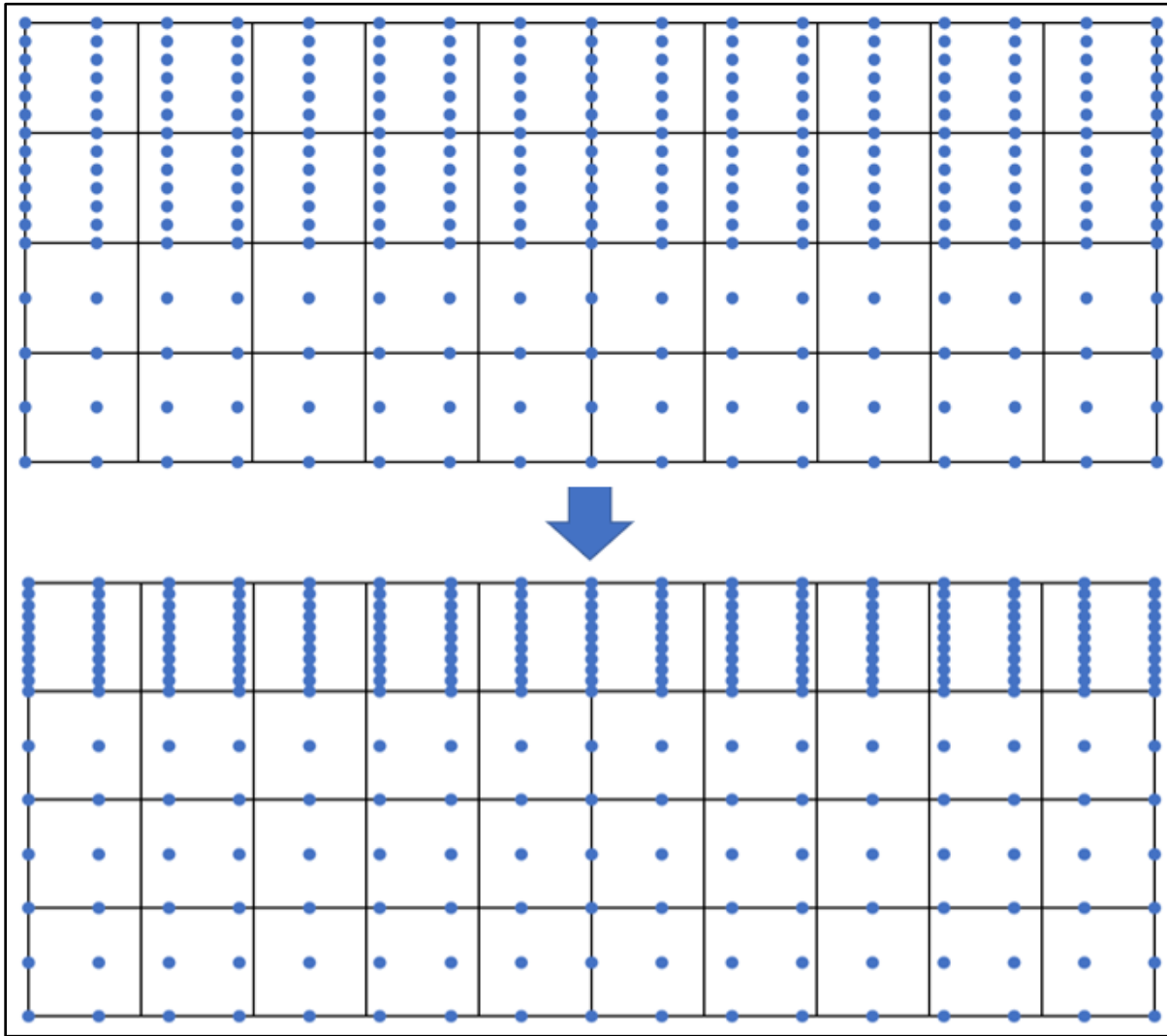


Figure 4.35: Second mesh modification

4.3.7 Final comparison between models

With this new mesh, a final comparison between models is made. Following the original idea, a comparison is made for 7.05 years (time for corrosion to occur in $\frac{1}{4}$ of the beam) and the corrosion variable of the Lagamine model is adjusted to obtain the most similar results with respect to the diffusional model with values from the literature, Table 4-4. As a result of this last comparison, it is expected to obtain the optimal corrosion parameters for the Lagamine model.

Lagamine model	Diffusional model		Test	
K_u (m/s)	D (mm ⁻¹ /s)	M (MPa ⁻¹)	Time (Years)	Load (MPa)
$1,5 \cdot 10^{-12}$	$1,397 \cdot 10^{-12}$	0,0098	7,05	60

Table 4-4: Comparison conditions

The corrosion comparison is shown in Figure 4.36. With the new mesh change the results have improved slightly, however, in the short term there are still differences in the two models. This is because the Lagamine model, following a parabolic corrosion damage law, is not able to adjust the shape of the curve by varying the corrosion variable and therefore it is not possible to achieve a better fit with the diffusional model.

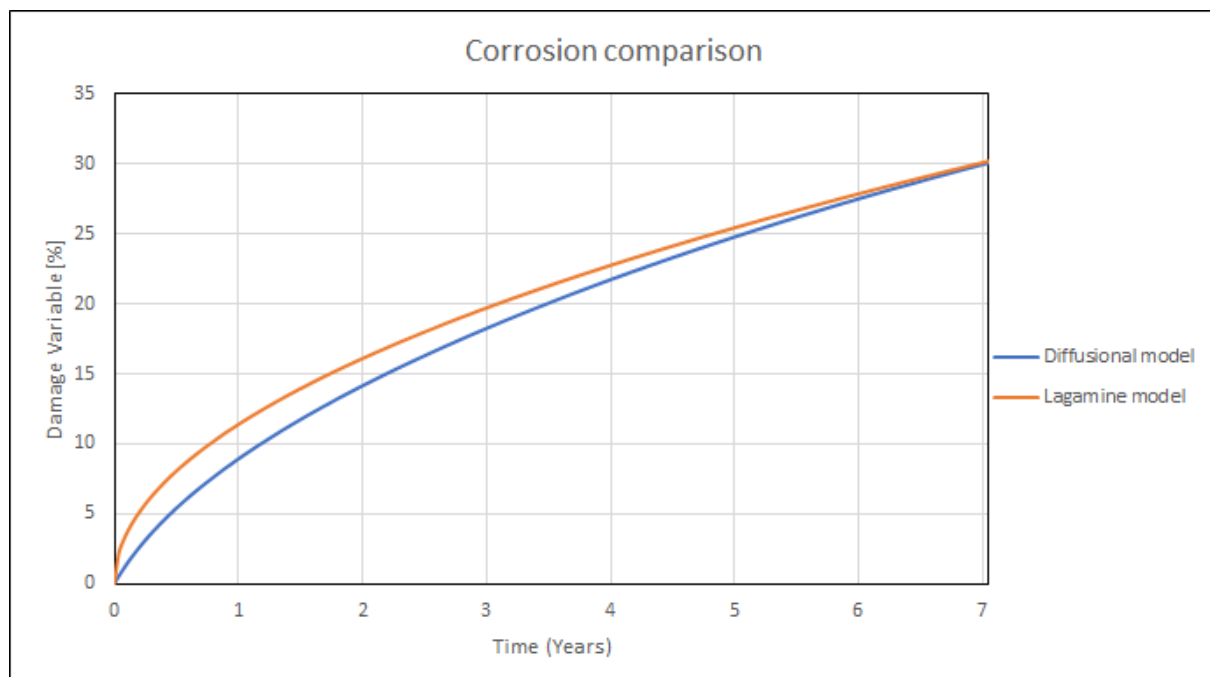


Figure 4.36: Final corrosion comparison between models

Once both models have been adjusted as closely as possible from the point of view of corrosion damage, it is necessary to check if both models give similar mechanical results, to ensure that they are still compatible and that the conclusions obtained from the corrosion comparison are valid.

To perform the mechanical comparison between models, the stress-strain curve of both models will be shown, both in the corrosion zone and in the non-corrosion zone. As it has been done with the corrosion damage in the diffusional model, when extracting the results of stress and deformation of the diffusional model, an average of the interior nodes corresponding to the equivalent element in Lagamine will be carried out.

Therefore, in order to mechanically compare both models, the stress-strain curve of a Lagamine element affected by corrosion (Black) Figure 4.37, will be compared with the average stress-strain curve of all the interior nodes of the diffusional model. On the other hand, the comparison of the non-corrosion zone (Red) is made by comparing with the results of the single interior node of the diffusional model, due to the mesh used.

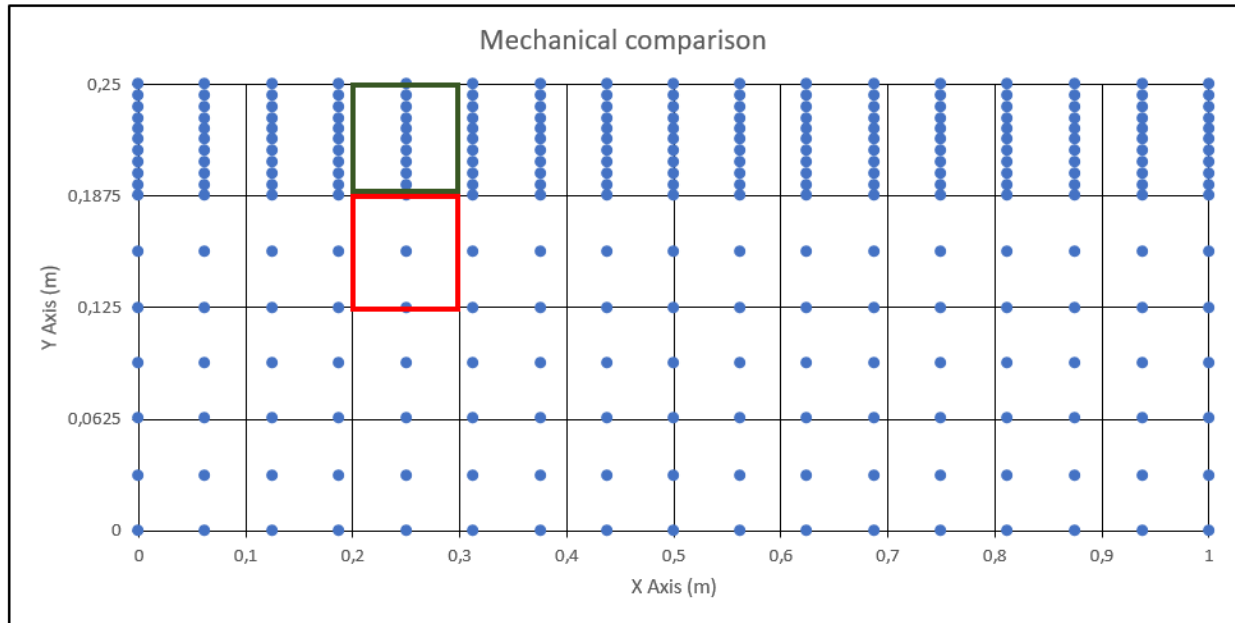


Figure 4.37: Mechanical comparison; In the corrosion zone (Black); Outside the corrosion zone (Red)

In first place, the comparison is made in the area with corrosion, Figure 4.39, in which it can be seen how in both models, the slope of the curve decreases as time goes by, due to the decrease in Young's modulus in both cases due to the corrosion damage, Figure 4.38. In the graphic of the mechanical comparison, it can be noticed how both models give practically identical results, so it can be concluded that in the area affected by the corrosion, both models have the same mechanical behaviour.

The only difference that can be perceived between the two models is that there are stages in which the curve of the diffusional model is slightly higher than the curve of the Lagamine model. This is due to the difference in corrosion damage between the two models (as seen in the corrosion comparison), especially in the middle of the simulation, as the diffusional model has less corrosion damage, so the slope of the stress-strain curve is slightly bigger.

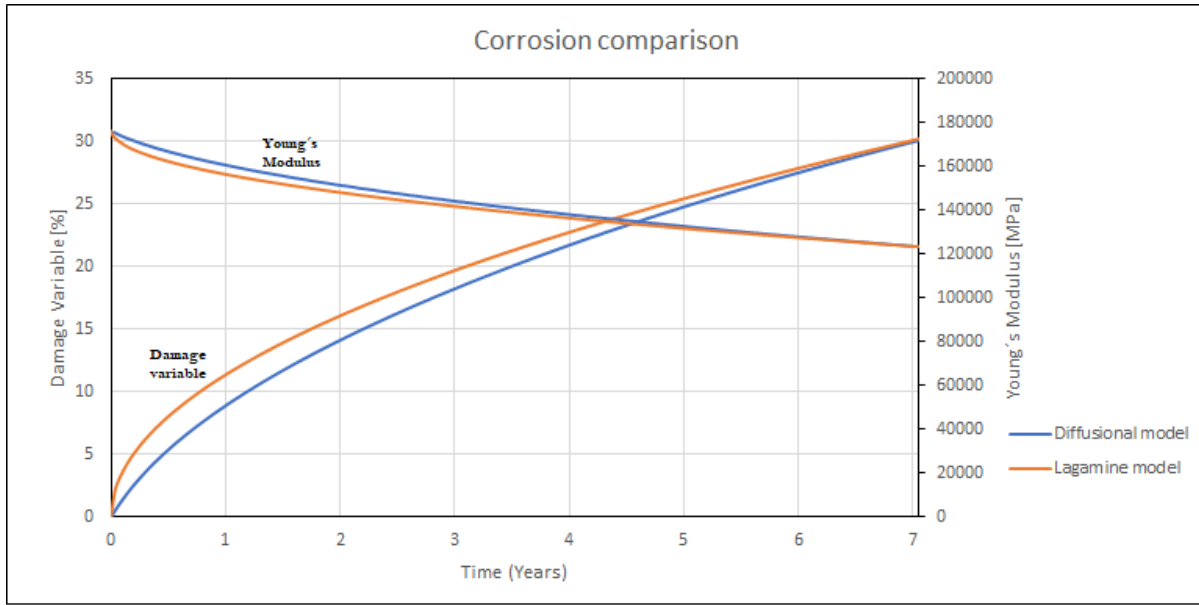


Figure 4.38: Young's modulus decrease compared to damage evolution

Once it has been verified that the area affected by corrosion, $\frac{1}{4}$ of the beam, is compatible in both models both in terms of corrosion damage and mechanical behaviour, it must be verified if the rest of the beam, which is not directly affected by corrosion damage, also has the same mechanical behaviour in both models.

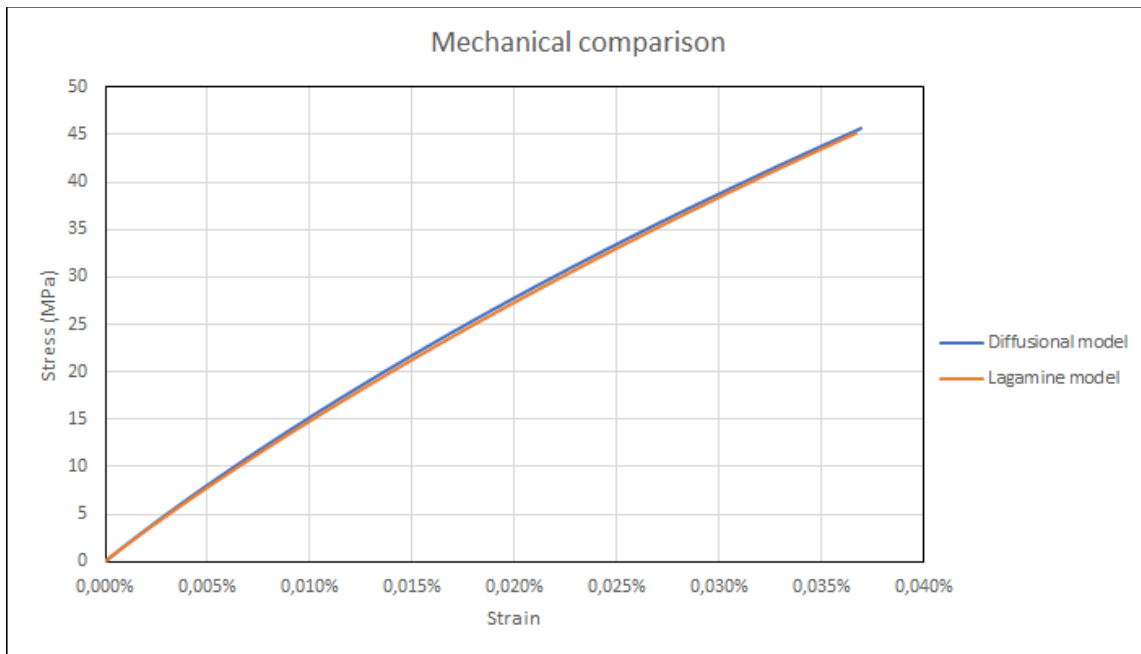


Figure 4.39: Final mechanical comparison between models (In the corrosion zone)

Figure 4.40 shows the comparison between the stress-strain curves of the area not affected by corrosion. It can be observed how the results are identical except that in the diffusional model a slight prolongation of the curve is obtained, however, the rest is equal, so it can be stated that the mechanical behaviour of both models is compatible in the whole beam.

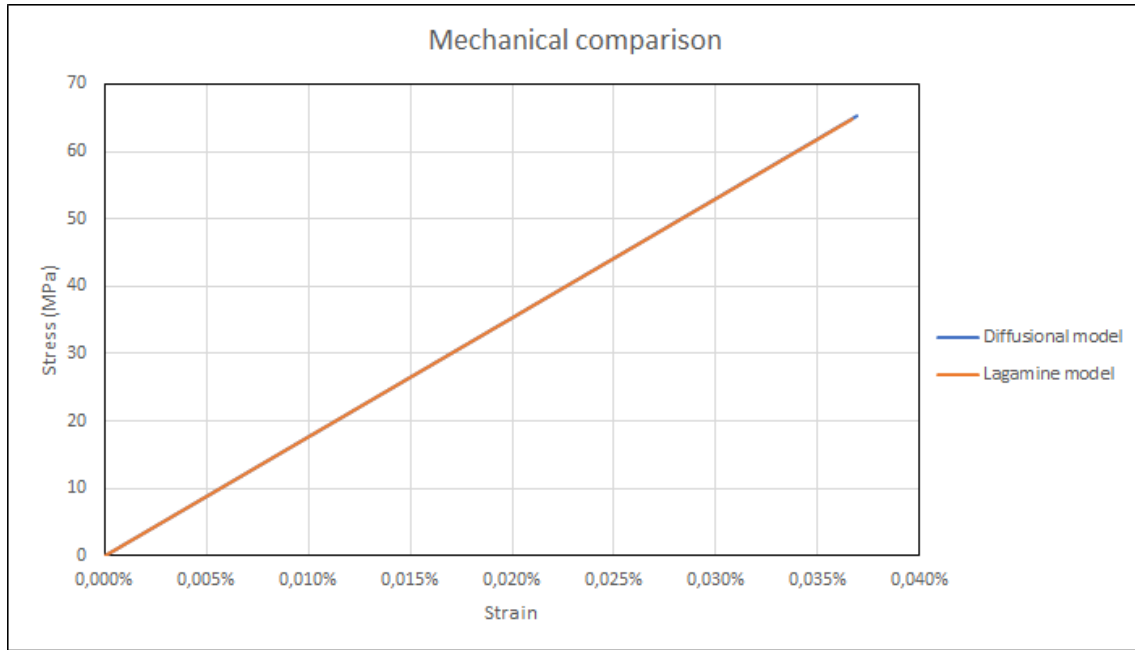


Figure 4.40: Final mechanical comparison between models (Outside the corrosion zone)

In conclusion, by making the necessary changes in the meshing of the diffusional model to overcome the limitations of the model itself, an adjustment of both models at the corrosion level has been carried out to determine the corrosion variable of the Lagamine model that obtains the results closest to those of the diffusional model, for the conditions of this test described.

Thus, for the 700°C, the value of the corrosion ratio that gives the optimal results in the Lagamine model is $K_u = 1,5 \cdot 10^{-12} \text{ m/s}$. To validate that this result is sufficiently reliable, a mechanical comparison between the two models has also been carried out to verify that they are compatible while applying corrosion

However, as shown in the model comparison, the Lagamine model with the parabolic corrosion damage law does not achieve perfect coupling with the results of the diffusional model, as there are sections of the simulation in which slight differences appear due to this parabolic law.

5 Discussion

In this work, the coupling of the Lagamine model and the diffusional model in terms of corrosion diffusion has been tested. Once the proposed test has been completed, the optimal solution has been reached with the current corrosion damage law of the Lagamine model, which achieves similar results to the diffusional model, but as seen in previous comparisons, it can still be improved if a finer model adjustment is desired.

Therefore, in this chapter we seek to modify the corrosion damage law of the Lagamine model, aiming for a better fitting with the results of the diffusional model, by suggesting a new corrosion damage equation.

To begin with, the current corrosion damage law used by the Lagamine model is shown:

$$D_u = \frac{1}{L_E} \sqrt{2k_u \cdot t} \quad (5.1)$$

Considering the size of the elements of the Lagamine model ($L_E = \sqrt[3]{V_E}$) and the corrosion variable obtained as a result of the fit between models ($k_u = 1,5 \cdot 10^{-12} \text{ m/s}$), the following expression is obtained after substituting the values:

$$D_u = 11,696 \cdot \sqrt{3 \cdot 10^{-12} \cdot t} \quad (5.2)$$

Operating the expression (5.2):

$$D_u = 2,026 \cdot 10^{-5} \cdot t^{0,5} \quad (5.3)$$

Obtaining a time-dependent exponential expression, in which there is a constant ($2,026 \cdot 10^{-5}$) and an exponent (0,5). Taking into account the form of the current damage law, it is aimed to find the optimal values for both the constant and the exponent, so that the new equation gives results more similar to those given by the diffusional model, where the time unit is seconds.

$$D_u = K \cdot t^x \quad (5.4)$$

5.1 Equation fitting for 7,05 years

In this section, the values of the damage equation of the Lagamine model will be determined so that the new equation achieves the best fit for the results of the diffusional model in the 7,05-year simulation.

To carry out this adjustment, the Excel tool called Solver will be used to obtain the values of K and x for which there is the smallest difference with respect to the results of the diffusional model. Therefore, using Solver the results shown in the Table 5-1 are obtained.

K	x
$2,224 \cdot 10^{-6}$	0,61467

Table 5-1: Equation values obtained with Solver for the 7,05-year simulation

This being the new damage equation:

$$D_u = 2,224 \cdot 10^{-6} \cdot t^{0,61467} \quad (5.5)$$

Looking at the new formula, it can be noticed that the coefficient is not very far from the original coefficient of the Lagamine model, so it can be stated that the assumption of the parabolic law of damage is not very far from reality, a fact that has been demonstrated throughout the comparison between the two corrosion models.

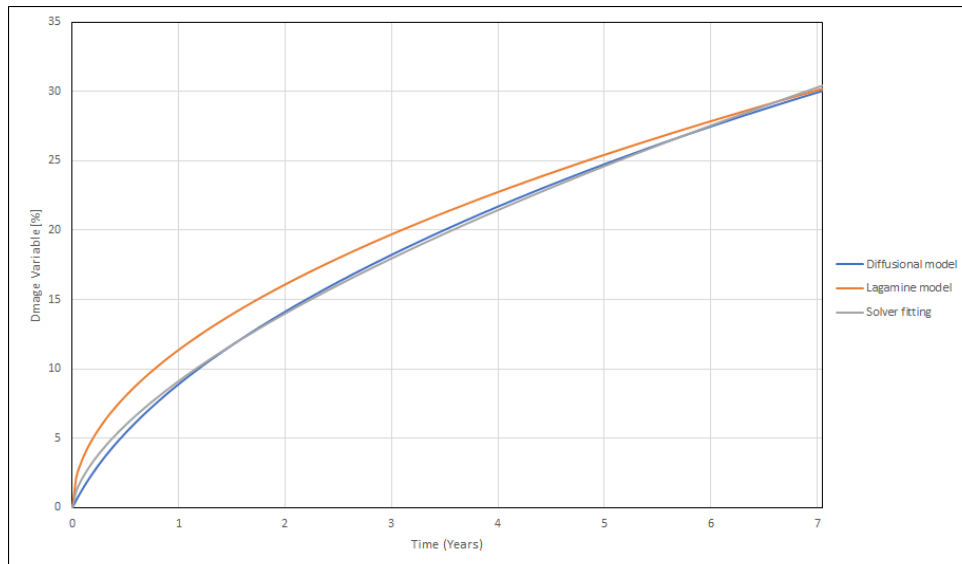


Figure 5.1: Comparison with Solver fitting; 7,05-year simulation

Therefore, Figure 5.1 shows the results of the Lagamine model, the diffusional model and the new equation for the 7.05 year simulation. In this graph, it can be appreciated how the new curve fits much better to the results obtained in the diffusional model thanks to the use of the Solver tool.

However, despite the improvement with the new equation, the coupling of results is not perfect as there are sections in which there are slight differences with respect to the diffusional model, although these differences are much smaller than with the results of the Lagamine model, as can be seen in the graph.

Additionally, if we extend the duration of the comparison between the 3 cases to a 10-year simulation (Figure 5.2), it can be seen how the solution obtained with Solver, despite having a great fit in the short term, obtains worse results in the long term than even the Lagamine model, which adapts almost perfectly to the diffusional model in the long term.

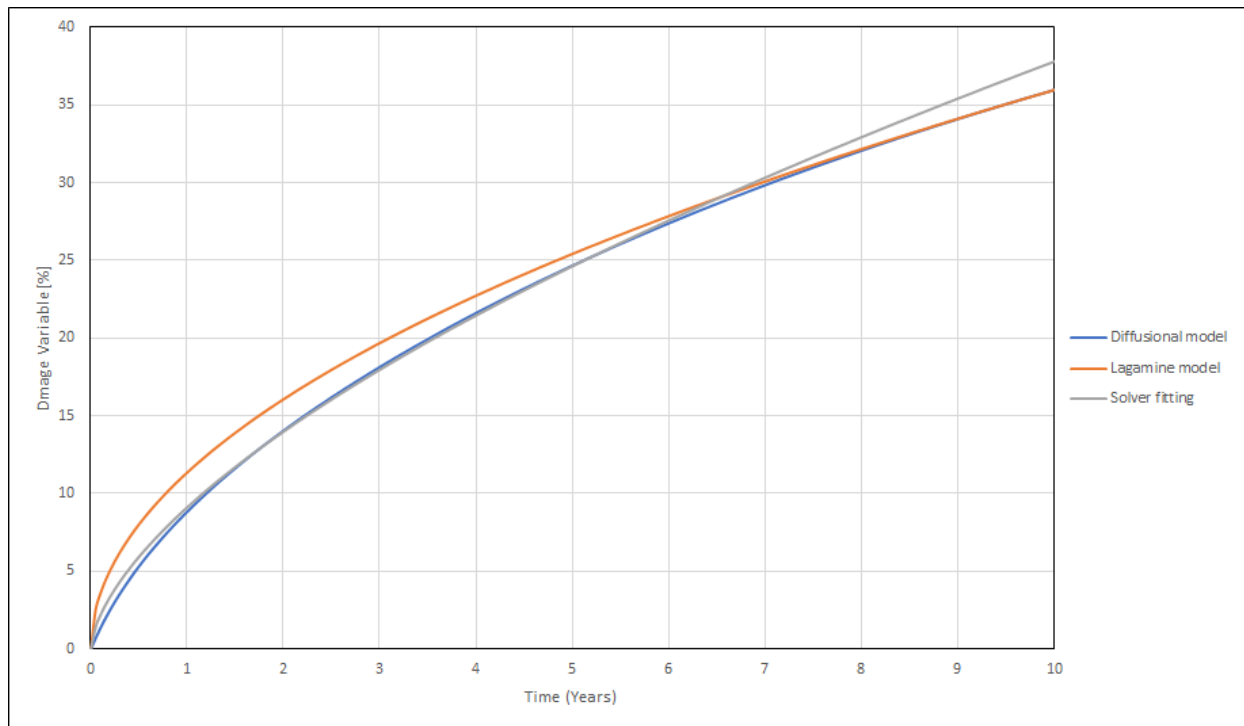


Figure 5.2: Comparison with Solver fitting; 10-year simulation

Taking into account that the application of the Lagamine model is to estimate the lifetime of the different compounds of a CSP plant and that the goal for the new generation is to ensure a minimum lifetime guarantee of 25 years, the new equation adjusted with the Solver tool would not be useful to incorporate it in the Lagamine model, since in the long term it gives worse results than the original formula.

5.2 Equation fitting for 25 years

In this section, the same fitting process is performed with the Solver tool and compared with the results of the Lagamine model and the elastic diffusional model for a simulation of 25 years, a reasonable lifetime for the receiver pipes of a CSP plant.

Following the same procedure as in the previous section, the following values for the new damage equation are obtained:

K	x
$2,323 \cdot 10^{-5}$	0,49143

Table 5-2: Equation values obtained with Solver for the 25-year simulation

Therefore, the equation has the following formula:

$$D_u = 2,323 \cdot 10^{-5} \cdot t^{0,49143} \quad (5.6)$$

If we compare this equation (5.6) with the original one obtained with the model comparison (5.3), we can appreciate that both the constant and the exponent are very similar, almost identical. In fact, in the results graph (Figure 5.3), it can be seen how the adjustment gives practically the same results as those obtained with the Lagamine model, apart from slight differences in some sections and a small improvement in the long term with the new formula.

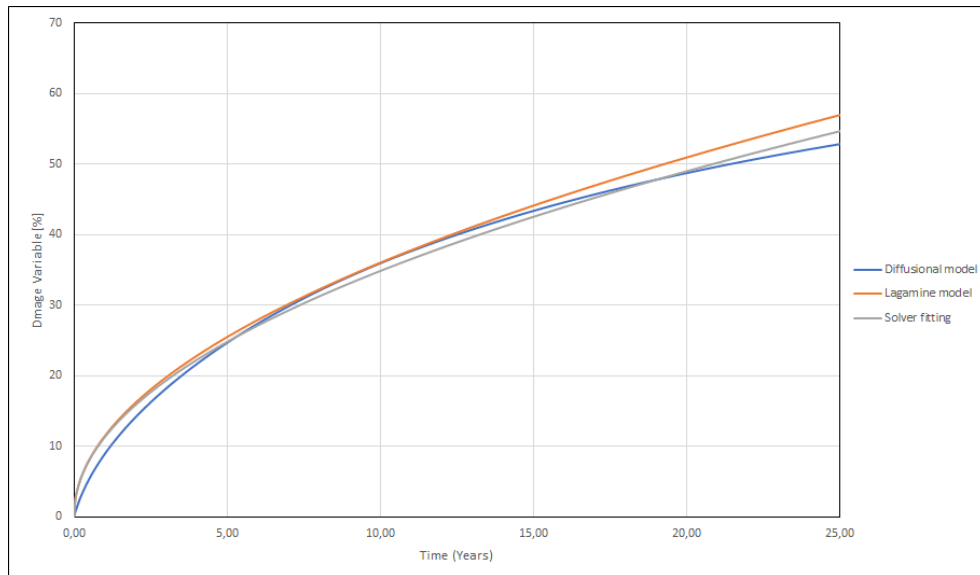


Figure 5.3: Comparison with Solver fitting; 25-year simulation

With this new equation, a better prediction of corrosion damage after 25 years of operation can be obtained since the damage variable at 25 years is closer to the value obtained with the diffusional model. Moreover, due to its similarity with the original formula obtained by the Lagamine model, it indicates how the parabolic damage law hypothesis used in Lagamine fits quite well to actual reality and, above all, to the best possible fit of Solver.

It is worth mentioning that it has been tried to fit the results of the diffusional model with other types of equations compatible with corrosion kinetics such as linear, logarithmic or inverse logarithmic, however, none of these has given a better fit than the one finally used. Therefore, it is considered that it is not possible to adjust the formula further, at least for the described test conditions.

6 Conclusions and perspectives

In the work carried out in this master thesis, the optimisation of the corrosion variable of the Lagamine model has been sought by comparing the corrosion damage variable with the diffusional model, whose corrosion modelling is based on the use of the corrosive concentration as a degree of freedom of the model. In this way, the corrosion variable has been calibrated for the Lagamine model for the case of a nickel-based alloy, a material that will be used in the components of the next generation of CSP plants, due to its good properties at high temperatures and its great corrosion behaviour.

For this purpose, this work compares the results of both models with a simple tensile test over time, exposing the material to a progressive load within the elastic working zone at a temperature of 700°C. For this, the boundary conditions of the test are established, which are implemented in both models, so an equivalent test is performed, and the comparison is validated.

Regarding the corrosion-related conditions, literature values are used for the corrosion variables of the diffusional model at 700°C for nickel-based alloys, and the value of the corrosion variable of the Lagamine model is determined for which both models give the closest possible results. The model comparison is performed for when $\frac{1}{4}$ of the beam mesh of both models is affected by corrosion.

Both models have a common damage law that models a linear degradation of the Young's modulus of the material due to corrosion, therefore, when corrosion is applied to the top of the beam, the mechanical behaviour of the beam is affected. Therefore, during the comparison, it is verified that the mechanical behaviour of both models is still compatible to validate the comparison, through the stress-strain curves.

The models have a different approach to corrosion. On the one hand, the Lagamine model indicates, in the input file, which elements are to be exposed to a parabolic corrosion damage law and, on the other hand, the diffusional model models the diffusion of corrosion within the beam. Therefore, the comparison is made for a simulation time in which the corrosion has diffused into a $\frac{1}{4}$ of the diffusional model mesh. As a criterion to determine whether or not the material is affected, a degradation of 1% of the Young's modulus is chosen as a limit.

During the model comparison, several changes are made to the diffusional model mesh due to the limitations of the model itself since, for example, the initial surface corrosion condition fixes a constant corrosion value throughout the simulation, when in reality it should follow an evolution with time, equivalent to the temperature in a convective situation at the surface between a liquid and a solid.

After the model comparison, the optimal value of the corrosion variable of the Lagamine model is found, which fits the results of the Lagamine model reasonably well. However, it can still be improved.

Therefore, using the Excel Solver tool, a new exponential equation for the corrosion damage in the Lagamine model is suggested in order to better fit the results of the diffusional model.

Finally, after performing this adjustment, an exponential formula is obtained that achieves a slightly better estimation of the corrosion damage in the long term. However, this improvement is not substantially significant since the equation itself has very similar values to the original equation implemented in the Lagamine model, which indicates that the use of the original equation is adequate and that no significant optimisation of the equation can be performed.

Additionally, during the work carried out, no significant influence of the load on the corrosion diffusion has been found. This was possibly due to the use of a not very high load, because it was necessary to stay in the elastic working zone. Furthermore, if one looks at Figure 6.1, it can be seen that the pressure factor (which models the influence of the load on the rate of diffusion) has relatively small values compared to the values at higher temperatures.

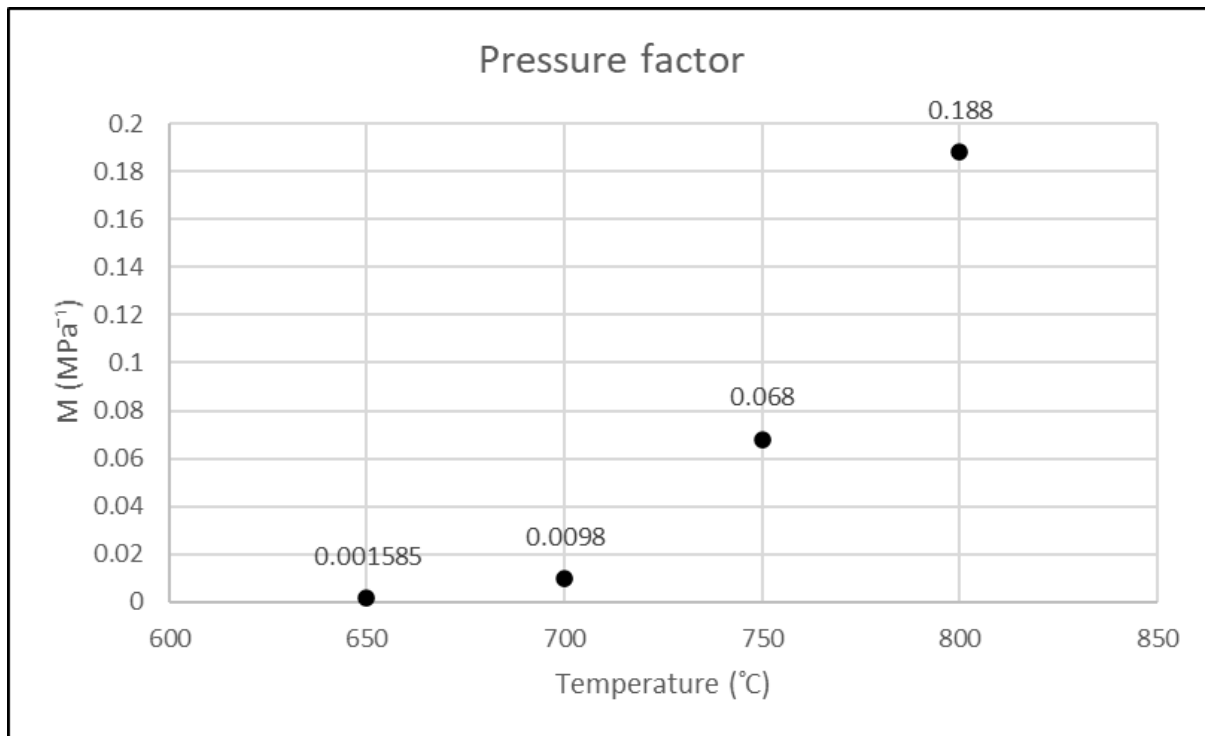


Figure 6.1: Pressure factor for nickel-based alloys at different temperatures [15]

Several additional perspectives can also be considered. For instance, the incorporation of the plastic zone modelling into the diffusional model. In this way, it would be possible to work with higher loads, being able to appreciate other damage factors that are related to plasticity, such as creep damage or fatigue damage, which do not participate in the current test. Taking these damage factors into account, the interaction between the different types of damage could be studied, as well as the influence of dynamic stiffening on the visco-plastic model of Lagamine.

Other improvements that could be implemented in the diffusional model to improve the quality of the comparison, is the evolution of the corrosive concentration on the beam surface, following convective type equations.

Additionally, the implementation of cyclic loading or a cyclic variation of the temperature during the test would be very interesting, since it should be remembered that these are the real conditions to which the component materials are subjected in a CSP plant. Therefore, with this incorporation, it is expected to obtain conclusions closer to reality.

Bibliography

- [1] Md Tasbirul Islam et al. A comprehensive review of state-of-art concentrating solar power (CSP) technologies: Current status and research trends. *Journal of Renewable and Sustainable Energy Reviews* 91. 987-1018. 2018
- [2] International Renewable Energy Agency. Concentrating Solar Power: Clean Power on Demand 24/7. 2020
- [3] Pôle Mecatech. Solar Gnext. <https://www.polemecatech.be/fr/projets/solar-gnext/>, 2019-2022.
- [4] Technical specification: 82003/49E02. Particular Project data and environmental conditions. Cerro Dominador Project.
- [5] SQM's Thermo-Solar Salts: The natural solution for thermal storage and heat transfer in your CSP plant.
- [6] G.J Janz, Ursulu Krebs, H.F. Siegenthaler and R.P.T. Tomkins. Molten salts: Volume 3, Nitrates, Nitrites and Mixtures: Electrical conductance, density, Viscosity, and surface tension data. *Journal Pys. Chem. Ref. Data*, Vol1. No. 3. 1972
- [7] Julian Steinbrecher et al. Investigation of Regeneration Mechanisms of Aged Solar Salt. *Journal of Materials* 14. 5664. 2021
- [8] P. Gimenez et al. Effect of heating rates and composition on the thermal decomposition of nitrate based molten salts. *Journal of Energy Procedia* 69. 654-662. 2015
- [9] Qiang Peng et al. The release properties of nitrogen oxides of solar salt used for thermal energy storage in different environment. *Journal of Energy Procedia* 105. 4420-4427. 2017
- [10] Heng Li et al. Impact of temperature on corrosion behavior of austenitic stainless steels in solar salt for CSP application: An electrochemical study. *Journal of Solar Energy Material & Solar Cells* 239. 110-162. 2022
- [11] Florian Sutter et al. Dynamic corrosion testing of metals in solar salt for concentrated solar power. *Journal of Solar energy materials and solar cells* 232. 111331. 2021

- [12] H.E.Evans et al. Mechanisms of Breakaway Oxidation and Application to a Chromia-Forming Steel. *Journal of Oxidation of Metals* 52.379-402. 1998
- [13] Alexander Bonk et al. Impact of Solar Salt aging on corrosion of martensitic and austenitic steel for concentrating solar power plants. *Journal of Solar energy materials and solar cells* 203. 110162. 2019
- [14] Heng Li et al. Effect of Chloride Impurity on Corrosion Kinetics of Stainless Steels in Molten Solar Salt for CSP Application: Experiments and Modeling. *Journal of Experiments and Modeling. Oxidation of Metals* 95. 311-332. 2021
- [15] A.Karabela et al. Oxygen diffusion and crack growth for a nickel-based superalloy under fatigue-oxidation conditions. *Journal of Materials Science & Engineering A* 567. 46-57. 2013.
- [16] J.A. Grogan et al. A physical corrosion model for bioabsorbable metal stents. *Journal of Acta Biomaterialia* 10. 2313-2322. 2014
- [17] Zhenquan Shen et al. Predicting the degradation behaviour of magnesium alloys with a diffusion-based theoretical model and in vitro corrosion testing. *Journal of Materials Science & Technology* 35. 1393-1402. 2019
- [18] Neu and Sehitoglu. Thermomechanical Fatigue, Oxidation, and Creep: Part II. Life Prediction. *Journal of Metallurgical Transactions A* 20, 1769-1783. 1989
- [19] Da Costa-Mattos et al. A simple model for slow strain rate and constant load corrosion tests of austenitic stainless steel in acid aqueous solution containing sodium chloride. *Journal of Corrosion Science* 50. 2858-2866. 2008
- [20] D. Gastaldi et al. Continuum damage model for bioresorbable magnesium alloy devices – Application to coronary stents. *Journal of the Mechanical Behavior of Biomedical Materials* 4. 352-365. 2011
- [21] University of Liège. Lagamine. [LAGAMINE \(uliege.be\)](http://LAGAMINE.uliege.be).
- [22] Jean Lemaitre, Jean-Louis Chaboche, Ahmed Benallal, Rodrigue Desmorat. *Mécanique Des Matériaux Solides*. 2009.
- [23] Julien Heremans. Modeling of the interaction between corrosion diffusion and mechanical behavior of metallic alloys by FEM coupling. University of Liège. 2019

[24] Hélène Morch. Efficient temperature dependence of parameters for thermo-mechanical finite element modeling of alloy 230. Journal of European Journal of Mechanics-A/Solids 85.104116.2020